HIGH RESOLUTION MAGNETIC RESONANCE SPECTROSCOPIC IMAGING OF THE BRAIN FROM 3T TO 7T

BY

RONG GUO

DISSERTATION

Submitted in partial fulfillment of the requirements
for the degree of Doctor of Philosophy in Electrical and Computer Engineering
in the Graduate College of the
University of Illinois Urbana-Champaign, 2022

Urbana, Illinois

Doctoral Committee:

Professor Zhi-Pei Liang, Chair
Professor Brad Sutton
Professor Michael L Oelze
Professor Xin Yu (Case Western Reserve University)

ABSTRACT

The objective of this thesis research is to develop fast high-resolution magnetic resonance spectroscopic imaging (MRSI) methods of the brain at both high field (3 Tesla) and ultrahigh field (7 Tesla) MR.

MRSI has long been regarded as a promising tool for non-invasive imaging of brain metabolism, with its potential shown in a large range of applications including energy consumption analysis, brain functional investigation, brain lesions characterization like tumors and stroke, neurodegeneration assessment, etc. However, its practical utility has been largely limited by several long-standing technical obstacles, including low signal-to-noise-ratio (SNR), long scan time, and limited resolution. Given these limitations, it has been very challenging to perform three-dimensional high-resolution MRSI experiments in a clinically feasible time.

In recent years, a subspace-based MRSI method named as SPICE (SPectroscopic Imaging by exploiting spatiospectral CorrElation) has been proposed for accelerated MRSI. A number of proof-of-concept works using the basic SPICE method for ^{1}H-MRSI at 3T have demonstrated its potential and advantages in significantly advancing imaging speed, resolution, and SNR. However, imaging capability of the basic SPICE method still cannot satisfy the ever-growing clinical needs.

The proposed research further developed the SPICE method with multiple aspects of improvements, which significantly enhanced its imaging capability and made it a more practically powerful and clinically useful MRSI tool. In data acquisition, a novel pulse sequence was developed at 3T with multiple unique acquisition features for high imaging efficiency and robustness. More specifically, the proposed sequence used an FID (free induction decay)-based acquisition with ultrashort TE (echo time) and short TR (repetition time) for maximized SNR efficiency, removed water and lipid suppression pulses for minimized energy deposition, and employed fast spatiotemporal trajectories and highly sparse sampling of data space for fast imaging speed. As a result, three-dimensional metabolite signals (field of view: 240×240×72 mm^3) at 2.0×3.0×3.0 mm^3 nominal spatial resolution and unsuppressed water signals at 2.0×1.0×1.0 mm could be successfully acquired in an 8-minute scan. This method was also implemented and further developed at 7T MR systems. Taking advantage of the SNR benefit of ultrahigh field, the pulse sequence at 7T was pushed to achieve whole brain coverage (field of view: 240×240×160 mm^3), high-resolution (3.0×3.0×3.2 mm^3 for metabolites and 2.0×2.0×3.2 mm^3 for water) imaging within

the same scan time (8 minutes) via using a rapid spatiotemporal readout on slice direction and employing a higher sparse sampling strategy. Given these data acquisitions, the key processing and reconstruction issues included (1) separation of signals from water, lipid, and metabolites, (2) reconstruction from the sparse and noisy measurements, and (3) correction of effects and artifacts brought by various system imperfections. The first two processing issues were addressed using a union-of-subspaces model with subspace learning strategies, and the last issue was resolved by utilizing information derived from the unsuppressed water signals and several navigator signals embedded in the data acquisition.

To demonstrate the feasibility and performance of the proposed method, *in vitro* experiments and *in vivo* experiments were carried out on a standard spectroscopic phantom and healthy volunteers, respectively. Given those technical advances, the proposed method successfully showed good accuracy and reproducibility in phantom experiments and obtained high-quality, high-resolution brain metabolite maps from healthy subjects. Moreover, the presented method was also applied for clinical tumor imaging to demonstrate its values in clinical environments. The feasibility studies showed its impressive imaging capability in capturing metabolic alterations in small-size tumors, imaging intra-tumor heterogeneity, classifying tumors with different grades, and monitoring therapeutic responses. In addition, the improved SPICE method was used for ^{31}P-MRSI at 7T for high resolution mapping of high-energy metabolites. Experimental results also showed significantly advanced performance of the proposed method in generating high-resolution, high-quality ^{31}P metabolite maps.

In this thesis research, the feasibility of fast high-resolution MRSI at both 3T and 7T was successfully demonstrated. The described method is expected to provide a very powerful imaging tool in practical environments for a wide range of scientific and clinical applications.

ACKNOWLEDGEMENTS

When looking back at the journey of my graduate study at University of Illinois, I feel so blessed. The people I have encountered, the research I have been working on, the time and efforts I spent here, the experience I have gone through, will all be valuable treasures to me for my future life and career. I would like to express my deepest and sincerest appreciation to all the people and things making up such an unforgettable journey for me the past six years.

I would like to thank my parents and my brother. It was their love and support that gave me enough courage and determination to pursue graduate study overseas, allowed me to focus on career and research during the whole process, and helped me hang in there even in the toughest times.

I would like to thank Prof. Zhi-Pei Liang, even though I can never thank him enough. I often feel fortunate to have the opportunity to have Prof. Liang as my advisor. His passion and capability on research, vision on the scientific field and society, profession in academia, wholehearted support and guidance for students, always inspired me and shaped me into who I am. He is our role model, our advisor, our family, and our friend.

I would like to thank my lab-mates, especially Yudu Li and Yibo Zhao, who have been here with me almost for the entire PhD process. It was their constant support in research that has made a lot of our work possible, and it was their company that has made the time here so enjoyable. Appreciations are also given to other current and previous group members, Wen Jin, Ruihao Liu, Jiahui Xiong, Ziyu Meng, Yang Chen, and many names not listed here. Thanks for their contribution to this inspiring and family-like group environment, which is really unique.

I would like to thank my girlfriend Yixin Chen, and friends Wenxi Fan, Chang Hu, Yiliang Wang, Tiancheng Qin, Zhuoluo Xiang, Yi Yang, Lanxin Shen, Tianyi Shan, and many names not listed here. Their companionship has brought me so many memorable and special moments in this small town.

I would like to thank our group alumni, Drs. Fan Lam, Chao Ma, Bryan Clifford, and Peng Xi, who have shared their experiences and gave me very valuable guidance and help along the way. Their success has also often encouraged me to keep the momentum.

I would also like to show my gratefulness to the support on our research from Dr. Brad Sutton, Dr. Patricia Jones, Dr. Jeffrey Moore, Dr. Tracey Wszalek, Dr. Aaron Anderson, Nancy Dodge,

and Holly Kelleher of Beckman Institute and Biomedical Imaging Center. It was the fantastic fertilities, resources, and research environment that made our work possible. I would also like to thank many collaborators who have made our work more impactful, especially Drs. Yao Li, Jie Luo, Wei Chen, Xiao-hong Zhu, Tianyao Wang, Miao Zhang, Pallab Bhattacharyya, and many names not listed here.

Finally, I would like to thank my doctoral committee members, Professors Zhi-Pei Liang, Brad Sutton, Michael Oelze, and Xin Yu, for their time and suggestions on my thesis research.

TABLE OF CONTENTS

CHAPTER 1 – INTRODUCTION

1.1 Motivation

Brain metabolism links neural activity, energy consumption, blood flow, brain functions, and health status [1]–[3]. Imaging brain metabolism is central to understanding brain function and characterizing brain health states, which have long been desired by both researchers and clinicians. Over decades of development, metabolic imaging methods such as positron emission tomography (PET), magnetic resonance spectroscopy (MRS), and optical imaging have provided valuable tools to probe the distribution of many metabolites and their related metabolic processes in the brain [4]–[7]. For example, with specific tracers, PET has been used to map glucose consumption, oxygenation extraction, and dopamine metabolism of the brain. With this imaging capability, PET has been applied in the diagnosis of various diseases including brain tumors, Alzheimer's disease, and Parkinson's disease [8], [9]. Magnetic resonance spectroscopic imaging (MRSI) is another well-known metabolic imaging method. Without any injection of radioactive isotopes, MRSI can use the intrinsic signals from brain tissues to map numerous metabolites, such as N-Acetylaspartate (NAA), creatine (Cr), choline (Cho), myo-inositol (Ins), glutamine (Gln), and glutamate (Glu) using ^{1}H-MRSI, and phosphocreatine (PCr), adenosine triphosphates (ATPs), Nicotinamide adenine dinucleotide (NAD), and inorganic phosphate (Pi) using ^{31}P-MRSI. Due to the radiation-freeness and easy-accessibility, MRSI has long been regarded as a promising imaging tool for non-invasive *in vivo* metabolic studies and clinical diagnosis [6], [10]. Its invention dates back to the early stage of magnetic resonance imaging (MRI) [11]–[13]. Through several decades of development, MRSI has shown its great potential and value in many studies such as energy consumption analysis, tumor characterization, and neurodegeneration assessment.

However, its development and clinical applications were much more limited than expected since the practical utility was restricted due to several long-standing technical obstacles:

- Low signal-to-noise ratio (SNR): The concentrations of most MR detectable metabolites in the human brain are on the order of millimolar (mM), which is around three orders of magnitude lower than the concentration of water molecules. Therefore, the detection sensitivity of these metabolites is extremely low given the weak signals buried in the thermal noise.
- Long scan time: Typical MRSI methods needs to encode four dimensions of the signal functions, including three spatial dimensions and one spectral dimension, which require a huge

number of measurements. In addition, given the low SNR of metabolite signals, usually many averages are applied in practice to gain enough SNR, which further prolongs the scan time. For example, traditional ^{1}H-MRSI methods usually take more than 10 minutes to scan only one slice, which is far from practically feasible for three-dimensional (3D) imaging of the brain.

- Low spatial resolution: Limited by the low SNR and long scan time, typical MRSI methods can only acquire a small number of spatial encodings, resulting in a very low spatial resolution. The spatial resolution for typical ^{1}H-MRSI methods is around one cm^3. This large voxel size makes these methods suffer from severe partial volume effects and not be able to resolve spatial metabolic heterogeneity.
- Nuisance signals: Specially for ^{1}H-MRSI, another big challenge it faces is the overwhelming water and lipid signals (which are called nuisance signals). Since signals of water and lipids are more than three orders of magnitude higher than the metabolite signals, metabolite signals are hardly visible in the spectra of ^{1}H-MRSI without any suppression or processing. Therefore, insufficient separation between nuisance and metabolite signals can result in significant artifacts and quantification errors for metabolite signals.

Given these barriers, it has been very challenging to perform 3D high-resolution MRSI experiments in a clinically feasible time. Therefore, even with the capability to obtain scientifically and clinically desirable information, the applications of MRSI methods in practical environments are still very limited.

During the past several decades, numerous efforts have been made to address these challenges and promote MRSI technology. In data acquisition, special excitation pulses for good localization [14]–[16], suppression pulses for reducing nuisance signals [17]–[19], and fast trajectories for rapid spatiospectral encoding have been developed [20]–[22]. Moreover, the advances in parallel imaging and compressed sensing have enabled sparse sampling of the signal space, which can further reduce the acquisition time [23]–[25]. Various processing methods have also been proposed for effective denoising, high-quality reconstruction, and accurate spectral quantification [26]–[33]. In recent years, a subspace based MRSI technique called SPICE (SPectroscopic Imaging by exploiting spatiospectral CorrElation) has been proposed for accelerated ^{1}H-MRSI at 3T [34]–[36]. SPICE technique exploits a unique property known as partial separability (PS) or low-rank structure of spectroscopic signals [33]. This property reveals that high-dimensional spectroscopic signals reside in a very low-dimensional subspace, and it has enabled special data acquisition and

processing schemes to significantly accelerate MRSI. The proof-of-concept works using the basic SPICE method on ^{1}H-MRSI at 3T have demonstrated its superior performance on improving imaging speed, resolution, and SNR [34]–[36]. However, the imaging capability of these "prototype" methods in terms of imaging volume, resolution, and speed, is still not sufficient to satisfy the ever-growing clinical needs.

Ultrahigh field MR ($\geq$ 7T) has drawn more and more attention in recent years. The most direct benefit brought by ultrahigh field MR is the significantly enhanced signal intensity, which enables higher resolution for various MR imaging techniques [37]–[40]. The relaxation times change in ultrahigh field MR compared with low field MR, such as longer T_1, shorter T_2 and T_2*. These changes of relaxation times can lead to higher contrast-to-noise ratio (CNR) for functional MRI (fMRI) and better image contrast for structural imaging like MPRAGE (Magnetization Prepared Rapid Acquisition Gradient Echo) and SWI (Susceptibility Weighted Imaging) [41]–[45]. Specially for MRSI, ultrahigh field MR not only provides enhanced SNR, but also offers increased chemical shift dispersion for better separation of different molecules. Ultrahigh field MR has shown great potential to enhance the MRSI imaging capability [46]–[50].

This thesis research aims at leveraging these progresses and further developing the SPICE method to provide a more powerful MRSI image technique with sufficient spatial resolution and imaging speed for clinical environments (at 3T). This thesis research also aims at utilizing the unique benefits brought by ultrahigh field MR to further enhance the imaging capability of high-resolution MRSI at 7T.

1.2 Main Results

In this thesis research, we achieved the following main results:

- We proposed a novel data acquisition sequence for ultrafast high-resolution ^{1}H-MRSI at 3T. The proposed sequence significantly improves the previous basic SPICE method, and it is characterized by several unique acquisition features, including FID (free induction decay)-based acquisition with ultrashort TE (echo time) and short TR (repetition time), elimination of water and lipid suppression pulses, fast simultaneous spatiotemporal trajectories, and highly sparse sampling of data space in variable density. As a result, 3D metabolite imaging (field of view (FOV): 240×240×72 mm^3) at 2.0×3.0×3.0 mm^3 nominal resolution could be obtained in an 8-minute scan at 3T MR systems. Furthermore, since no water suppression pulses are

applied, the proposed pulse sequence can also obtain high-resolution water imaging at $2.0\times1.0\times1.0$ mm^3 simultaneously in the same scan, from which anatomical imaging, quantitative susceptibility mapping (QSM), and quantitative T_2* mapping can be generated.

- This data acquisition sequence was further developed at ultrahigh field (7T). Utilizing the SNR benefits of ultrahigh field, the sequence at 7T was extended to achieve whole-brain high-resolution MRSI within the same time. More specifically, the sequence kept acquisition features including FID acquisition and no water suppression, but changed the readout direction to slice direction, and employed sparse sampling with a higher acceleration factor. As a result, whole brain (FOV: $240\times240\times160$ mm^3) metabolite imaging at $3.0\times3.0\times3.2$ mm^3 nominal resolution and water imaging at $2.0\times2.0\times3.2$ mm^3 were obtained simultaneously in an 8-minute scan. Furthermore, the unsuppressed water signals were used for correcting the effects caused by various challenging system imperfections at ultrahigh field.
- The key processing issues given the proposed data acquisition schemes included (1) separation of signals from water, lipid, and metabolites; (2) reconstruction from the sparse and noisy MRSI data; and (3) correction of system imperfection. The union-of-subspaces framework of SPICE was used to address the first two processing issues. This model is able to significantly reduce degrees-of-freedom for representing the spatiospectral functions, facilitate effective reconstruction from sparse and noise measurements, and allow good separation of signals between different molecules. In this thesis research, the basis functions for different molecules were generated using subspace learning strategies, pre-determined from quantum simulation and sets of high-quality training data. The feasibility of addressing these processing issues and producing high quality reconstruction results were successful demonstrated. The third issue was resolved using the unsuppressed water signals and embedded navigator signals in the sequence. Successful resolve of these issues not only made the SPICE technique practically possible, but also provided a set of valuable tools and solutions to many common issues in other MRSI methods.
- Both phantom experiments and *in vivo* experiments were carried out to demonstrate the feasibility and potential of the proposed method for fast high-resolution ^{1}H-MRSI. At 3T MR platforms, the proposed method successfully achieved metabolic imaging at $2.0\times3.0\times3.0$ mm^3 nominal resolution and water imaging at $2.0\times1.0\times1.0$ mm^3 with an FOV of $240\times240\times72$ mm^3 within an 8-minute scan time. It produced accurate and reproducible results in the phantom

experiments and achieved high-quality, high-resolution results in experiments on healthy subjects. The proposed method was also performed on patients diagnosed with various grades of brain tumors. Results from these feasibility studies have showed great potential values of the proposed method in tumor imaging with the capabilities to capture metabolic alterations in small-size tumors, map intra-tumor heterogeneity, and monitor therapeutic responses. At 7T MR platforms, the proposed method further extended the FOV to whole brain coverage ($240\times240\times160$ mm^3) and achieved metabolic imaging at $3.0\times3.0\times3.2$ mm^3 nominal resolution and water imaging at $2.0\times2.0\times3.2$ mm^3 resolution within the 8-minute scan time. Encouraging high-quality experimental results were also obtained successfully in both phantom and *in vivo* scans, showing the feasibility and performance of the proposed method.

- The presented SPICE method was also adapted to ^{31}P-MRSI at 7T for high resolution mapping of energy metabolites. An optimized ^{31}P-MRSI sequence featured by FID acquisition with short TE and TR, NOE (Nuclear Overhauser Effect) enhancement module, and SNR efficient data space sampling was used. Using the subspace-based method for denoising, high quality 3D metabolite maps ($220\times220\times100$ mm^3) at $9.1\times9.1\times12$ mm^3 nominal resolution were obtained in a 30-minute scan, successfuly revealing metabolite contrast between gray matter and white matter.

1.3 Organization of the Dissertation

The dissertation is organized as follows:

Chapter 2 reviews some basic background knowledge related to this thesis work. At first, overall background about brain metabolic imaging including its significance and current progress on imaging methods are discussed. Then technical essentials including MR physics, MRSI basic principles, accelerated acquisition approaches, and mathematical foundation of subspace modeling (known as partial separability model) follow. After these, basic concept and early work on the SPICE method for MRSI are introduced. Progress, benefits, challenges, and potentials of ultrahigh field MR are discussed at the end of this chapter,. Chapter 3 describes the detailed design of the proposed fast high-resolution ^{1}H-MRSI acquisition sequence at 3T, including the specifically designed features in pulse sequence, the pattern of sparse sampling on the data space, embedded navigator signals' acquisition, and experimental implementation. Similarly, Chapter 4 describes the data acquisition sequence at 7T, particularly on features to utilize the signal enhancement for

whole-brain coverage and to overcome the specific technical challenges brought by ultrahigh field. Example implementation of this sequence is also described at the end of this chapter. Chapter 5 introduces the data processing methods based on the union-of-subspaces model and subspace learning strategies. The essentials of signal model, subspace learning procedure, reconstruction of water, lipid, and metabolite signals, and the correction of system imperfection are covered in this chapter. Chapter 6 presents the experimental results obtained both *in vitro* and *in vivo*, at both 3T and 7T, demonstrating the performance and potential of the method for high-resolution metabolite mapping. Results from a feasibility study applying the proposed method for tumor imaging are also included. Chapter 7 introduces application of the subspace imaging method in high-resolution ^{31}P-MRSI, including acquisition sequence optimization, data processing and reconstruction methods, and experimental results. Chapter 8 concludes this dissertation and discusses future research directions built on this work. In the following chapters of this dissertation except Chapter 7, "MRSI" refers to "^{1}H-MRSI" if no specific classification is given.

CHAPTER 2 – BACKGROUND

2.1 Metabolic Imaging of the Brain

The human brain consists of a huge number of cells which closely and continuously interact with each other through complex chemical and electrical activity. There are various metabolic processes simultaneously happening in the brain to facilitate brain functionality. The metabolism can be divided into catabolism and anabolism. In catabolism, large complex molecules are transformed into small ones through breakdown processes, which releases energy to support the communication and function of cells. The anabolic processes consume energy to synthesize more complex molecules, which are used for building cellular structures and storing energy. These metabolic processes support and mediate numerous brain cellular functions, including gene expression, protein expression and translation, generation and propagation of action potential, synaptic transmission, metabolites recycling, and so on. Therefore, probing brain metabolism and imaging distribution of metabolites are central to understanding how brain's anatomy and physiology respond to environment, diseases, injury, and aging [51].

Regulation of brain metabolite supply and energy metabolism is essential to maintain normal brain functionality, while physiological or pathological processes usually activate or deactivate some specific metabolic pathways, thus lead to abnormal changes of metabolite concentrations [2], [3]. For example, glutamate is the primary excitatory neurotransmitter and gamma-aminobutyric acid (GABA) is the main inhibitory neurotransmitter, both of which work together to regulate the normal neurotransmission processes [52]. In glutamatergic synapses, glutamate is released by the pre-synaptic neuron, and its uptake by the post-synaptic neuron via glutamate receptors stimulates the change of action potential, which leads to communication between neurons. On the contrary, GABA limits nerve transmission by decreasing action potential and blocking stimulation of neurons, thus modulating the overall neural communication. The imbalance of glutamate and GABA could cause abnormality or dysfunction of neurotransmission, which has shown to be correlated with many mental disorders such as schizophrenia, anxiety disorders, and depression [53]–[58]. There are several MR detectable metabolites playing central roles in the brain energy metabolism, such as glucose (Glc), ATPs, and lactate (Lac) [51]. Glucose is an energy substrate which produces ATPs through glucose oxidation and glycolysis. Most of the energy consumed by the human brain is produced from glucose, so it has been regarded as the

most essential metabolic fuel for the brain. The overall glucose level and flux rate are kept in a dynamic balance in normal brains; severe reduction of brain glucose level could quickly lead to disease states like cognitive dysfunction, loss of consciousness, seizures, or irreversible brain damage. ATP is the primary source of biochemical energy, and its expenditure devotes to maintain cell integrity, keep tissue viability, support electrophysiological activity, and facilitate neural communication. PCr functions as an alternative energy reserve, which can provide an additional ATP supply through a phosphorylation-dephosphorylation reaction when the energy requirement cannot be met by oxidative phosphorylation. When sufficient oxygen is present, the pyruvate generated from glucose is fully oxidized to carbon dioxide and water through the tricarboxylic (TCA) cycle, while the pyruvate is reduced to lactate when oxygen is lacking. In many disease states, the pathways to production of lactate are strongly enhanced, such as ischemia and cancer. Hence, sudden lactate increase in the brain has been regarded as an indicator for abnormality. Many diseases also usually come with reduction of NAA, which is one of the metabolites with the highest concentrations in the brain (around 10 mM in some brain regions). NAA is a nervous system-specific metabolite, which is synthesized from aspartate and acetyl-coenzyme A. It has been found to play multiple roles in brain biochemical processes, including involvement in myelin lipid turnover, link to ATP metabolism in neuronal mitochondria, and as a precursor for the enzymatic synthesis of N-acetylaspartylglutamate (NAAG), the third most prevalent neurotransmitter in the human brain [59]. Additionally, NAA has long been regarded as a marker of neuronal density, and its decreases associated with those neuropathologies are interpreted to represent loss of neurons [59]. Another prominent brain metabolite, choline, is specially associated with cancer metabolism, like oncogenesis, tumor progression, and proliferation. The “Cho” signal in ^{1}H-MRS actually contains multiple choline-containing compounds, such as free choline, glycerophosphorylcholine, and phosphorylcholine, so it is also often referred as “total choline”. Choline-containing metabolites are involved in cell membrane synthesis and degradation, so the elevated Cho in brain tumors is suggested to indicate high cellularity, cell destruction, and increased brain membrane turnover [60].

Since these brain metabolites participate in numerous aspects of the brain metabolism, being able to map them can provide a valuable window to study brain metabolism and probe how the brain responses to various environmental conditions. After decades of effort on the development of imaging methods, recent state-of-the-art non-invasive metabolic imaging tools like PET and

MRS/MRSI have been successfully applied in many brain imaging applications, showing great potential and clinical values. Three representative metabolic imaging tools including ^{18}FDG-PET, ^{1}H-MRS/MRSI, and ^{31}P-MRS/MRSI are discussed as follows.

2.1.1 ^{18}FDG-PET

Positron emission tomography has been currently regarded as one of the most common metabolic imaging tools. As the name suggests, PET is a technique that depends on the positron emitted from the object and utilizes it for imaging. More specifically, PET requires injection of radiotracers which are chemical molecules labeled by radioactive positron emitting isotope. After injection, the PET tracers concentrate in the tissues of interest through blood circulation and undergo positron emission decay. The emitted positron travels in tissue shortly and then annihilates with an electron, producing a pair of gamma photons moving in the opposite directions (approximately). These emitted gamma photons can be collected by the detectors distributed around the PET scanner and then produce signals. PET requires coincident detection of the pair of photons in opposite directions, which allows localization of the emission event in post processing. By determining the lines where the coincident events happen and collecting data emitting by many angles, PET can obtain spatial maps of the labelled metabolites through reconstruction. Since the radioactive isotopes can be used to label various biochemical molecules like glucose, ammonia, and water, PET is able to measure the distribution and changes of targeted molecules in metabolic processes or physiological activities.

2-[18F]-fluoro-2-deoxy-D-glucose (^{18}F-FDG) is the most widely used PET tracer, which is a glucose analog. After injection, FDG is transported into living tissues at a similar rate as glucose, then it is phosphorylated to FDG-6-phosphate while it does not enter further metabolic pathways. Therefore, FDG uptake reflects the uptake of glucose, so it has been widely used for measuring glucose metabolism. ^{18}FDG-PET imaging has been applied in a wide range of applications including investigating neurofunction, neurodegenerative diseases, and oncology. For functional imaging, ^{18}FDG-PET quantitatively measures cerebral metabolic rates of glucose (CMRglu), whose consumption is directly related to physiological stimulation of the neurons, thus it can effectively probe the spatiotemporal correlation between the metabolic changes and hemodynamics. Since CMRglu is closely related to the brain functional state, ^{18}FDG-PET has also been successfully applied in numerous neuropsychiatric and neurodegenerative diseases including traumatic brain injury (TBI), schizophrenia, depression, bipolar disorder, Alzheimer's disease, and

Parkinson's disease [61]–[66]. Given the fact that cancer cells usually have increased glucose uptake and glycolysis to support their abnormal growth, ^{18}FDG-PET has shown its advantages and values in tumor diagnosing, staging, monitoring, evaluating and even prognosis of various malignancies [5], [8], [67]. Over decades of development, ^{18}FDG-PET has been well-accepted and widely employed as one of the standard imaging techniques for oncology scans in both scientific research and clinical environments.

Besides ^{18}FDG, there have been many other PET tracers developed to probe in different aspects of human metabolism. For example, ^{15}O-water, which is a water analog, has been utilized to measure regional cerebral blood flow and oxygen consumption; ^{18}F-Fluorodopa can be used for measuring dopamine synthesize, which has shown great values for schizophrenia, Parkinson's disease, and brain tumors; ^{13}N-Ammonia is regarded as excellent blood flow agent and has been widely used for quantification of myocardial blood flow; it is also related to glutamine metabolism so used for diagnosis of astrocytoma; ^{11}C-Methionine is related to amino acid uptake and protein synthesis, so it is mainly applied in brain tumors and myocardium infarction.

2.1.2 ^{1}H-MRS/MRSI

MR spectroscopy/spectroscopic imaging are imaging techniques based on the magnetic resonance phenomenon. Different molecules have different electronic structures, thus different shielding effects on nuclei which are reflected as different resonance frequencies in MR signals. MR scanners use RF pulses to excite the imaging object and receive MR spectroscopic signals as sum of all these frequency/molecule components. Through special post-processing and reconstruction methods, MRS/MRSI can resolve different molecules from the overall spectroscopic signals. MRS usually refers to methods measuring spectroscopic signals from a single voxel, while MRSI are methods measuring spatially resolved spectra, thus obtaining the spatial distribution or mapping of different molecules. More details of MRS/MRSI methods will be introduced in section 2.2.

^{1}H-MRS/MRSI methods measure MR signals from protons. An illustration of ^{1}H-MRSI and typically detectable molecules are shown in Figure 2.1. The number of metabolites measurable by typical ^{1}H-MRS/MRSI techniques is more than ten. The most widely investigated metabolites include NAA, creatine, choline, myo-inositol, glutamate, glutamine, GABA, lactate, etc. These metabolites have been proved valuable in many applications and studies. For example, NAA, Cho, and Lac have been used as good biomarkers for brain tumor imaging, with close relation to tumor grading, characterization, and treatment responses [68]; NAA and Lac have been used in ischemia

for lesion identification and assessment of tissue salvageability [69]; neurotransmitters including Glu and GABA are critical in various functional studies, especially in investigation of their metabolic changes in response to stimulation activity [70]; moreover, Glu and GABA have shown great potential in diagnosis and characterization of a bunch of neuropsychiatric diseases like schizophrenia and depression [53]–[58]. ^{1}H-MRS/MRSI allows detection and measurement of all these molecules within a single scan without any injection, so it has been regarded as a very useful investigative metabolic imaging tool.

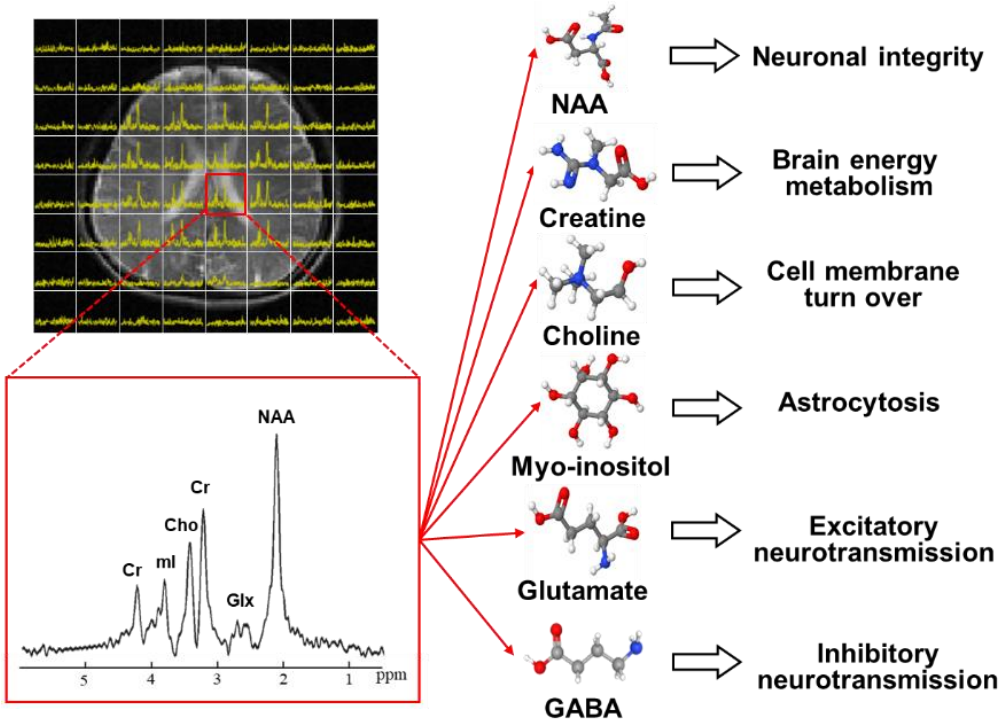

Figure 2.1: Illustration of ^{1}H-MRSI in obtaining distributions of multiple molecules from the spatially resolved spectra. The main detectable molecules (including NAA, Cr, Cho, Ins, Glu, GABA, etc.) are involved in specific biological process, thus indicate different aspects of the brain metabolism.

However, concentrations of these metabolites in the human brain are very low, usually on the order of a few mMs. Moreover, MR-based methods have fundamentally limited sensitivity and acquisition efficiency compared with PET imaging from physics. Sensitivity issue is one of the most severe technical challenges ^{1}H-MRS/MRSI methods face, limiting its resolution, imaging speed, accuracy, and practical impact. Recent technical advances to overcome this issue will be elaborated in later sections of this thesis.

2.1.3 ^{31}P-MRS/MRSI

Similar to ^{1}H-MRS/MRSI, ^{31}P-MRS/MRSI utilizes tissue intrinsic spectroscopic signals to measure multiple phosphorus metabolites. Different from the metabolites measurable by ^{1}H-MRS/MRSI, many detectable phosphorus metabolites are involved in cellular energetic processes and membrane phospholipids. As a representative MR spectrum shown in Figure 2.2, the typically measurable phosphorus metabolites of human brain include PCr, ATPs (split into three resonances, α-ATP, β-ATP, and γ-ATP), NAD (integration of NADH and NAD+), Pi (including exocellular and intracellular Pi), phosphocholine (PC), phosphoetanolamine (PE), glycerophosphocholine (GPC), and Glycerophosphoethnolamine (GPE) [71]. Given this rich set of metabolites which are closely related to bioenergetics, ^{31}P-MRS/MRSI is regarded as one of the most powerful imaging tools to study brain energy metabolism.

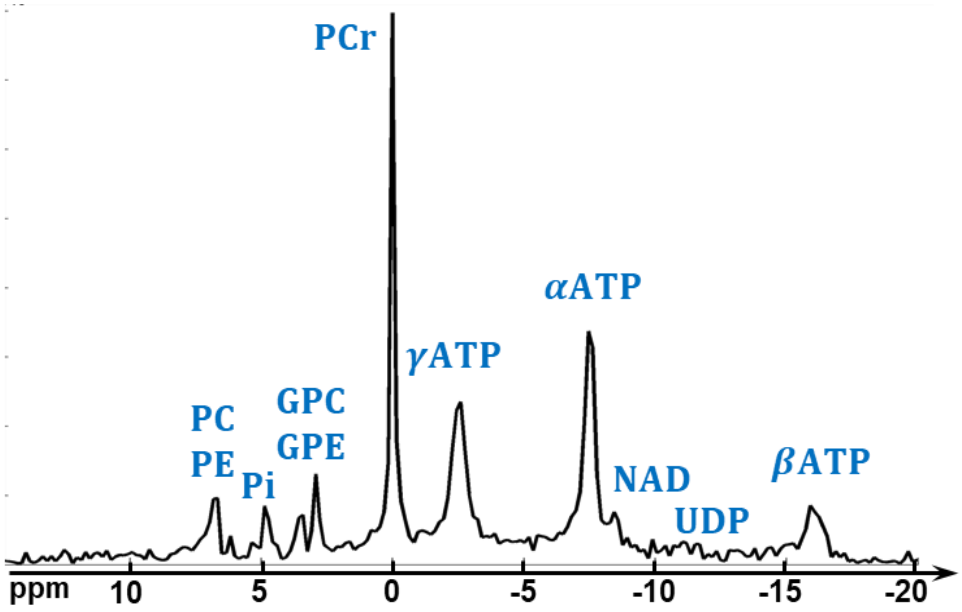

Figure 2.2: Representative 31P-MR spectrum of human brain. The detectable phosphorus molecules can provide biological information regarding energy metabolism and membrane phospholipids.

Measurement of PCr and ATPs using ^{31}P-MRS/MRSI in human brain has been utilized to characterize and understand the energetic processes in both healthy and diseases states. Since many disorders are related to imbalances in bioenergetics processes, ^{31}P-MRS/MRSI has been used in numerous studies to investigate energetic impairments in neural disorders like Alzheimer's disease, multiple sclerosis, migraine, epilepsy, and cerebral ischemia [72]–[74]. It has also been found that

the phosphomonoesters (PC and PE) and phosphodiester (GPC and GPE), which are related to cell membrane phospholipids, are important biomarkers for aging and psychiatric illness like schizophrenia [75]. Another important application of ^{31}P-MRS/MRSI is to measure tissue PH value using the chemical shift of Pi. It is known that PH value presents abnormality in tissues with several disease states, hence ^{31}P-MRS/MRSI has also been applied in PH investigations of some diseases like brain tumors and depression disorders.

Compared with ^{1}H-MRS/MRSI, ^{31}P-MRS/MRSI has a few advantages. First, phosphorus spectrum has a wider bandwidth spanning around 30 ppm (only around five ppm for proton spectrum), so the phosphorus metabolites have much less spectral overlapping with others and their separation is considerably easier. Another major advantage is that ^{31}P-MRS/MRSI does not have huge nuisance signals like water and lipids in proton spectrum, which largely simplifies the acquisition and processing of ^{31}P-MRS/MRSI data. However, the sensitivity of phosphorus signals is considerably lower than proton, given its lower gyromagnetic ratio and lower metabolite concentrations. Therefore, the resolution and imaging speed of ^{31}P-MRS/MRSI methods are more limited than ^{1}H-MRS/MRSI methods, which have largely limited its practical utility.

Comparing these metabolic imaging tools, each one has its own strength and weakness. PET imaging has the advantage of superior signal sensitivity compared with MRS/MRSI methods. The molecular sensitivity of typical PET and MR methods are around 10^{-11} mol/L and 10^{-6} mol/L, respectively. And PET imaging is naturally quantitative while MRS/MRSI methods are not, which need external or internal reference for absolute quantification. However, most of the PET tracers have short half-life, so a cyclotron is usually needed near the clinical site, which has limited the widespread applications. MRS/MRSI methods do not require the injection of radioactive isotopes, thus providing simpler experimental operation and harmlessness to examined subjects. Moreover, MRS/MRSI methods are able to simultaneously map multiple metabolites in a single scan, which is currently impossible for PET. In a practical aspect, MR scanners have much better accessibility compared with PET scanners, making MRS/MRSI a compelling non-invasive metabolic imaging tool in practice.

2.2 Magnetic Resonance Spectroscopic Imaging

This section introduces some basic concepts of MR physics and basic principles of MRSI.

2.2.1 Nuclear magnetic resonance and signal formulation

The generation of MR signals is based on the well-known nuclear magnetic resonance (NMR) phenomenon. As the name suggests, NMR involves nuclei in the object, magnetic fields, and resonance phenomena. It is known that any imaging objects can be broken down into molecules, then atoms, then to nuclei and surrounding electrons. A nucleus with odd atomic numbers has a nonzero angular momentum usually called nuclear spin (denoted as $\vec{J}$). The nucleus with non-zeros spin generates magnetic moment as:

$$\vec{\mu} = \gamma \vec{J} \tag{2.1}$$

where the constant γ is known as the gyromagnetic ratio, and it is nucleus dependent. Each nuclear spin has its magnetic moment with specific magnitude and direction. The net magnetization of the imaging object is the vector sum of the magnetic moment of all the nuclear spins in the object.

$$\vec{M} = \sum_{n=1}^{N_s} \vec{\mu}_n \tag{2.2}$$

where $\vec{M}$ is the bulk magnetization of the whole object, $\vec{\mu}_n$ the magnetic moment of nth nuclear spin and N_s the total number of spins in the object, which is normally much more than 10^{26} in the human brain. At thermal equilibrium, when no external magnetic field is present, the net magnetic moment is zero since the directions of spins are arbitrary due to thermal random motion. When the object is exposed to a strong external magnetic field B_0 (assuming the direction is in z direction), according to the theory of quantum mechanics and Boltzmann distribution, the bulk magnetization is along the same direction as B_0 and the magnitude is:

$$M_z^0 = \frac{\gamma^2 \hbar^2 B_0 N_s I(I+1)}{3KT_s} \tag{2.3}$$

where γ is the gyromagnetic ratio, $\hbar$ is Planck's constant ($\hbar = h/2\pi$, $h = 6.626 \times 10^{-34}\, J \cdot s$), N_s is the total number of spins, I is the nuclear spin quantum number, K is the Boltzmann constant ($1.38 \times 10^{-23}\, J/K$), T_s is the absolute temperature of the spin system. For ^{1}H (spin-$1/2$ system), $\gamma = 2\pi \times 42.58$ MHz/T, and the bulk magnetization is:

$$M_z^0 = \frac{\gamma^2 \hbar^2 B_0 N_s}{4KT_s} \tag{2.4}$$

Bulk magnetization M_z^0 which determines the sensitivity of NMR experiments points along the direction of B_0, and the transverse component is zero at equilibrium. To generate NMR signals from such a polarized sample, precession motion needs to be generated. In other words, the longitudinal magnetization needs to be transformed onto the transverse plane. In modern MR experiments, an additional magnetic field is needed to apply, which varies with time and oscillates in radiofrequency (RF) range, known as $B_1(t)$. During the RF pulse, the magnetization precesses on B_0 and B_1. For simplicity, assuming frequency of the B_1 field matches the resonance condition, the frequency is the same as the Larmor frequency of the spin system:

$$\omega_1 = \omega_0 = \gamma B_0 \tag{2.5}$$

The time-dependent behavior of $\vec{M}$ during the application of B_1 field could be described quantitatively using the Bloch equation which takes the following form in MR context:

$$\frac{d\vec{M}}{dt} = \gamma\vec{M} \times \vec{B} - \frac{M_x\vec{\imath} + M_y\vec{\jmath}}{T_2} - \frac{(M_z - M_z^0)\vec{k}}{T_1} \tag{2.6}$$

where $\vec{B}$ includes both B_0 and B_1 field ($\vec{B} = \overrightarrow{B_0} + \overrightarrow{B_1}$); $\vec{\imath}$, $\vec{\jmath}$ and $\vec{k}$ are unite vectors of the coordinates x, y, z respectively; M_z^0 is the thermal equilibrium value of bulk magnetization as described above; T_1 and T_2 are the longitudinal and transversal relaxation times, respectively. After typical RF excitation, a transverse magnetization component will be generated, which rotates around B_0 at Larmor frequency and can induce voltage signals in the receiver coil according to Faraday law of electromagnetic induction and the principle of reciprocity. More specifically, the voltage induced in the receiver coil is determined by:

$$V(t) = -\frac{\partial}{\partial t}\int \overrightarrow{B_r}(\boldsymbol{r}) \cdot \vec{M}(\boldsymbol{r}, t)d\boldsymbol{r} \tag{2.7}$$

where $\overrightarrow{B_r}(\boldsymbol{r})$ is receiver sensitivity on location $\boldsymbol{r}$ and the integral is on the whole object. This voltage signal is often referred as raw NMR signal. Under modern MRI detection scheme (phase-sensitive detection with signal demodulation), the signal detected by the MR scanners can be expressed as:

$$S(t) = \omega_0 e^{i\pi/2}\int B_{r,xy}^*(\boldsymbol{r})M_{xy}(\boldsymbol{r}, 0)e^{-t/T_2(\boldsymbol{r})}e^{-i\Delta\omega(\boldsymbol{r})t}d\boldsymbol{r} \tag{2.8}$$

where ω_0 is the Larmor frequency; $\Delta\omega(\boldsymbol{r}) = \gamma\Delta B(\boldsymbol{r})$ is the frequency of field inhomogeneity; $B^*_{r,xy}$ is the conjugate of $B_{r,xy}$. In this expression, the field inhomogeneity is assumed to be time independent. If the field inhomogeneity is time varying, the term $\Delta\omega(\boldsymbol{r})t$ should be replaced by $\gamma\int_0^t \Delta B(\boldsymbol{r},\tau)d\tau$.

2.2.2 Chemical shift and magnetic resonance spectroscopic imaging

The description in 2.2.1 assumes the object only contains one single type of nuclear spin, so the object only has one resonance frequency which is determined by Equation (2.5). However, in the real world, the resonance frequency not only depends on gyromagnetic ratio and the main B_0 field, but also depends on chemical environment of the nucleus, which is usually referred to as chemical shift. More specifically, there are electrons surrounding the nucleus, which rotates in the opposite direction to the nuclear spin precession when placed in the main B_0 field. This precession of electrons generates an associated magnetic moment opposite to the nuclear magnetic moment, which is analogous to a shielding of nucleus. The "effective" resonance frequency of the nucleus under this shielding effect can be expressed quantitatively in the following form:

$$\omega = \gamma B_0(1-\sigma) \tag{2.9}$$

where σ is the shielding constant depending on the chemical environment of the nucleus, and it is usually on the order of a few parts per million (ppm). This frequency shift due to chemical shift phenomenon makes it possible to separate the spectroscopic signals from different molecules based on their frequency differences, which lays the physical foundation of the NMR spectroscopy.

Given a spin system containing spins with different resonance frequencies (assuming a homogeneous sample with homogeneous sensitivity profile), the MR signals generated after a pulse excitation, which is also referred as popular FID signals, take the following mathematical form:

$$S(t) = \int_{-\infty}^{\infty} \rho(\omega) e^{-\frac{t}{T_2(\omega)}} e^{-i\omega t} d\omega \tag{2.10}$$

where $\rho(\omega)$ is the spectral density function characterizing the distribution of different frequency components. In Equation (2,10), the decay rate of FID signal is characterized by T_2 relaxation time, where the magnetic field is ideally homogeneous. In the practical cases where field homogeneity is present, the FID signal would decay faster given the phase cancellation, thus the decay rate

would be characterized by another shorter "effective" relaxation time instead, which is usually denoted as T_2^*. With the capability to probe the distribution of different molecules based on their differences in resonance frequencies, NMR spectroscopy has made significant impact in chemical and biological studies in the past several decades.

Obtaining spatially resolved spectroscopy has long been desired in both scientific research and clinical applications. MRSI is such a technique to obtain and resolve both spatial and spectral information using the MR signals (as illustrated in Figure 2.1). MRSI combines MR spectroscopy with MR imaging, encoding spectral information in the FID/temporal signals and employing gradient fields to encode spatial information, as done in typical MR imaging methods. More specifically, the introduction of gradient fields generates a spatially dependent magnetic field:

$$\Delta B(\boldsymbol{r}, t) = \vec{G}(t) \cdot \boldsymbol{r} \tag{2.11}$$

Then, the signal equation can be revised as:

$$S(t) = \int_V \int_W \rho(\boldsymbol{r}, \omega) e^{-\frac{t}{T_2(\boldsymbol{r},\omega)}} e^{-i\omega t} e^{-i\gamma \int_0^t \vec{G}(\tau)\cdot \boldsymbol{r} d\tau} d\omega d\boldsymbol{r} \tag{2.12}$$

If we introduce $\boldsymbol{k}$ to denote $\boldsymbol{k} = \frac{\gamma}{2\pi}\int_0^t \vec{G}(\tau)d\tau$, use $\omega = 2\pi f$, and add the term for static field inhomogeneity, then the signal equation becomes:

$$s(\boldsymbol{k}, t) = \int_V \int_F \rho(\boldsymbol{r}, f) e^{-\frac{t}{T_2(\boldsymbol{r},f)}} e^{-i\gamma \Delta B(\boldsymbol{r}) t} e^{-i2\pi f t} e^{-i2\pi \boldsymbol{k}\cdot\boldsymbol{r}} df d\boldsymbol{r} \tag{2.13}$$

which is the (k, t)-space data acquired in the MRSI methods (noise term is discarded in the above equation). In this equation, $\rho(\boldsymbol{r}, f)$ is the desired spatiospectral function to map, $s(\boldsymbol{k}, t)$ is the measured MRSI data, V is the volume of interest, and F is the spectral bandwidth. The fundamental imaging problem of MRSI is to recover $\rho(\boldsymbol{r}, f)$ from the measured (k, t)-space data $s(\boldsymbol{k}, t)$.

To collect the MRSI signals $s(\boldsymbol{k}, t)$, as shown in Equation (2.13), both spatial encodings in k-space and temporal encodings in t dimension are needed. The most commonly used pulse sequence for MRSI acquisition is the well-known chemical shift imaging (CSI) method [12]. Essentially, in each excitation after RF pulses, CSI method collects entire FID/temporal signals for t dimension encodings on one specific $\boldsymbol{k}$ space location; then it collects spatial encodings using different phase

encoding gradients in different excitations. Assuming the desired spatiospectral function $\rho(\boldsymbol{r}, f)$ is support-limited and band-limited, CSI method samples both k-space and temporal signals at the Nyquist rate for full recovery without aliasing. With enough number of encodings, direct Fourier reconstruction can be performed to generate a good approximation of $\rho(\boldsymbol{r}, f)$. The CSI method has been used as the gold standard method of MRSI for many years, and it is still widely used in many MRSI studies. However, the spatial encoding efficiency of CSI is very low, with only one spatial encoding in each excitation. Assuming the number of encodings in each spatial dimension is N_x, N_y, N_z, and in temporal dimension is N_t, the total number of excitations needed in CSI for one average would be $N_x \times N_y \times N_z$. Given the low SNR of MRSI signals, many averages are usually needed, leading to a very long scan time. Therefore, most CSI experiments are limited to low spatial resolution and small brain coverage. For example, in human brain experiments, typical CSI methods acquire only one single slice, with resolution around 10 mm (where $N_x = 24$, $N_y = 24$, $N_z = 1$, assuming TR = 1 second) and three averages, then the scan time is already 28.8 minutes. These imaging efficiency and capability are far from sufficient for practical applications in clinical environments. Therefore, acceleration is necessary for MRSI methods.

2.3 Accelerated MRSI

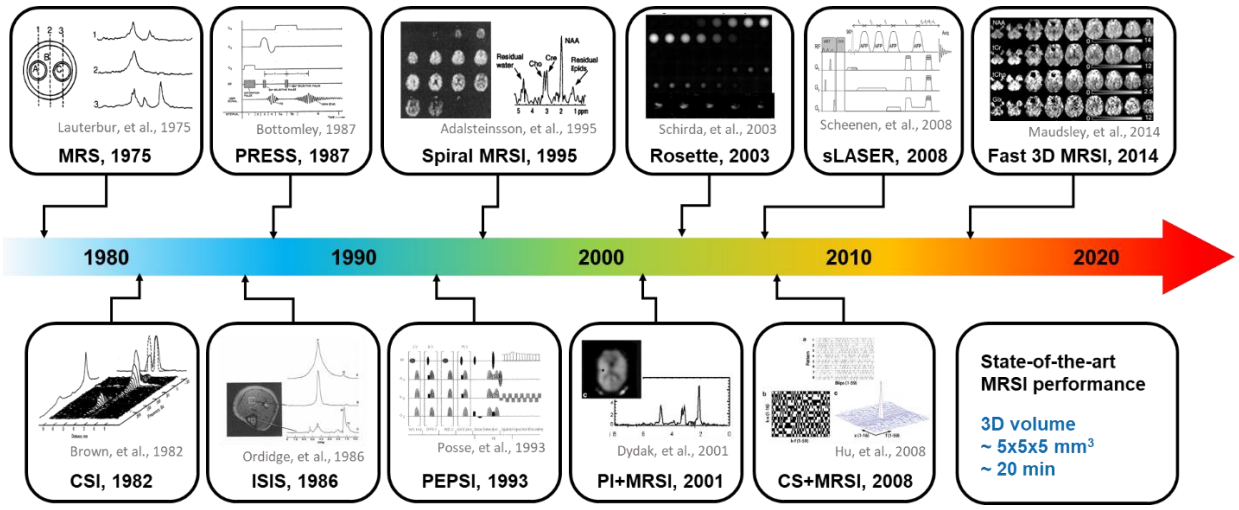

Figure 2.3: A historic illustration of some milestones in the development of MRSI technology.

During the past a few decades, a lot of research efforts from the MR society has been invested to push the development of MRSI methods forward, resulting in many advanced MRSI technologies. A historic illustration of some milestones in the development of MRSI technology is shown in Figure 2.3. In these progresses, a large number of methods were proposed for the acceleration of MRSI. These accelerated MRSI methods can be roughly categorized into methods using fast sampling trajectories and methods using sparse sampling of (k, t)-space.

2.3.1 Fast trajectories

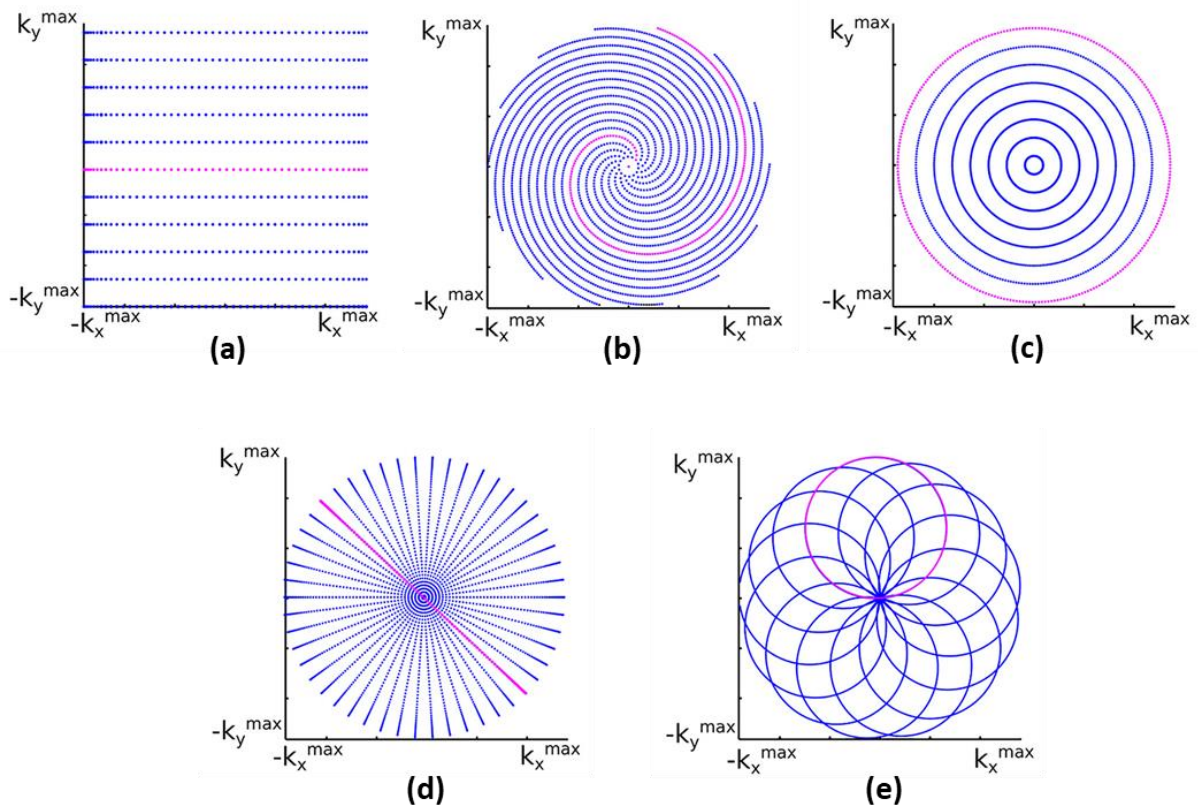

Figure 2.4: Fast sampling trajectories used for MRSI acquisition. (a) EPSI trajectory; (b) spiral trajectory; (c) concentric ring trajectory; (d) radial trajectory; (e) rosette trajectory. This figure is reproduced from [76].

The basic idea of fast sampling trajectories is to use a much higher readout bandwidth to increase the number of readout encodings and utilize these increased encodings to simultaneously sample both spatial and temporal dimensions. The number of spatiotemporal encodings acquired in each excitation increases, then the number of excitations needed could be reduced to shorten the total scan time. For example, traditional ^{1}H-CSI sequences at 3T use a readout bandwidth around 5 kHz.

To accelerate the acquisition, the readout bandwidth can be increased to 200 kHz, increasing the number of temporal encodings by a factor of 40 and these extra encodings can be utilized as spatial encodings, thus reducing the number of excitations needed by a factor of 40. Therefore, the critical part of sequence design is how to efficiently and simultaneously encode both spatial and temporal information but avoid inducing additional artifacts. Over decades of development, there have been many special sampling trajectories proposed for fast MRSI acquisition, including echo planar spectroscopic imaging (EPSI) trajectory, spiral trajectory, concentric ring trajectory, radial trajectory, and rosette trajectory [76], as illustrated in Figure 2.4. These trajectories have different acquisition efficiency, different requirements on gradient coil systems, and result in different characteristics of collected signals.

EPSI is one of the most commonly used fast MRSI trajectories, using a sequence of alternating trapezoidal gradients to encode kx-t space [20]. As shown in Figure 2.4(a), EPSI encodes one kx line and its corresponding temporal signals in each TR, then encodes ky and kz using different TRs with different phase encoding gradients. So, the overall acceleration factor compared with CSI is equal to the number of encodings in kx. Compared with other fast trajectories, EPSI has the advantage of cartesian sampling, thus easiness in reconstruction, but it faces spectral ghost artifacts given the inconsistency between odd and even echoes. Spiral trajectory samples both kx and ky at the same time, and it has been shown in principle to have the best efficiency in covering spatial encodings for MRI [21]. But for MRSI, the efficiency of spiral trajectory is reduced by the time needed to fly back to origin for the next repeated temporal sampling. Some methods like spiral-in-spiral-out type of acquisition have been proposed, but they also face the inconsistency issue similar to EPSI. Additionally, spiral trajectory is sensitive to field inhomogeneity and requires non-cartesian reconstruction. Concentric ring trajectory also simultaneously encodes both kx and ky and has good acquisition efficiency. Compared with spiral trajectory, concentric ring trajectory does not have dead time between repeating temporal encodings. But due to the gradient limitation, the k-space rings with large radius would require multiple temporal interleaves to fulfill Nyquist sampling rate in temporal direction [77]. Rosette trajectory is another similar non-cartesian trajectory, and its advantage lies in the design flexibility and low-gradient requirements [78]. With different setup of parameters, it can be transformed into concentric ring, spiral and radial trajectories. Radial trajectory is similar to the projection-based sampling as used in CT [79]. Its advantage is the repeated sampling of k-space center, thus offering the possibility of self-

navigation. These trajectories have all been adopted in MRSI studies for accelerated acquisition, and the choice between them depends on the gradient system, practical needs, and corresponding processing methods.

2.3.2 (k, t)-space under-sampling

Another major type of acceleration approach for MRSI is under-sampling of (k, t)-space. These methods sparsely sample (k, t)-space data to reduce the number of excitations, thus reducing the acquisition time. Then the missing measurements are recovered by reconstruction methods including other prior information or constraints.

One widely used strategy to recover under-sampled data is parallel imaging, using the sensitivity encodings provided by the modern multi-channel array coils. From the mathematical standpoint, Papoulis' multi-channel sampling theorem shows that with multiple sampling channels, the signals sampled without satisfying the Nyquist rate can still be recovered under some conditions [80]. More specifically, assuming a signal $s(t)$ is bandlimited ($|f| < B/2$) and energy limited, the Shannon sampling theorem states that $s(t)$ can only be determined from the samples when the sampling interval is smaller than $1/B$. This sampling interval is known as the Nyquist sampling interval. Under multi-channel sampling scenario, assuming the sampled signals are outputs of $s(t)$ after L linear time-invariant filters, with the sampling rates as $1/L$ of the Nyquist rate, denoted as $s_l(m\Delta t), \Delta t = L/B$, Papoulis' sampling theorem states that $s(t)$ can be perfectly recovered from $s_l(m\Delta t)$ by a uniquely determined interpolation, with some conditions on the frequency responses of these filters/channels. In MR imaging, the image function can be regarded as the bandlimited signal $s(x)$ and its corresponding signal in k-space as $s(k)$, the multiple receiving coils (assuming the number of coils is L) with different sensitivity profiles can be regarded as those linear time-invariant filters. Based on the Papoulis' sampling theorem, the image function $s(x)$ can be perfectly reconstructed from the measured multi-coil data $s_l(m\Delta k)$, even if Δk is only L times of the Nyquist rate ($\Delta k = L/B$, B stands for the FOV of the image function). Even through the practical situation cannot match the idealness; for example, the real coil sensitivity profiles do not fully satisfy the requirements of this theorem on the channel frequency responses; it has still been shown that good reconstruction of MR images can be achieved with multi-channel coils under some level of sub-sampling which is lower than a factor of L [23], [24].

There have been many parallel imaging methods building on this principle to enable reconstruction from sub-sampling. The two most popular methods are known as SENSE and GRAPPA [23], [24]. Even both methods have Papoulis' sampling theorem as the most basic principle, and they share some common features, but do have different assumptions, different requirements, and different implementations. SENSE method assumes that the image data acquired by each coil channel is the image function multiplied by the receiving sensitivity profile of that channel, as shown in the following forward model:

$$d_c(\boldsymbol{k}) = \int_V \rho(\boldsymbol{r}) s_c(\boldsymbol{r}) e^{-i2\pi \boldsymbol{k}\cdot\boldsymbol{r}} d\boldsymbol{r} \tag{2.14}$$

where $d_c(\boldsymbol{k})$ is the measured k-space data of the cth coil, $s_c(\boldsymbol{r})$ is the sensitivity profile of the cth coil, and $\rho(\boldsymbol{r})$ is the image function to be reconstructed. As can be seen, to reconstruct $\rho(\boldsymbol{r})$ from $d_c(\boldsymbol{k})$, the sensitivity functions of each coil $s_c(\boldsymbol{r})$ is required to be known. In practice, one set of auxiliary data is usually acquired to pre-estimate the sensitivity maps, and the inverse problem of the forward model in Equation (2.14) can be solved in either k-space domain or spatial domain. GRAPPA method assumes the following k-space interpolation model which means that the data in one k-space location can be presented by a linear combination of adjacent k-space data from multiple channels, and the coefficients are k-space independent:

$$d_c(k) = \sum_{n=1}^{N} \sum_{m=-M/2}^{M/2} d_n(k - m\Delta k) g_{n,c}(m\Delta k) \tag{2.15}$$

where g is the interpolation kernel, M is the neighborhood range, N is the number of channels. GRAPPA method does not need to pre-acquire explicit sensitivity maps, but it needs a set of fully sampled k-space calibration data to estimate the interpolation kernel. The interpolation kernel can be estimated by solving $g_{n,c}(m\Delta k)$ from the inverse problem of Equation (2.15) in least square sense using the calibration data. Both methods have been successfully and widely used in many MR imaging techniques and they have also been adopted in MRSI methods for acceleration.

Another popular strategy is constrained reconstruction exploiting various prior information like spatial smoothness, spatial/spectral sparsity, low rankness, etc. [25], [33], [81]. These constraints and priors can significantly narrow the solution space in the reconstruction problems, and different methods can work in different applications, depending on the signal properties. The

spatial smoothness assumes that the spatial distribution of MR signals is relatively smooth especially in the human brain except at some anatomical edges; the spatial/spectral sparsity assumes the signals have only a limited number of non-zero values under some sparsify transforms; the low rankness means some specific forms of matrix have only a very small rank. All these prior knowledges can be incorporated into the reconstruction process in various forms (separately or jointly) to help recover sparse measurements. A systematic and comprehensive review of constrained reconstruction methods can be found in [82].

2.4 Partial Separability Model

MRSI is a high-dimensional imaging technique. Compared with conventional anatomical MRI, MRSI adds one or two spectral dimensions to the imaging problem (thus is a 4D or 5D imaging problem). Due to the curse of dimensionality, MRSI requires a much larger number of encodings compared with 3D MRI under traditional Fourier imaging framework. In practice, collecting MRSI encodings in good resolution require numbers on the order of a hundred in each direction and a few averages are usually needed for good SNR. So a total-number about hundreds of millions of encodings are needed, which could lead to prohibitory acquisition times. Fortunately, based on the partial separability model [33], it can verified that the high dimensional spatiospectral function actually resides in a very low dimensional subspace and only has a small number of degrees-of-freedom. It means that only a small number of measurements are needed to represent the high dimensional data, which admits highly sparse sampling of the data space. This session will introduce the mathematical framework of the subspace modeling based on the partial separability of spatiotemporal signals.

Consider the acquired spatiotemporal MRSI data $s(\boldsymbol{k}, t)$ (the data has been digitalized in the process of MR signals collection), which is defined over $\mathcal{K} \times \mathcal{T}$, with $\mathcal{K} = \{k_1, k_2, \dots, k_m\}$ and $\mathcal{T} = \{t_1, t_2, \dots, t_n\}$ (m is the number of k-space sampling points and n is the number of temporal sampling points). For now, let's assume $m > n$, which is the case in most 3D MRSI applications. In Fourier imaging framework, the number of encodings needed to represent this spatiotemporal function is $m \times n$. However, if it is assumed that the spatial variations are separable from temporal variations, which means the spatiotemporal function is partially separable, then the spatiotemporal function $s(\boldsymbol{k}, t)$ can be represented as:

$$s(\boldsymbol{k}, t) = \sum_{l=1}^{L} u_l(\boldsymbol{k}) v_l(t) \tag{2.16}$$

where L is the model order, $\{v_l(t)\}$ usually denote the temporal basis functions and $\{u_l(\boldsymbol{k})\}$ the spatial coefficients. Such a $s(\boldsymbol{k}, t)$ satisfying Equation (2.16) is called L th-order partially separable. It can be justified that when L is large enough, Equation (2.16) is a valid model to represent any L^2 functions defined over $\mathcal{K} \times \mathcal{T}$, as the following theorem states:

Theorem 2.1. Let $\mathbf{X} \times \mathbf{Y}$ be the Cartesian product of measure spaces **X** and **Y**, then the set of functions $\sum_l g_l(x) h_l(y)$ for all $g_l(x) \in L^2(x)$ and $h_l \in L^2(y)$ is a dense subset in $L^2(\mathbf{X} \times \mathbf{Y})$.

In the scenario of MRSI data, this theorem states that if $u_l(\boldsymbol{k})$ and $v_l(t)$ are L^2 functions, which is the case in practice, any L^2 function $s(\boldsymbol{k}, t)$ defined on the (k, t)-space can be expressed as the form of $\sum_{l=1}^{L} u_l(\boldsymbol{k}) v_l(t)$, as long as the order L is large enough. For better understanding, one extreme case is that when $s(\boldsymbol{k}, t)$ is digitalized, if L is chosen as $m \times n$ with $u_l(\boldsymbol{k})$ and $v_l(t)$ as delta functions, then Equation (2.16) can naturally represent any finite functions defined over $\mathcal{K} \times \mathcal{T}$, which means there are no correlations between spatial and temporal variations. But in practice, the spatial variations of MRSI signals are strongly correlated with its temporal variations. Given the spatiotemporal correction, the model order can be very small. Another extreme case is that if the temporal variations of all the spatial points are the same, i.e., $s(\boldsymbol{k}, t) = u(\boldsymbol{k}) v(t)$, then the model order is only one. The assumption on small model order of MRSI signals can also be justified by the fact that there are only a limited number of molecules or biological tissues in the brain.

The function satisfying Equation (2.16) also implies low rankness of the Casorati matrix formed by $s(\boldsymbol{k}, t)$, which means, it can be proved that the matrix

$$\boldsymbol{C} = \begin{bmatrix} s(k_1, t_1) & s(k_1, t_2) & \dots & s(k_1, t_n) \\ s(k_2, t_1) & s(k_2, t_2) & \dots & s(k_2, t_n) \\ \vdots & \vdots & \ddots & \vdots \\ s(k_m, t_1) & s(k_m, t_2) & \dots & s(k_m, t_n) \end{bmatrix} \tag{2.17}$$

has a rank upper-bounded by L and $L < \min\{m, n\}$. This is a necessary and sufficient condition for Equation (2.16). Given this partial separability model (when the model order L is small), the overall degrees-of-freedom reduces from $m \times n$ to $(m + n) \times L$, which indicates that the actual

number of measurements required to estimate the desired spatiotemporal function can be significantly decreased. Moreover, in applications like MRSI where the temporal basis functions $\{v_l(t)\}$ can be pre-determined by prior information, the number of unknown to be determined will further reduce. With this benefit, the partial separability (or low-rank, or subspace) model provides a lot of flexibility for special signal acquisition and processing methods beyond the basic Fourier imaging framework, like reconstruction from sparse sampling and signal denoising. This model has also been successfully applied in a range of MR imaging applications besides MRSI, such as dynamic imaging, function imaging, and parameter mapping [83]–[86]. This thesis research is also built on this partial separability model for acquisition design, signal processing, and image reconstruction.

2.5 Subspace-Based MRSI Method – SPICE

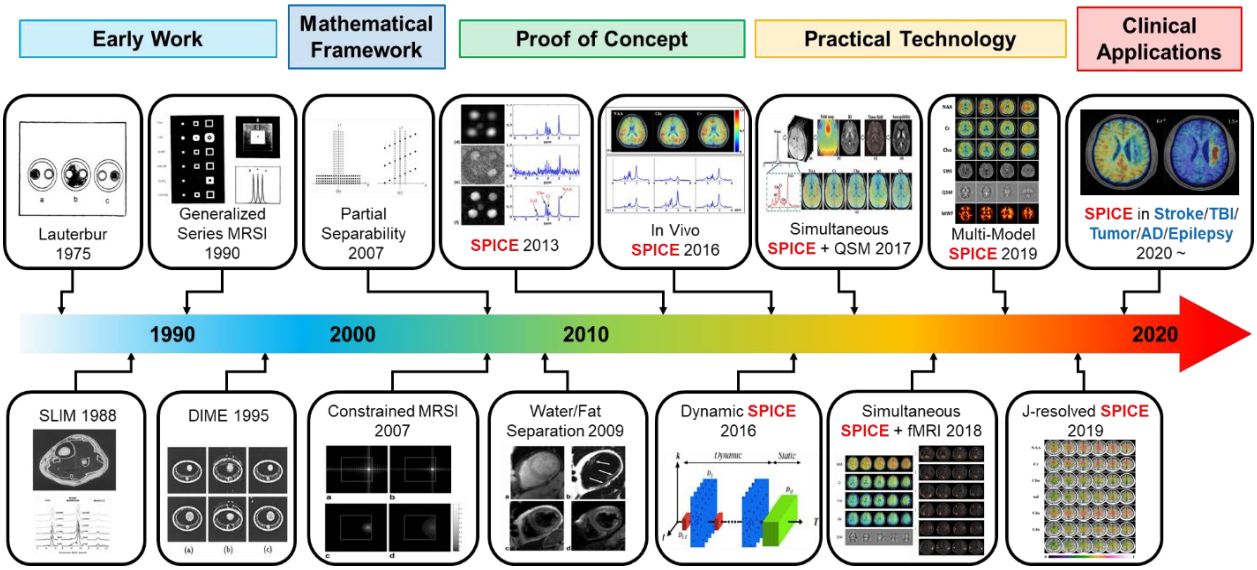

Figure 2.5: An overview on the development timeline of SPICE technique, including early works starting from 1975, mathematical framework proposed in 2007, proof-of-concept work from 2013, and recent development into a practical technique and clinical applications.

As described in the last section, the partial separability, or subspace model can be applied to MRSI methods for many aspects of improvements, including acceleration and denoising. SPICE (SPectroscopic Imaging by exploiting spatiospectral CorrElation) is such a subspace-based imaging method for high-resolution MRSI. The development of SPICE is a long-term effort, with early concepts starting from Lauterbur's work in the 1970s [11]. Then from the 1980s to 1990s,

several early works such as the compartmentalized spectroscopy like SLIM (spectral localization by imaging) and generalized-series model-based MRSI method were proposed [85], [87]. The mathematical framework, which is the partial separability model as described above, was proposed in 2007 [33]. During the same period, a few more signal processing tools like anatomical constrained reconstruction and methods for water-fat separation were also developed [81], [88]. From 2013 to 2016, the concept of SPICE had been proven feasible in both phantom and *in vivo* experiments using phototype acquisition methods, and the results have shown great potential of SPICE in advancing imaging capabilities of MRSI [34]–[36]. In recent years, SPICE has been further developed into a more powerful and practical technique for fast high-resolution metabolic imaging, with several novel designs and improvements, which is also where this thesis research contributes [89]–[92]. Moreover, the SPICE method has lately been applied to a range of clinical applications like brain tumors and stroke and achieved many encouraging results [93], [94]. These clinical cases have shown the tremendous potential and values of SPICE in clinical environments. A timeline overview of the development of SPICE is shown in Figure 2.5, summarizing some key milestones in the process. The rest of this section will briefly introduce the basic concepts of SPICE method regrading to data acquisition and data processing as proposed in the early proof-of-concept stage, which is referred as "basic SPICE".

The basic SPICE method is featured by the use of subspace model in both data acquisition and data processing. In data acquisition, the basic SPICE method uses a hybrid acquisition sequence to collect two sets of MRSI data, which are used for determining subspace structure and image reconstruction, separately. In data processing, SPICE estimates spectral subspace from one of the two datasets and reconstructs spatiospectral functions using the other one incorporating subspace structure and spatial constrains. As a result, the basic SPICE method is able to achieve 3D MRSI at around 3 mm resolution in about 30 minutes.

More specifically, in the basic SPICE method, a dual-density, dual-speed EPSI sequence is used for data acquisition, as shown in Figure 2.6. The entire data acquisition is divided into two phases. In the first phase, a slow EPSI sequence is used to acquire the data for subspace estimation, which are denoted as D_1. This slow EPSI sequence encodes two phase encoding directions and one temporal direction with sampling rates satisfying Nyquist rates. As shown in Figure 2.6(b), this acquisition only covers a small set of k-space center, thus only has a very low resolution with a short scan time. In the second phase, a rapid EPSI sequence is used to acquire the imaging data

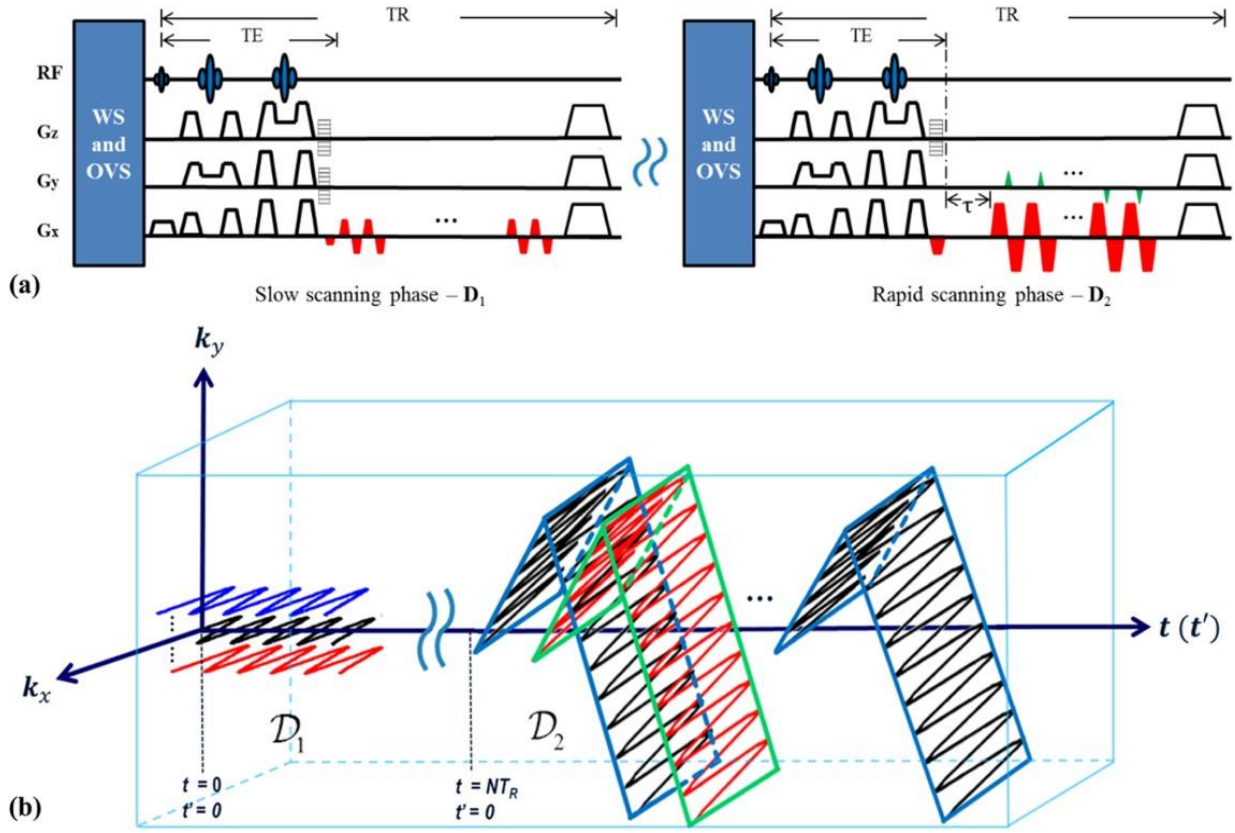

Figure 2.6: The basic SPICE sequence for 3D MRSI: (a) the dual-density, dual-speed EPSI sequence to acquire D_1 and D_2 data; (b) the corresponding (k, t)-space trajectories. This figure is from [35].

for reconstruction, which is denoted as D_2. Within each excitation, this rapid EPSI sequence simultaneously encodes two spatial dimensions as well as the temporal dimension. The third spatial dimension is encoded using different excitations/TRs with different phase encoding gradients. Additional temporal encodings are obtained using different excitations with different echo shifts. As shown in Figure 2.6(b), this D_2 acquisition has a much larger k-space coverage than D_1 to provide higher spatial resolution, but with sparser temporal samplings. As discussed in section 2.3.1, EPSI trajectories simultaneously sample spatial encodings and temporal encodings, so there is a trade-off between the number of readout points and echo-spacing, which correspond to spatial resolution in readout direction and spectral bandwidth, respectively. In these two datasets, D_1 has a smaller spatial resolution but higher spectral bandwidth, while D_2 has a higher spatial resolution and smaller spectral bandwidth, which is to be overcome via echo shifts and subspace-based processing. In both D_1 and D_2 acquisitions, the sequences use PRESS (Point Resolved Spectroscopy) for excitation and localization, which is able to selectively excite a spatial

region like brain only. If no spatial selection is needed, the PRESS excitation module can be replaced by a typical spin echo (SE) module. For water and lipid suppression, a WET (water suppression enhanced through T1 effects) module and an OVS (outer volume suppression) module are added at the beginning of each TR. A spoiler gradient is placed at the end of each TR to dephase the remaining transversal magnetization.

One example implementation of this acquisition sequence has the following scan parameters: FOV = 240×240×72 mm^3 (excitation volume = 240×240×60 mm^3), TR = 1100 ms, TE = 20 ms, readout bandwidth = 68kHz/125 kHz (for D_1/D_2), matrix size = 16×16×16×512/80×80×20×120 (for D_1/D_2, corresponding spatial resolutions = 15×15×4.5 mm^3/3.0×3.0×3.6 mm^3), total time is 26 minutes.

Given the acquired D_1 and D_2 data, the main processing steps include subspace estimation and image reconstruction. To estimate the subspace structure (basis functions) from D_1, based on Equation (2.16), it is straightforward to use singular value decomposition (SVD) directly on the Casorati matrix as shown in Equation (2.17). But the pre-requirement is that the field inhomogeneity effects need to be removed first. Otherwise, the model order would be significantly increased. The limited resolution of D_1 data makes the removal of field inhomogeneity challenging. To overcome this issue, a constrained reconstruction method incorporating a pre-acquired field map is used, as solving the following optimization problem:

$$\hat{\rho}_1 = \arg\min_{\rho} \left\| d_1 - \Omega_1\left(\mathcal{F}(B \odot \rho)\right) \right\|_2^2 + \lambda_1 \|\rho\|_*, \tag{2.18}$$

where ρ is the field-corrected spatiotemporal MRSI signal, d_1 the measured (k, t)-space D_1 data, λ_1 the regularization weight, and Ω_1, $\mathcal{F}$, B the operators representing k-space sampling, Fourier transform, and field inhomogeneity effects, respectively. After $\hat{\rho}_1$ is obtained, it can be used to reformed the Casorati matrix as Equation (2.17) and then be applied by SVD. The first L right singular vectors are chosen to form the temporal basis functions (denoted as a matrix V). With the determined basis functions from D_1, the image reconstruction problem becomes estimation of spatial coefficients in Equation (2.16) using the D_2 data. It can be done by solving the following regularized least-squares formulation:

$$\hat{\mathrm{U}}_2 = \arg\min_{\mathrm{U}} \left\| d_2 - \Omega_2\left(\mathcal{F}(B \odot (\mathrm{UV}))\right) \right\|_2^2 + \lambda_2 \|\mathrm{W}\nabla\mathrm{U}\|_2^2, \tag{2.19}$$

where U is the matrix form of spatial coefficients $\{u_l(x)\}$, d_2 the measured (k, t)-space D_2 data, λ_2 the regularization weight, and W∇ the edge weighted total variation operator. The later term, a weighted L_2 regularization incorporates spatial priors to further improve the reconstruction. The spatial prior can be generated from any anatomical images. This form of regularization has good computational efficiency and is easy for characterization. With the spatial coefficients determined, the reconstructed spatiotemporal functions can be generated using U and V as Equation (2.16).

Using the basic SPICE method, many encouraging preliminary results have been obtained, showing a good combination of resolution, imaging speed, and resulting SNR [34]–[36]. However, the scan time around 30 minutes is still not good enough to be clinically welcomed as a routine imaging method. Besides, additional scans are needed to acquired field map and anatomical images for data processing, which also take more scan time.

2.6 Ultrahigh Field MR

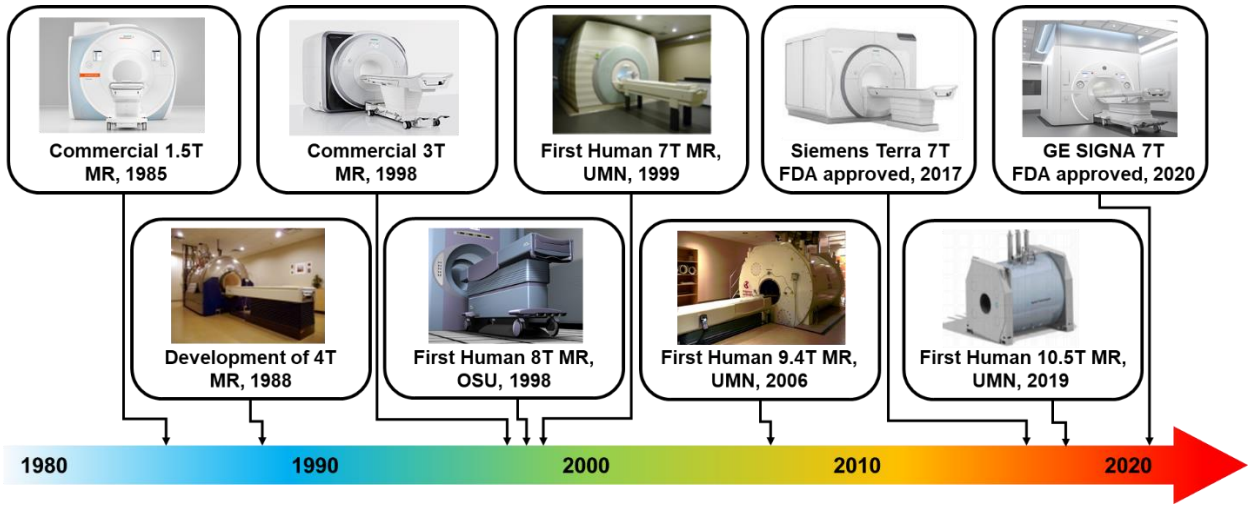

Figure 2.7: The timeline of development on the high field MR (1.5T - 7T) and ultrahigh field MR (≥7T).

Normally, ultrahigh field MR is referred to as MR system with a field strength equal to or larger than 7 Tesla. The first 7T human MR system was established in 1999. Over the last 20 years, we have witnessed encouraging progress in the instrumentation improvement and overcoming technical challenges in ultrahigh field MR [37], [38]. In recent years, the ultrahigh field MR has received tremendous interest in both scientific research and clinical studies, especially after the manufacture 7T systems got Food and Drug Administration (FDA) approval. Both Siemens

Magnetom 7T Terra and GE SIGNA 7T have been approved for clinical use by the US FDA in 2017 and 2020, respectively. To date there have been more than 80 operative human ultrahigh field MR scanners around the world and the number continues increasing. A timeline of the development of MR with different field strength is summarized in Figure 2.7.

Compared with low field MR (< 1.5T) and high field MR (1.5T - 7T), ultrahigh field MR has several attractive advantages including enhancement of SNR and contrast-to-noise ratio (CNR) which enables higher spatial resolution; change of relaxation times (such as prolonged T_1 and shortened T_2) which leads to better imaging contrast in some specific imaging applications; and increased chemical shift dispersion especially benefitting separation of molecules in MR spectroscopy/spectroscopic imaging.

- SNR: The most direct benefit of ultrahigh field is the increase of SNR. Given the relationship between thermal equilibrium spin polarization and field strength shown in Equation (2.3), ultrahigh field MR can provide a linear increase of signal intensity theoretically. In practice, the enhancement of SNR also depends on the coil setup, B_1 transmission field, shape of the object, and effects of displacement currents. Based on the simulation study considering those practical factors, the SNR gain at 7T is still in the linear regime, approximately [95]. Therefore, compared with the widely used 3T MR system, 7T MR can provide more than twice SNR in general. This SNR improvement has been largely used to push higher spatial resolution, as demonstrated in a variety of MR imaging techniques, such as anatomical MRI, fMRI and MRSI.
- Relaxation times: Relaxation times of molecules change with field strength. Generally, as field strength increases, T_1 values increase significantly, T_2 values decrease slightly, while T_2* values decrease almost linearly. Taking the water of gray matter as an example, from 3T to 7T, T_1 value increases from around 900 ms to 1800 ms, T_2 value slightly decreases from 80 to 65 ms, and T_2* value decreases from around 64 ms to only 35 ms. These changes of relaxation times can provide better imaging contrast in some imaging techniques. For example, due to the decrease of T_2* value (which is the result of increased susceptibility effects), ultrahigh field MR has shown improved imaging of brain vascular structures using susceptibility weighted imaging.
- Chemical shift dispersion: Based on Equation (2.9), the chemical shift dispersion increases linearly with field strength, which provides better frequency separation between different

molecules. Especially for ^{1}H-MRSI, the spectra are quite crowded with the frequencies of more than ten molecules spreading within a range of 4 ppm. With increased chemical shift dispersion, it would be easier to overcome some of the challenging issues in MRSI, such as removal of water and lipid signals from metabolite signals and accurate robust spectral quantification.

However, there is still a considerable number of technical challenges restricting the impact of ultrahigh field MR in practical use. These technical issues include more inhomogeneous B_0 main field and B_1 transmission field, quadratically increased specific absorption rate (SAR), and faster signal decay (due to shortened T_2*) at ultrahigh field.

- B_0 inhomogeneity: The susceptibility effect is linearly dependent on the field strength, so the B_0 field inhomogeneity greatly increases at ultrahigh field. The increased B_0 inhomogeneity could lead to severe artifacts and signal distortion, especially in the regions with large susceptibility effects like the frontal areas near the sinuses. For some imaging techniques like echo-planar imaging (EPI) sensitive to B_0 field inhomogeneity, ultrahigh field would cause significantly increased artifacts or geometric distortions.
- B_1 inhomogeneity: The relationship between wavelength and frequency is $\lambda = v/f$. So with an increased field strength (thus resonance frequency), the wavelength of the RF pulse decreases significantly at ultrahigh field. More specifically, for excitation of ^{1}H at its resonance frequency, the RF pulse wavelength is around 25 cm at 3T while it becomes around 12 cm at 7T, smaller than the normal human head size. Therefore, the interference effects can cause severe excitation variations over the imaging volume, which could lead to noticeable spatial inhomogeneity on images. This inhomogeneity sometimes is difficult to be separated with real image contrast, thus it causes challenges in both qualitative and quantitative evaluation.
- SAR: A simplified model of SAR calculation is $SAR = (\sigma A^2 \omega^2 B_1^2 D)/2\rho$, where σ is the electrical conductivity of tissue, A the body size, ω the RF frequency, B_1 the RF pulse amplitude, and D the duty cycle. Therefore, given the same subject and the same RF pulse, SAR at 7T is more than 4 times than that at 3T. The increased SAR limits the usage of quite some sequences with high SAR values, such as turbo spin echo (TSE), inversion recovery (IR), adiabatic pulses and sequences with very short TR like fast low angle shot (FLASH).
- Signal decay: As described above, T_2* value decreases almost linearly with field strength increasing. The significantly faster signal decay means shorter acquisition window, degraded

SNR in late echoes, wider spectral linewidth for spectroscopic signals, and more serious signal dephasing and distortion. For acquisition sequences with a long TE, the SNR improvement brought by the increased field strength may be cancelled by the faster signal decay.

In the past decades, many works and efforts have been made to overcome these technical challenges [96], [97]. Even though they have not been fully addressed, but given the significant amount of technical advances, some quite encouraging results have been achieved at 7T regarding better reveal of morphological details as well as improved imaging capability. For example, anatomical images at submillimeter resolution have been shown in a clinically feasible scan time [43]–[45], functional imaging with improved spatial accuracy and neural activity specificity has been demonstrated [41], [42], and some works have shown the improved resolution and robustness of metabolic imaging at ultrahigh field [47]–[49]. These results have shown the unique opportunities provided by ultrahigh field in improving imaging performance. This thesis research implements the SPICE method at ultrahigh field and utilizes its SNR benefits to further enhance the imaging capability for high-resolution metabolic imaging.

CHAPTER 3 – DATA ACQUISITION FOR HIGH-RESOLUTION ^{1}H-MRSI AT 3T

In this chapter, we present a novel data acquisition scheme for fast high-resolution ^{1}H-MRSI at 3T, further extending based on the basic SPICE method. This data acquisition sequence is characterized by several unique features to increase imaging efficiency and to make SPICE a feasible technique for practical applications and clinical environments.

3.1 Pulse Sequence

As described in section 2.5, the basic SPICE sequence has produced very promising results as a proof-of-concept imaging tool. Aiming at being a clinically endorsed imaging technique, further improvements are needed in terms of imaging speed, SNR, and robustness. Figure 3.1 shows the sequence diagram of the proposed pulse acquisition scheme, equipped with several unique features to improve imaging capability in these aspects. These acquisition features include: (1) FID-based acquisition with ultrashort TE, (2) short TR, (3) no water/lipid suppression, (4) EPSI trajectories with a large echo-space, (5) blipped gradients for sparse sampling, and (6) motion navigators. This section will introduce these acquisitions features and their impacts on the imaging performance in detail.

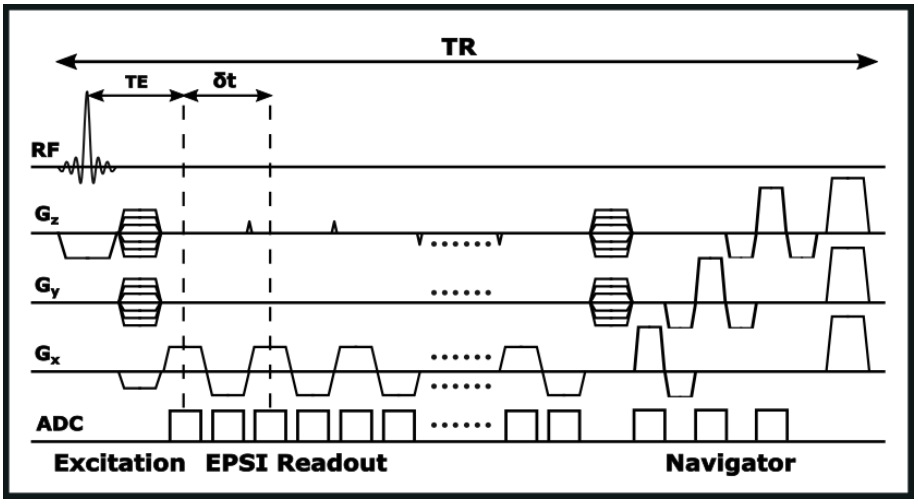

Figure 3.1: Pulse sequence diagram of the proposed data acquisition scheme. This sequence includes several unique features to enable fast high-resolution MRSI, which include: FID-based acquisition with ultrashort TE, short TR; no water/lipid suppression; EPSI trajectories with a large echo-space; embedded motion navigator for motion detection; and blipped gradients used for sparse sampling of (k, t)-space.

3.1.1 FID-based acquisition with ultrashort TE

Typical MRSI methods use a spin echo or stimulation echo-based sequence for excitation and localization, such as PRESS, STEAM (stimulated echo acquisition mode), LASER (localization by adiabatic selective refocusing), and semi-LASER methods [14], [16]. These SE type of MRSI methods have several advantages including high-quality volume selection and good spectral quality. FID-based acquisition without any 180-degree refocusing pulses is another type of MRSI scheme which is typically used in ^{31}P-MRSI and ^{13}C-MRSI, given their very short T_2 values. The comparison of FID-based MRSI and SE-based MRSI is discussed as follows.

- Volume selection: PRESS, STEAM, LASER, and semi-LASER can specifically excite a spatial volume (with selective excitations in three dimensions) while basic SE sequences and FID sequences can only excite a slab (with selective excitation in only one dimension, usually in the slice dimension). Volume selection can help exclude signals from unwanted regions like the subcutaneous layer, but it may also exclude signals from some regions of interest like cortex near the edge of the brain. So, SE sequences and FID sequences can reverse full signals from in-plane, but they need to overcome the lipid contamination issue in other ways.
- Chemical shift displacement (CSD): Different molecules have different chemical shifts, thus different resonance frequencies, so they would experience different excitation profiles given the same selective excitation, normally called CSD. This CSD issue is particularly problematic in single voxel spectroscopy (SVS) if using PRESS or STEAM. LASER and semi-LASER use adiabatic pulses, thus minimizing the CSD. SE sequences and FID sequences only have selective pulses in one dimension, so the effects of CSD can be minimized by wide bandwidth pulses or some oversampling.
- TE: SE-based acquisitions usually include one or more refocusing pulses and their associated gradients after the excitation pulse, while FID-based acquisitions can acquire signals after excitation with very small decays for phase encoding gradients. So, SE-based acquisitions usually have a relatively long TE (> 20 ms), while FID-based acquisitions can have a very short TE (< 4 ms). The benefit of long TE used in SE-based acquisitions is reduction of signals from both macromolecules and lipids, thus the metabolite signals are more clear and easier to quantify. But long TE causes a loss of SNR, and the FID-based acquisitions can minimize the signal loss due to TE and keep short T_2 components like macromolecules and lipids.

- Energy deposition and B_1 inhomogeneity: As mentioned above, SE-based acquisitions include one or more 180-degree refocusing pulses while FID-based acquisitions only use one excitation pulse with relatively a small flip angle. So the energy deposition or SAR of FID-based sequences are much smaller than the SE-based sequences, especially at high field or ultrahigh field systems. Similarly, the use of 180-degree pulses also makes the SE sequences relatively more sensitive to B_1 inhomogeneity compared with FID-based sequences. But it should be noted that the adiabatic pulses used in LASER and semi-LASER sequences can reduce the sensitivity to B_1 inhomogeneity.

In summary, SE-based sequences have the advantages of volume selection and clearer spectra, while FID-based acquisitions generally keep more signal components, have smaller CSD, smaller SAR, and are less sensitive to B_1 inhomogeneity. Considering these factors, SNR efficiency (which is discussed in the next section), and capability of signal processing tools, an FID-based acquisition instead of the original SE-based acquisition, is used in the proposed acquisition sequence. The TE value of this sequence is kept as short as possible to preserve the SNR which is 1.6 ms in current implementation.

3.1.2 Short TR for SNR efficiency and acquisition efficiency

Typical SE-based sequences usually use a relatively long TR more than one second, while FID-based sequences can use a very short TR as possible. Taking simple CSI as an example, if both SE sequences and FID sequences only sample temporal encodings of one specific k-space location in each TR, then their scan times are the numbers of spatial encodings multiplying their TR values. So given the same number of encodings, shorter TR means shorter scan time, thus higher acquisition efficiency. For example, in a CSI experiment with spatial encodings of 16×16×10, SE sequences with TR as 2 seconds would take 5,120 seconds, around 85 minutes, while FID sequences with TR as 200 ms only takes 8.5 minutes, which is a significant reduction. However, for MRSI, another major concern is the SNR. The SE sequences in the above example is sure to have much better SNR than the FID sequences given the long scan time. So SNR efficiency needs to be taken into account in sequence selection. Here we compare the SNR efficiencies of both FID sequences and single-echo SE sequence, changing with TR values. In both cases, perfect spoiling is assumed.

In FID-based sequence (assuming excitation using the Ernst angle), when the magnetization reaches a steady state, the signal formulation at TE can be expressed as:

$$S_{FID} = \frac{M_0 \sin\theta_E \,(1 - e^{-TR/T_1})}{(1 - \cos\theta_E \, e^{-TR/T_1})} e^{-TE/T_2^*}, \tag{3.1}$$

where θ_E is the Ernst angle, which is the flip angle that maximizes the signals in Equation (3.1). The Ernst angle can be calculated as:

$$\theta_E = \arccos(e^{-TR/T_1}). \tag{3.2}$$

In SE-based sequence (assuming the excitation pulse is 90˚ and the refocusing pulse is 180˚), the signal intensity at TE is:

$$S_{SE} = M_0(1 - 2e^{-(TR-TE/2)/T_1} + e^{-TR/T_1})e^{-TE/T_2^*}. \tag{3.3}$$

The SNR efficiency is computed as:

$$\eta = \frac{S}{\sqrt{TR}}. \tag{3.4}$$

For comparison, a T_1 value of 1400 ms, a T_2 value of 260 ms, and a T_2* value of 30 ms, are selected (representative as NAA at 3T). The TE values are selected as 4 ms and 30 ms for FID and SE sequences, respectively. Their SNR efficiencies with different TRs are plotted in Figure 3.2.

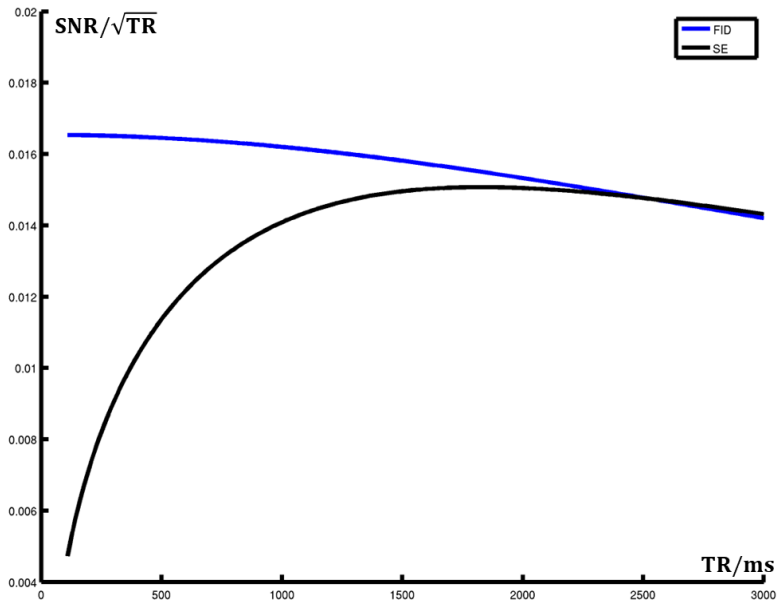

Figure 3.2: SNR efficiency comparison between FID and SE sequences, with different TR values.

We can see that in this simple setup (other factors like number of encodings, bandwidth, etc. are not included), FID sequences with a short TR have better SNR efficiency than SE sequences. Additionally, when TR is in a short range (100 ms to 300 ms), the SNR efficiency shows little difference. Therefore, based on the acquisition efficiency and SNR efficiency, the TR used in the FID sequence used in this research is as short as 160 ms.

3.1.3 Elimination of water/lipid suppression

The signal intensity of water and lipid signals are usually several orders of magnitude higher than that of metabolite signals in the brain, so water and lipid suppression are almost necessary in the traditional MRSI methods. The water signals and metabolite signals have different resonance frequencies, so typically frequency selective pulses are used to excite and then spoil the water signals, such as CHESS (chemical shift selective), WET, and VAPOR (variable pulse power and optimized relaxation delays). The basic SPICE sequence uses a three-pulse WET for water suppression. The lipid signals are mainly from the subcutaneous layer, leaking into the brain due to the limited spatial encodings. One method to suppress the lipid signals are using spatial selective pulses like OVS to excite and spoil the signals in the subcutaneous layer, as described in the basic SPICE acquisition sequence. Another method is to use inversion recovery pulses to null the lipid signals by selecting specific inversion times. However, all these suppression methods will prolong the TR, thus total scan time since multiple pulses and gradients are needed to be added prior to excitation. Moreover, methods like inversion recovery also affect the signals of metabolites. Therefore, in the proposed acquisition sequence, no water suppression and lipid suppression pulses are used, the removal of water and lipid signals is performed using signal processing methods instead.

Elimination of these suppression pulses have several advantages. First, without these pulses, TR values can be pushed much shorter, as the 160 ms used. So, the acquisition efficiency is further improved. Second, removing of these pulses can significantly reduce the energy deposition, which is especially useful at high field and ultrahigh field given the short TR. Third, it can keep the metabolite signals unaffected from the suppression pulses like OVS or inversion recovery. Fourth, the unsuppressed water signals can be utilized to provide a lot of useful information such as structural information, sensitivity map, field map, etc. This information from the water signals can be used to facilitate reconstruction, correct system imperfection, and provide water imaging of multiple modalities.

3.1.4 EPSI trajectories with a large echo-space

As introduced in section 2.5, SPICE uses EPSI trajectories to provide fast simultaneous spatial and temporal encodings. The echo-space of the EPSI trajectory is determined by:

$$\tau_{EPSI} = 2 \times (2 \times \tau_{ramp} + N_{read} \times t_{read}), \quad (3.5)$$

where τ_{ramp} is the ramp time of readout gradient, t_{read} the readout dwell time, which is determined by the readout bandwidth, and N_{read} the number of readout points, which determines the spatial resolution in readout direction. In traditional EPSI methods, the echo-space is limited by the spectral bandwidth, thus the number of readout points and the readout spatial resolution are very limited. Enabled by the subspace modeling, the echo-space of SPICE sequence do not necessarily satisfy the Nyquist sampling rate, so a large echo-space can be used to achieve high readout resolution, as illustrated in Figure 3.3. More specifically, in the proposed sequence, the number of readout points is 110, plus ramp sampling points of 24 (the effective total number of readout points is 126), resulting an echo-space of 1.76 ms (equivalent to 568.2 Hz). With an FOV of 240 mm in readout direction, the readout resolution is around 2.0 mm, which is significantly higher than the typical EPSI methods.

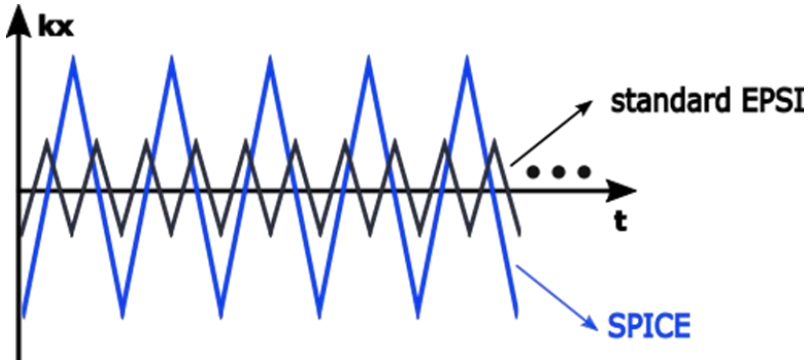

Figure 3.3: Comparison of EPSI trajectories in (kx, t)-space of traditional EPSI method and SPICE method.

The basic SPICE method acquires two sets of data, with D_1 for subspace estimation and D_2 for image reconstruction. In the proposed sequence, D_1 acquisition is no longer needed since the subspace structures can be estimated and learned from a set of training data. Furthermore, in acquisition of the metabolite signals, no blipped gradients are used for spatial encodings, as the typical EPSI methods. This means that only one kx line is covered in each TR, including all the temporal encodings of that kx line. Both ky and kz dimensions are encoded using different TRs

with different phase encoding gradients. Removal of the D_1 acquisition further reduces the scan time, and the modification on D_2 acquisition improves the (k, t)-space coverage, avoids the inconsistency issue between multiple echo shifts, and makes it more flexible for sparse sampling of peripheral (k, t)-space, as introduced in the next section.

3.1.5 Blipped gradients for sparse sampling

The proposed sequence does not suppress water signals, so the simultaneously acquired water signals can be used for water imaging like QSM [89]. If no extension is applied, the resolution of water signals is the same as the metabolite signals, which is around two to three mm. This resolution is high for metabolite signals but not enough for water signals to capture some fine structures in the brain. As a reference, typical structural imaging techniques used in routine clinical scans have resolutions around one mm. To increase the spatial resolution, one alternative approach is to increase the number of spatial encodings by adding more TRs with higher phase encoding gradients, but this will significantly increase the scan time. For example, to increase the resolution from three mm to one mm in two phase encoding directions, the number of TR will increase to nine times, thus the total scan time will be nine times, which is not practically acceptable. To address this issue, we use blipped gradients in the proposed sequence. As described in the basic SPICE sequence, using blipped gradients can enable multiple spatial encodings in one FID process, which is equivalent to utilizing temporal encodings for spatial encodings. More specifically, without blipped gradients, only one (ky, kz) location is encoded in one TR, but the t direction is fully sampled; with blipped gradients, multiple (ky, kz) locations can be encoded in one TR, but t direction of these points are under-sampled. Different from the original SPICE method where echo shifts are used to compensate the temporal encodings, the proposed method leaves the missing (k, t)-space data empty and uses a reconstruction method to recover the missing measurements. A uniform under-sampling is also used in the phase encoding directions, which can be recovered using typical parallel imaging techniques. With these sparse sampling strategies, the acquisition for high-resolution signals is significantly accelerated. But given the limited SNR of metabolite signals and the highly sparse measurements, this extended acquisition is only for water signals but not metabolite signals. The detailed design of (k, t)-space sampling pattern is discussed in section 3.2.

3.1.6 Linear motion navigators

As shown in Figure 3.1, a set of linear motion navigators is included at the end of each TR. The navigator set includes three readouts in the k-space center of three orthogonal directions (kx, ky, kz). With these navigators in each TR, the proposed sequence is able to detect translational motion of the subject with a temporal resolution of a TR (160 ms). More specifically, the signals acquired by each of the three navigators can be regarded as a projection of the object in the axis (x, y, z). This can be easily understood from the central slice theorem, which states that the Fourier transformation of a projection at a specific angle is equal to the line in Fourier space at the same angle. Therefore, any translational head movement in these three directions can be detected and estimated from these three projections. Since each TR has one set of such navigators, the proposed sequence can identify the TRs corrupted by head motion and the corresponding data, which provides a lot of flexibility in retrospective motion correction.

It should be noted that this design of navigators minimizes affecting on the original sequence, without prolonging TE or lengthening the scan time. There are many other more sophisticated motion navigators for MRSI which can provide more accurate motion estimation like including estimation of rotation motion [98]–[103], but most of these methods require additional equipment or additional acquisition time for collecting enough signals. Comparing with these methods, the implementation in the proposed method is relatively simple but efficient. It should also be noted that the signals at the end of the TR still have enough SNR for motion estimation, which is also one of the benefits of removing water suppression in acquisition.

In summary, the proposed pulse sequence has several unique acquisition features including: (1) FID-based acquisition with ultrashort TE, (2) short TR, (3) no water/lipid suppression, (4) EPSI trajectories with a large echo-space, (5) blipped gradients for sparse sampling, and (6) motion navigators. These acquisition features improve the pulse sequence over the basic SPICE sequence in terms of efficiency, energy deposition, resolution, and robustness. The following section will describe the design of sampling pattern in (k, t)-space for further acceleration and resolution enhancement.

3.2 Sparse Sampling of (k, t)-Space

The proposed sequence can simultaneously acquire the spectroscopic signals of water, lipid, and metabolites in (k, t)-space. So its sampling in (k, t)-space not only needs to take into account the

desired spatial resolution, spectral bandwidth, and total scan time, but most importantly, the largely different characteristics of different signals. The concentration of metabolites in human brains is several orders of magnitude lower than that of water and lipids, so the most limiting factor for metabolic imaging is its SNR. Given the limited SNR, it is challenging to push high-resolution and acceleration beyond what the SNR can support. On the contrary, signals from water and lipids have sufficient SNR, especially in spectroscopic imaging, so higher resolution and acceleration is much more feasible. Besides, the metabolite spectra contain signals from multiple molecules like NAA, Cr, Cho, Ins, Glu, etc. and these signals spread over a narrow frequency range around three ppm, so some of the metabolite signals are largely overlapped with each other, while the water signals have only a single resonance peak in ideal conditions. Therefore, typically, more temporal encodings are needed for metabolite signals to separate signals from different molecules while fewer temporal encodings are needed for water signals.

Considering these factors, the sampling pattern of the proposed sequence in (k, t)-space is designed as shown in Figure 3.4. As can be seen, this (k, t)-space is sampled in two regions with variable density. First, the central (k, t)-space region is fully sampled both spatially and temporally. It means the EPSI trajectory in one TR only samples the (kx, t)-space of one single (ky, kz) point. The (ky, kz) space in this region is covered using different TRs with different phase encoding gradients. This full sampling in this region is to preserve enough SNR and sufficient temporal encodings for metabolite signals. The peripheral (k, t)-space is highly sparsely sampled using blipped gradients, as mentioned in section 3.1.5. The ky direction is under-sampled by a factor of 3 and the (kz, t)-space is under-sampled by a factor of 12. The sampling of (kz, t)-space follows the spatiotemporal CAIPIRINHA (Controlled Aliasing in Parallel Imaging Results in Higher Acceleration) pattern [104], [105], which encodes different kz with in adjacent temporal points. More specifically, in a (kz, t)-block, assuming point (kz0, t0) is sampled at t0, then point (kz0+2Δkz, t0+Δt) will be sampled at the next temporal point (t0+Δt). When the kz encoding points hit the boundary of the (kz, t)-block, then the gradient blip step would change the polarity, becoming -2Δkz. So the sampling trajectories are in "zig-zag" shape in (kz, t)-space. If the temporal dimension is collapsed, which means all the (kz, t) points are used to fill its corresponding kz only, then there would be no under-sampling in kz direction. The CAIPIRINHA pattern has been proven to facilitate improved parallel imaging reconstruction, reducing noise and aliasing, thus it is widely employed in the sparse sampling design [104], [105]. Specially, the (kz, t)-space

CAIPIRINHA trajectories simultaneously encode both spatial and spectral information in each FID process, exploiting the spatiospectral correlation of MRSI data, thus enabling high sparsity level.

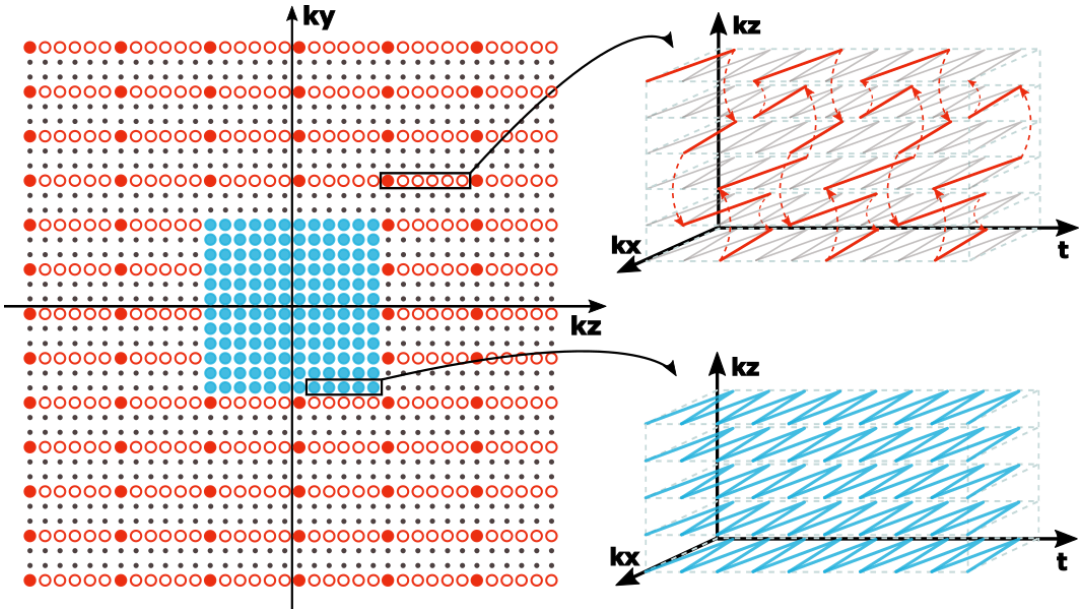

Figure 3.4: Sampling pattern of the proposed method in (k, t)-space. Entire (k, t)-space is sampled in two regions with variable density. The central region is fully sampled with typical EPSI trajectories, while the outer region is sparsely sampled both spatially (with a factor of 3 in ky) and temporally (with a factor of 12 in kz-t space) for water and lipid signals.

With this sampling pattern, metabolite signals are reconstructed only using the central region of (k, t)-space given its SNR and temporal encoding numbers. The unsuppressed water signals in this region can also be utilized to estimate the sensitivity profile of the acquisition coils and generate a B_0 field inhomogeneity map for field correction in post-processing. The water and lipid signals are reconstructed using the entire (k, t)-space, which has a large k-space coverage in ky and kz directions for higher resolution. The large acceleration factor in this outer region minimizes the additional scan time used for high-resolution. The high-resolution of water and lipid signals bring several benefits. First, the high-resolution water image and derived parameter maps like QSM can reveal more detailed brain structures like veins compared with low-resolution as the central region. This extended high-resolution can make the water imaging results comparable to typical structural imaging sequences. Second, the high-resolution of lipid signals can significantly reduce the leakage of lipid signals from the subcutaneous layers into the brain, i.e., mitigating the

lipid contamination issue. Third, the high-resolution water signals can provide a high-resolution B_0 field map which is useful to correct intra-voxel field inhomogeneity effects.

In current implementation of this sequence to cover an FOV of 240×240×72 mm^3, the entire (k, t)-space contains 124×216×72×144 encodings, which is corresponding to a nominal spatial resolution of 2.0×1.0×1.0 mm^3 for both water and lipid signals. The central k-space region contains only 124×78×24 spatial encodings, which is corresponding to a nominal spatial resolution of 2.0×3.0×3.0 mm^3 for metabolite signals. Given the current sparse sampling as described above (Ry = 3, Rzt = 12 in outer region), the overall acceleration factor is 6.9 for water and lipid signals.

3.3 Embedding Navigators

Besides the B_0/B_1 inhomogeneity, there are still a few system imperfections that can cause artifacts or degradation of data quality, such as B_0 field drift, head motion, eddy current effects between odd and even EPSI echoes. As mentioned above, the B_0/B_1 inhomogeneity can be corrected using the companion high-resolution water signals. To overcome the other system imperfections, we incorporate a few navigator-type of acquisitions in the sequence to collect additional useful information. This section describes two sets of navigator signals used in the proposed sequence in detail. One is a navigator to detect field drift and the other one is a bipolar navigator to correct eddy current effects in EPSI echo pairs.

3.3.1 Field drift navigators

In the MR scans with heavy gradient usage, such as diffusion imaging and functional imaging, the power deposition of RF pulses can warm up multiple scanner components and lead to a frequency drift of the B_0 field. Typically, the frequency drift could be from a few Hz to tens of Hz in a ten-minute scan, depending on the scanner hardware and pulse sequence. In MRSI experiments, this time-dependent frequency shift would cause violation of the assumption that the spatiotemporal functions of imaging objects keep unchanged during the scan period. So, with these gradient-induced frequency shifts, the resulting MRSI data is the integration of a time-changing imaging function, which can cause signal distortion and (k, t)-space misalignment. An accurate estimation of the frequency drift along time is needed to correct the effects. Therefore, navigator signals are embedded in the proposed acquisition sequence to track the drift frequency.

The pulse sequence diagram is shown in Figure 3.5, including two sets of acquisition, one is a short acquisition of FID signals and the other one includes multiple pairs of linear navigators. More specifically, after RF excitation, no phase encoding gradients are applied, so the FID signals are formed on the k-space center then a 10 ms window of the FID signals are collected. This set of short FID signals can be used to estimate the overall (zero-order) frequency. Following the short acquisition for field drift, a couple of paired linear navigators are added as those at the end of each TR in SPICE acquisition. These multiple pairs of linear navigators can be used to estimate high-order overall frequency. This set of navigator acquisition is embedded and repeated every 60 TRs in the SPICE acquisition. This means the navigator signals are collected every 10 seconds in the scan, so they can track the frequency changes along the time. Then the measured drift frequency values can be utilized in processing to correct the effect of field drift retrospectively.

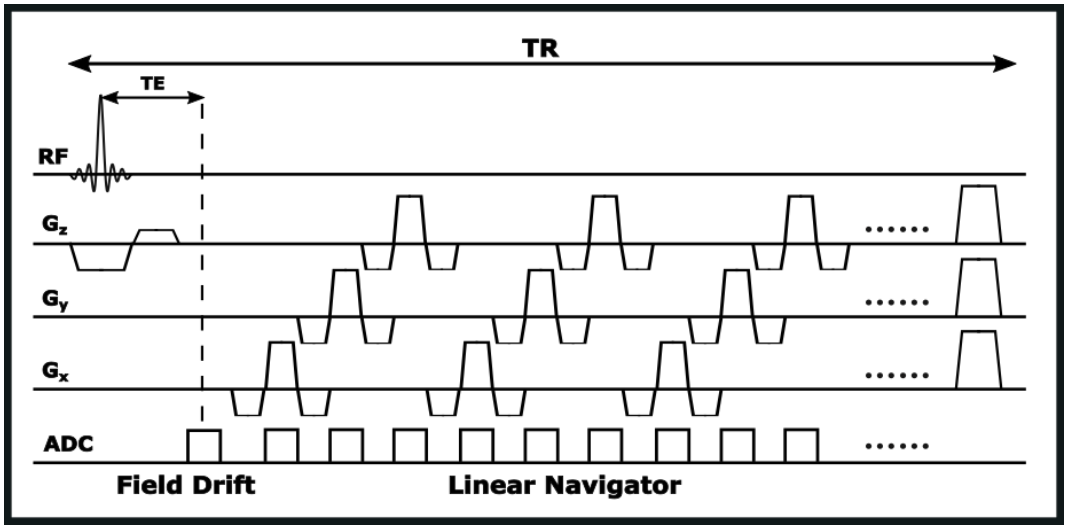

Figure 3.5: Sequence diagram for field drift acquisition. A short FID is acquired after the excitation for tracking field drift, multiple pairs of linear navigators are used for higher order field drift detection.

3.3.2 EPSI bipolar navigators

As shown in Figure 3.1, the proposed sequence uses a bipolar EPSI readout. Different from unipolar or flyback EPSI readout, which only collects data at odd echoes or even echoes and uses large gradients in the other one, bipolar EPSI trajectories use balanced gradients and collect data at both odd and even echoes. Bipolar EPSI readout collects more data given no dead time for flying back, thus has better efficiency than unipolar EPSI readout. However, as mentioned in section 2.3,

bipolar EPSI trajectories are much more sensitive to the eddy current effects, which causes observable inconsistency between the odd and even readouts. As a simplified model for understanding, eddy current is generated by gradient switch, and it causes a change on gradient amplitude, thus a change on actual gradient moment. The effect of gradient moment changes can be simplified as a shift on k-space. In bipolar EPSI trajectories, eddy currents at the beginning of both positive and negative gradients induce k-space shifts, but the shifts are in opposite directions. Therefore, the eddy current causes data inconsistency between the odd and even echoes of EPSI data. Without correction, there will be significant ghost in the resulting spectrum due to the inconsistency. As discussed above, in a simplified model, this eddy current effect can be viewed as a k-space shift and a phase offset in the readout. The k-space shift and phase offset are further assumed to be not phase encoding dependent, thus only global estimation of k-space shift and phase offset is needed for a zero-order correction.

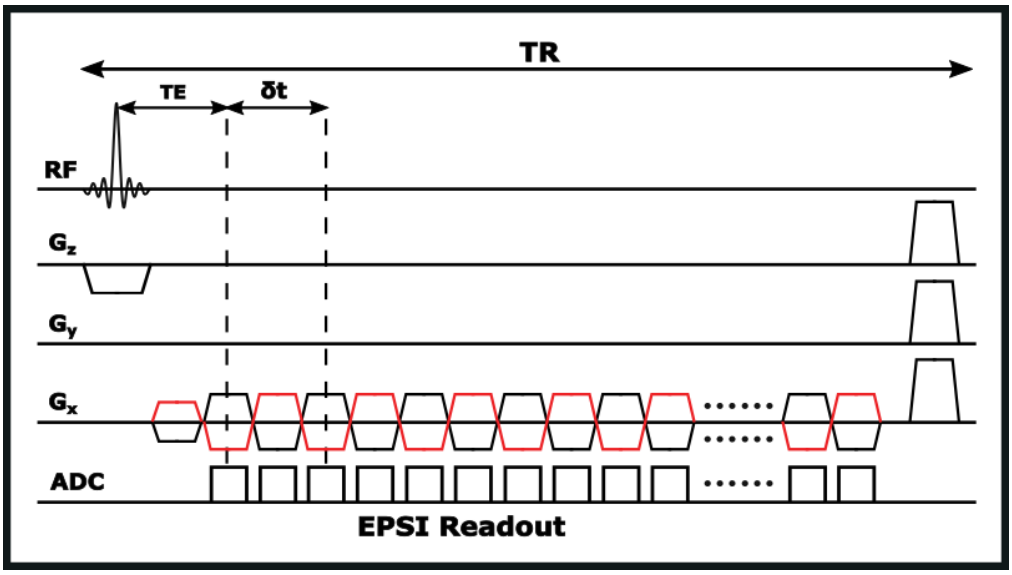

Figure 3.6: Sequence diagram for bipolar navigator acquisition. The EPSI readouts with opposite polarities are acquired in a pair of TRs at the end of the proposed sequence.

Therefore, a set of navigator signals is collected in the proposed sequence, as shown in Figure 3.6. Two TRs with EPSI trajectories are collected at the end of SPICE scan. In both TRs, no additional phase encoding gradients are applied after excitation, so the signals are formed in the (ky, kz)-center. The EPSI readouts in two TRs are of opposite polarities, so combining two TRs can form one echo chain only containing positive echoes and one only containing negative echoes. It is assumed that there is no eddy current-induced inconsistency in these two echo chains since

the eddy current causes the same effects among positive echoes or among negative echoes. Therefore, comparing the composite echo chains with acquired echo chains can estimate the global k-space shift and phase offset between positive echoes and negative echoes, and they can be used to correct the bipolar inconsistency in the MRSI data.

3.4 Implementation for Experimental Studies

In current implementation for experimental studies at 3T, the sequence parameters are summarized as follows: FOV = 240×240×72 mm^3, resolution of metabolites = 2.0×3.0×3.0 mm^3 (matrix size = 124×78×24), resolution of water and lipids = 2.0×1.0×1.0 mm^3 (matrix size = 124×216×72), TR = 160 ms, TE = 1.6 ms, echo-space = 1.76 ms, echo number = 74×2, readout bandwidth = 167 kHz, flip angle = 27˚ (Ernst angle), total scan time is eight minutes. In practical experiments, two OVS bands are added on the top and bottom of FOV to suppress aliasing signals from outside. Additionally, a manual shimming is performed by experienced operators to provide a good shimming condition.

Besides the SPICE sequence, the overall scan protocol also includes one Localizer scan and one typical MPRAGE scan (FOV = 256 mm, matrix size = 256×256×192, resolution = 1.0×1.0×1.0 mm^3, TR = 2400 ms, TE = 2.13 ms, TI (inversion time) = 1100 ms, 192 slices, scan time = 4:40 min). MPRAGE scan provides the anatomical information for the setup of field of view and segmentation for further signal processing tasks (such as nuisance signal removal and regional analysis).

The resulting imaging capability of the proposed pulse sequence provides a significant improvement over traditional MRSI methods. To cover the same FOV and achieve the same spatial resolution for metabolite mapping, CSI-based sequences (spin-echo based, assuming TR as one second) would take 124×78×24×1 = 232128 seconds = 64.48 hours; EPSI-based sequence (spin-echo based, assuming TR as 1 second, and three echo-shifts are needed) would take 78×24×1×3 = 5616 seconds = 93.6 minutes; the basic SPICE method (spin-echo based, assuming TR as 1 second, and no echo-shift is needed) would take 78×24×1 = 1872 seconds = 31.2 minutes, but the proposed method only takes eight minutes, which is within the range of clinically acceptable scan time. Besides the imaging efficiency, the proposed method also has very unique capability to provide high-resolution water-based imaging and correct system imperfections like field variation induced

effects using the unsuppressed water signals. These special features make the proposed sequence easier to be carried out in practice.

3.5 Summary

A special data acquisition scheme is developed to significantly enhance the imaging capability of basic SPICE sequence. Combining efficient excitation, fast trajectories, sparse sampling strategies, and special navigator signals, the pulse sequence can successfully achieve rapid, high-resolution, robust MRSI in an 8-minute scan.

CHAPTER 4 – DATA ACQUISITION FOR WHOLE BRAIN ^{1}H-MRSI AT 7T

Ultrahigh field MR provides unique opportunities for MRSI to further enhance the imaging capability. In this chapter, we describe a new data acquisition scheme at ultrahigh field (7T) building on the proposed sequence at 3T as presented in Chapter 3. This new sequence utilizes the power of ultrahigh field and is designed with several special features to achieve whole-brain MRSI without increasing the scan time.

4.1 Pulse Sequence

The potential of using ultrahigh field systems for MRSI has long been recognized. The most striking and direct benefit of ultrahigh field is the enhanced SNR. Some comprehensive studies have shown that the SNR increases linearly to superlinearly with field strength in practical environment [95]. Since the most fundamental challenge of MRSI methods is low SNR, this enhancement of SNR brought by ultrahigh field is very beneficial for MRSI. This SNR benefit can lead to higher spatial resolution, shorter scan time, and more robust quantification results. In addition, the chemical shift dispersion also increases linearly with field strength, as shown in Equation (2.9). This increased chemical shift dispersion makes the peaks of different molecules more separated with each other on the spectra, which is especially beneficial for ^{1}H-MRSI whose spectra are rather crowded.

However, the increased magnetic field also poses several technical challenges on the MRSI development. First, it is well-known that stronger B_1 field inhomogeneity is present at ultrahigh field. For MRSI, B_1 field inhomogeneity not only causes spatial excitation inhomogeneity, but also makes it more difficult to suppress the water signals, which is required by most typical MRSI methods. Second, ultrahigh field also brings stronger B_0 field inhomogeneity, which can cause severe signals distortion and cancellation in MRSI. The effects of B_0 field inhomogeneity are especially large when the spatial resolution is low on the order of centimeters, which is often the case in conventional MRSI methods. Third, the energy deposition (measured by SAR) increases as the square of the field strength. Therefore, at ultrahigh field, the use of high SAR pulses like adiabatic pulses and 180 refocusing pulses are limited for MRSI. If these pulses are used, it may require a quite long TR, leading to a long total scan time. Fourth, the signal decay rate (measured by T_2*) decreases almost linearly with increased field strength, thus the conventional long-TE

MRSI would suffer from significant SNR loss due to this faster decay. Fifth, the increased spectral bandwidth at ultrahigh field also makes it difficult to satisfy the Nyquist sampling rate when using fast spatiospectral trajectories like EPSI trajectories, which has limited the use of fast trajectories at ultrahigh field.

Given these benefits and challenges of ultrahigh field, this thesis research further develops the SPICE method at 7T to achieve whole brain covered MRSI. First, whole brain MRSI is desired in neurological studies, especially combining with functional imaging and anatomical imaging, which usually require whole brain coverage. Second, increasing brain coverage requires an increased number of encodings, thus increased scan time. Traditional acceleration methods by sparse sampling would sacrifice SNR, and it can be compensated by the SNR improvement brought by ultrahigh field. Therefore, the enhanced SNR is utilized to further increase imaging volume of the SPICE method.

The proposed pulse sequence at 7T is built on the SPICE sequence described in Chapter 3 for 3T, and extended with a few special features, as shown in Figure 4.1. This sequence keeps some basic features of the 3T SPICE sequence, which are already very suitable for MRSI at ultrahigh field, such as FID-based acquisition; ultrashort TE; short TR; no water suppression; and embedded navigators. As discussed in Chapter 3, FID-based acquisition has higher SNR efficiency than traditional SE-based acquisition, and it has much lower energy deposition given the low flip angle and no 180-degree refocusing pulses. Lower energy deposition is desirable at 7T since the SAR at 7T is more than 4 times of the SAR at 3T given the same pulses. SE-based sequences, especially those where multiple 180-degree pulses are used, such as PRESS and LESER, are subject to the tight SAR limitation at 7T, thus typically a longer TR is needed. Additionally, FID-based acquisition has relatively higher insensitivity to the B_1 inhomogeneity, which is also a good characteristic at 7T. Ultrashort-TE (1.6 ms) can minimize the signal loss given the faster T_2* decay and shorter TR is preferred since signals would become very noisy at the end of TR. Removal of water suppression and lipid suppression is also essential, since it not only reduces SAR and enables short TR, but also provide water signals for correction of various system imperfections such as B_0 and B_1 inhomogeneities. Given the increased system imperfections and severer discomfort of subjects when lying in the 7T scanners, head motion would become a more challenging issue at 7T. So the motion navigators embedded in each TR are more necessarily needed for sequence robustness.

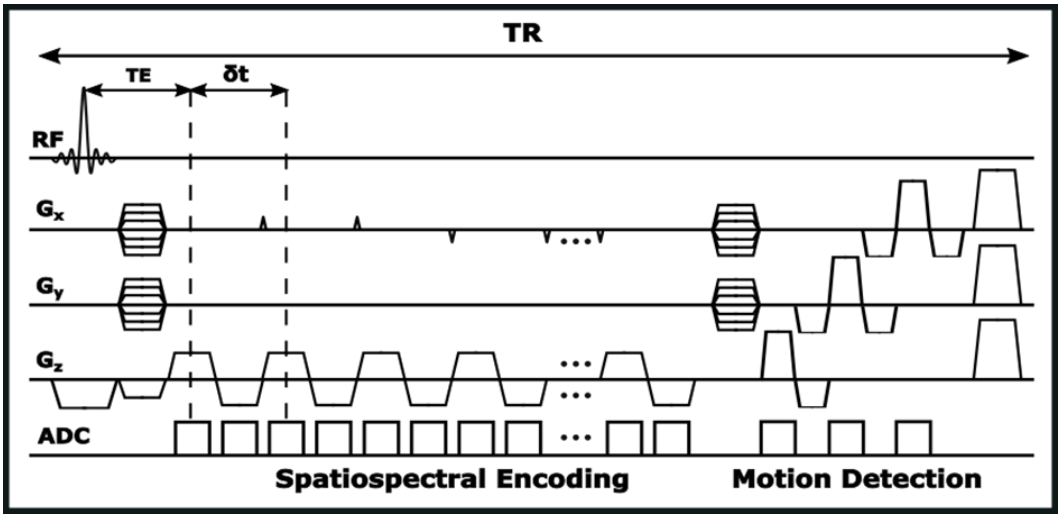

Figure 4.1: Pulse sequence diagram of the proposed data acquisition sequence at 7T. This sequence keeps basic features of the 3T SPICE sequence, including FID-based acquisition; EPSI trajectories; no water suppression; embedded motion navigator; and blipped gradients for sparse sampling. Additionally, this sequence changes the readout direction on the slice direction, which makes it more suitable for whole brain imaging.

Even though the proposed SPICE sequence at 3T has these features good for 7T, there are still a few technical issues if it was directly used for whole brain MRSI at 7T. First, using increased number of phase encodings to keep the spatial resolution while increasing imaging volume is very time-consuming. Specifically, if the FOV in slice direction is increased from 72 mm to 144 mm, then the number of encodings would be double, thus the imaging time will be twice as the sequence at 3T, which is more than 15 minutes. Second, larger spectral bandwidth is needed at 7T. For example, to cover the whole spectral range from 0 to 4.7 ppm, and assuming center frequency is on water (4.7 ppm), then the bandwidth needed at 3T is around 1200 Hz, and it becomes 2800 Hz at 7T. As discussed in Chapter 3, EPSI trajectories have a trade-off between the readout resolution and spectral bandwidth (echo-spacing), so the spatial resolution will be significantly reduced if we are to match the spectral bandwidth requirement at 7T. Third, even though SPICE sequence is a SAR efficient sequence with low flip angles, the saturation pulses used in OVS bands are spatial selective pulses with high SAR. These pulses can easily exceed SAR limitation at 7T but removing these pulses will introduce aliased signals from outside of the brain. To address these issues, the proposed sequence at 7T has two special acquisition features extending on the SPICE sequence at 3T, which include slice-direction readout and sparser sampling of (k, t)-space. The second feature will be described in the next section.

As shown in Figure 4.1, the EPSI readout gradients are placed in the slice direction (z-direction) instead of the typical x-direction. This change of readout direction has several advantages for whole brain MRSI at 7T. First, the number of encodings in slice direction is relatively smaller than the in-plane encodings, so better tradeoff can be achieved between resolution and echo-space. More specifically, the in-plane FOV is usually more than 200 mm (240 mm in the setup of the proposed method), and the excitation slab thickness is usually less than 200 mm even for whole brain imaging (150 mm in the setup of the presented method). To achieve the same spatial resolutions, e.g., around three mm, the number of encodings for in-plane directions is 80 while it is only 50 for slice direction. With fewer number of encodings, smaller echo-space thus wider spectral bandwidth can be achieved using EPSI trajectories. Furthermore, when ramp samplings are utilized, the echo-space can be further reduced. In the current implementation, 25 encodings are acquired at the flat top of readout gradients and 33 encodings are acquired at the ramp time (which is equivalent to 22 effective encodings), thus the resulting readout resolution is around 3.1 mm, and the echo space is 0.9 ms. Second, no additional oversampling in phase encodings or OVS are needed due to the readout oversampling. As mentioned in Chapter 3, in the sequence at 3T, two OVS bands are used to avoid the signals outsides the top and bottom of the FOV aliasing into the brain. Another strategy is also used to reduce the aliasing signals from the slice direction, which adds oversampling between the excitation slab and FOV. The sequence at 3T has 10% oversampling at both sides in the slice direction, so the excitation slab is 60 mm given the 72 mm FOV in slice direction. When changing the readout direction into the slice direction, the intrinsic readout oversampling (a factor of two) will make the acquisition FOV double, as 150×2 = 300 mm in slice direction. Therefore, no additional oversampling and OVS bands are needed any more, which also resolves the SAR issue caused by OVS bands at 7T. Third, this change puts the phase encodings in the in-plane directions (x and y directions), which are more efficient to utilize sensitivity profiles for parallel imaging. This can be elaborated in two aspects. On the one hand, in the in-plane directions, the number of encodings is usually more than that in the slice direction, so the truncation effects due to limited encodings will be less for parallel imaging. On the other hand, based on the design of modern head coils, more channels are usually distributed in the in-plane directions than slice direction, thus the sensitivity encoding efficiency is higher in in-place directions. Therefore, this feature can enable higher acceleration factors in

sampling (k, t)-space for reduction in scan time. More details on the sparse sampling of (k, t)-space are described in the following section.

4.2 Sparse Sampling of (k, t)-Space

Figure 4.2 shows the sparse sampling pattern of (k, t)-space in the proposed sequence at 7T. Similar to the discussion in section 3.2, the design of sampling is based on the consideration of largely different characteristics of water, lipid, and metabolite signals. The sampling of entire (k, t)-space is divided into three regions with variable density. More specifically, the central (k, t)-space region is fully sampled both spatially and temporally. The middle region is under-sampled by a factor of four spatially and fully sampled temporally. The under-sampling in this region follows the spatial CAIPIRINHA pattern, with an acceleration factor of two in each phase-encoding direction and a location shift in every second column. The outer region is sampled more sparsely with acceleration factors of two in each spatial direction and a factor of 20 sub-sampling temporally, which is achieved using spatiotemporal CAIPIRINHA sampling in (kx, t)-space. Moreover, the spatial sampling pattern also follows the spatial CAIPIRINHA pattern as the middle region.

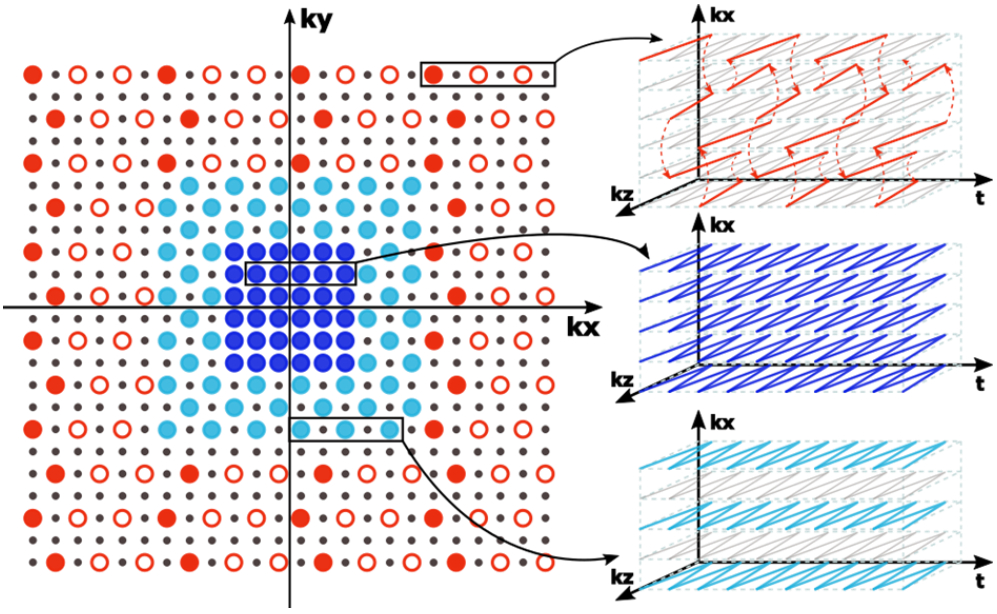

Figure 4.2: Sampling pattern of the proposed method in (k, t)-space. Entire (k, t)-space is sampled in three regions with variable density. The central region is fully sampled, while the middle region is spatially under-sampled by a factor of two in each direction. The outer region is sparsely sampled both spatially (a factor of four) and temporally (a factor of 20) for water and lipid signals.

Compared with the sparse sampling in the sequence at 3T, the sparse sampling at 7T adds a middle region with a moderate acceleration factor as four. Both the middle region and central region are used for metabolite signals while the sparse outer region is only for water and lipid signals. The under-sampling of the middle region is to reduce the scan time for metabolite signals. If the middle region is spatially fully sampled as the central region, then the total scan time would be much longer (e.g., more than 15 minutes). To preserve the SNR for metabolite signals, the acceleration in middle region is not high, just as two in each direction. And the SNR loss in this region can be compensated by the SNR enhancement brought by ultrahigh field. Moreover, no temporal under-sampling is applied, so the under-sampling in this region can be easily recovered by typical parallel imaging echo-by-echo, which does not disturb the temporal signals. It should also be noted that the under-sampling in two spatial directions is made workable by changing the readout into the slice direction, as described in section 4.1. The employment of CAIPIRINHA pattern in (kx, ky)-plane provides further improvement in reconstruction regarding to reduced aliasing and reduced noise amplification.

The sampling of central region is very similar to the sequence at 3T, which is to gain adequate SNR and provide estimates of spatial sensitivity profiles, field inhomogeneity maps, and data adaptive subspaces. The sampling of the outer region extends the sequence at 3T by adding under-sampling in the “blipped direction”. More specifically, the sequence at 3T has under-sampling in only one spatial direction if the temporal encodings are collapsed for spatial encodings, but this sequence at 7T has under-sampling in both spatial directions, and it also follows a CAIPIRINHA pattern. So, the overall acceleration factor in the outer region is higher than that in the sequence at 3T, and the sparse sampling in this region can also be overcome combining both parallel imaging and subspace modeling.

In current implementation, the entire (k, t)-space contains 120×120×58×280 encodings, with the central k-space region containing 32×32×58 spatial encodings, and the middle region 80×80×58 spatial encodings. Given the current sparse sampling as described above (Rx = Ry = 2 in middle region, Rx = Ry = 2, Rt = 20 in outer region), the overall acceleration factors would be 21 for water and lipid signals and 2.7 for metabolite signals. This level of sparsity makes the fast, high resolution, whole brain MRSI achievable in practice. In this implementation, the spatial resolution of water/lipid signals is not pushed high as the sequence at 3T, to nearly one mm. This is due to the consideration on computation load, since the data around one mm resolution will be

too large to be processed on our current computational platform, but there is no acquisition limitation to push higher resolution.

4.3 Implementation for Experimental Studies

In current implementation of this sequence at 7T, the parameters are summarized as follows: FOV = 240×240×150 mm^3, resolution of metabolites = 3.0×3.0×3.2 mm^3 (matrix size = 80×80×58), resolution of water and lipids = 2.0×2.0×3.2 mm^3 (matrix size = 120×120×58), TR = 150 ms, TE = 1.6 ms, echo-space = 0.9 ms, echo number = 140×2, readout bandwidth = 167 kHz, flip angle = 26˚ (Ernst angle), total scan time is eight minutes. Compared with the sequence at 3T, this sequence at 7T does not include OVS bands, so the TR is shortened to 150 ms for reducing scan time. Manual shimming is still required in operation and typical scans including Localizer and MP2RAGE (FOV = 256 mm, matrix size = 256×256×256, resolution = 1.0×1.0×1.0 mm^3, TR = 4400 ms, TE = 2.17 ms, echo-space = 6.8 ms, flip angle-1 = 4˚, flip angle-2 = 5˚, TI-1= 750 ms, TI-2 = 2950 ms; 256 slices, scan time = 8:02 min) are also included in the experiments.

To achieve the same spatial resolution with the same FOV for metabolite mapping, the proposed acquisition sequence has a significantly improved acquisition efficiency. More specifically, spin-echo CSI-based sequences (assuming TR as one second) would take 80×80×58×1 = 371200 seconds = 103.11 hours; spin-echo EPSI-based sequence (assuming TR as one second, and four echo-shifts are needed) would take 80×58×1×4 = 18560 seconds = 5.15 hours; the spin-echo based SPICE method (assuming TR as one second, and no echo-shift is needed) would take 80×58×1 = 4640 seconds = 77.3 minutes; the SPICE sequence directly converting from 3T as discussed in the last chapter will take around 15 minutes; and the proposed method at 7T only takes eight minutes. Similarly as the sequence at 3T, the proposed method at 7T also provides high-resolution water-based imaging and corrects system imperfections using the unsuppressed water signals. Besides, the removal of OVS bands makes it no need to worry about the SAR limitation in the practical experiments.

4.4 Summary

A special data acquisition scheme is designed building on the SPICE sequence at 3T, which takes advantage of the SNR benefit and overcomes the challenges brought by the ultrahigh field (7T).

Extending the SPICE sequence at 3T with slice-direction readout and sparser (k, t)-space sampling, the pulse sequence can achieve ultrafast, high-resolution, whole-brain MRSI in an eight-minute scan.

CHAPTER 5 – DATA PROCESSING WITH LEARNED SPATIOSPECTRAL MODEL

In this chapter, we present the special data processing approaches for generating high-quality spatiospectral functions of multiple molecules from the sparse measurement collected by the proposed pulse sequence. The processing methods are based on the union-of-subspaces signal model with the subspaces being pre-learned from training data, incorporating spatial priors as constraints. The algorithms for subspace learning and reconstruction from sparse and noisy data will be discussed. We also present the practical methods for correcting system imperfections, including strong B_0 inhomogeneity, B_1 inhomogeneity, frequency drift and subjects' head motion. These methods are generally applicable for both 3T and 7T, so they are not discussed separately for different strength unless necessary.

5.1 Union-of-Subspaces Model

Compared with the traditional MR imaging, MRSI increases dimensionality of the imaging problem by adding one spectral dimension. This high dimensionality significantly increases the degrees-of-freedom; thus, a huge number of encodings are needed under the traditional Fourier imaging framework. As introduced in section 2.4, the subspace model based on partial separability can significantly reduce the degrees-of-freedom and facilitate high quality signal denoising and reconstruction [33]. In this thesis work, the signal processing tasks are more complicated than the basic SPICE method introduced in section 2.5, since no water/lipid suppression is applied, and the data space is highly sparse sampled. Therefore, the subspace imaging framework is extended by using a union-of-subspaces model for addressing the new processing tasks. More specifically, the spatiotemporal function of each molecule (water, lipids, metabolites, etc.) is represented using a very low-dimensional subspace, and the overall signal is expressed as the sum of these subspaces instead of one single subspace:

$$\rho(x,t) = \sum_{n=1}^{N} \rho_n(x,t) = \sum_{n=1}^{N} \sum_{l=1}^{L_n} u_{n,l}(x) v_{n,l}(t) \tag{5.1}$$

where $\rho(x,t)$ denotes the overall spatiotemporal signal, $\rho_n(x,t)$ the signal of the n^{th} molecule, $\{v_{n,l}(t)\}$ the temporal basis functions, and $\{u_{n,l}(x)\}$ the corresponding spatial coefficients. In practice, it can be justified that the sum of model orders $\sum_{n=1}^{N} L_n$ is small, since there are only a

small number of molecules and tissue types in the human brain. In principle, this union-of-subspaces model is included in the single subspace model in Equation (2.16), both of which can significantly reduce the degrees-of-freedom and facilitate many special processing methods. But Equation (5.1) is more flexible to represent the signal containing molecules with largely different characteristics. In other words, the basis functions are grouped for different molecules, and each group of basis functions may have very different properties with others. This provides many benefits in subspace determination, separation of signal components, and incorporation of different constraints to different molecules in reconstruction.

As discussed before, one critical element of subspace-based models is the determination of subspace structures. In the basic SPICE method, water and lipid signals are suppressed in the acquisition stage and removed in processing prior to reconstruction. Therefore, only one subspace is needed for metabolite signals, and the subspace structure is estimated from the acquired D_1 dataset directly. This subspace estimation strategy is good at producing data-consistent and data-adaptive subspace, but the generated subspace may be contaminated by field inhomogeneity effects, measurement noise, and residual nuisance signals given the limited number of encodings in D_1. Increasing the number of encodings of D_1 acquisition can help mitigate these effects, but it would tremendously increase the scan time.

Given the proposed acquisition sequence and the union-of-subspaces model, the determination of subspaces for water, lipids, and metabolites are all needed. Instead of estimating these subspaces from a companionly acquired dataset as D_1, a subspace learning strategy is used to estimate these subspaces from multiple sets of pre-acquired training data [91].

5.2 Subspace Learning

To generate the sets of spectral basis functions, the learning strategy used in this thesis research combines prior information from both quantum mechanics simulations (physics-based priors) and pre-acquired training data (distribution priors). More specifically, for the spectroscopic signals of one specific molecule, the deterministic resonance frequency structure is determined by quantum mechanics simulations with known chemical structures and related parameters, and the distribution of spectral parameters depending on the experimental environments (like linewidth and frequency drift) is estimated from training data.

Considering a spectroscopic signal from a specific molecule (denoted as n^{th} molecule), it can be modelled as follows (the overall constant scale is discarded for simplicity):

$$s_n(t) = \varphi_n(t) e^{-t/T_{2,n} + i2\pi f_n t} h(t) \tag{5.2}$$

where $\varphi_n(t)$ represents the resonance frequency structure of this molecule, including chemical shift and spin-spin coupling; $T_{2,n}$ and f_n denote the T_2 relaxation time (which determines the spectral linewidth) and frequency shift of this molecule, respectively; $h(t)$ is an overall compensation function accounting for the line-shape variations in practical experimental environments (caused by intra-voxel field inhomogeneities, etc.). This modulating function is modelled as a generalized-series (GS) compensation function [85]:

$$h(t) = \sum_{m=-N_{\text{gs}}}^{N_{\text{gs}}} c_m e^{-i2\pi m \Delta f t} \tag{5.3}$$

where N_{gs} is the GS model order, which is usually small in practice; c_m the GS coefficient and Δf the frequency step.

The signal model in Equation (5.2) can be regarded as a generalized form of the FID signal formulation in Equation (2.10), based on several practically feasible assumptions. First, the chemical shift coefficients and spin-spin coupling coefficients do not change with experimental environments, so the integral of all the frequency components from a molecule can be represented using a single $\varphi_n(t)$. Second, the transversal relaxation process and frequency shift caused by the external magnetic field have overall effects for one molecule, even it has multiple nuclei (protons as discussed in ^{1}H-MRSI) with different chemical shifts. With these, the integral of Equation (2.10) can be represented by $\varphi_n(t) e^{-t/T_{2,n} + i2\pi f_n t}$. Third, the effects of environmental variations can be captured by the GS model. This can be justified in a few aspects: with a large enough model order, the GS model can be used to present any signals; considering the signal without the GS term as a reference signal, GS model is optimal to express the measured signal in the sense of maximizing cross-entropy [106]; the field inhomogeneity effects can be regarded as a spatial convolution, and the GS model can be regarded as a convolution model in spectral domain, so the GS model is a fair linear model for the general field effects under spatial smoothness conditions.

Generating physical basis functions of metabolite signals ($\varphi_n(t)$ in model Equation (5.2)) through quantum mechanics simulations have long been part of NMR studies. Through many years

of development, there have been many software and toolboxes for generating basis functions by simulation, such as NMR-SCOPE, GAMMA, GAVA, Spinach, and JMRUI [107]–[113]. Most of the simulation methods are based on the density matrix formulation, which allows determination of the measurement of MR signals for a specific molecular spin system under specific experimental conditions such as field strength and pulse sequence. There are a few parameters that describe physical properties of the molecular spin system, which are needed in the quantum mechanics simulation, including chemical shifts, spin-spin coupling constants, and relaxation times (which are optional). These parameters of the typically detectable molecules have been carefully quantified and are already well established to the society. In this work, the physical basis function of typical measurable brain metabolites (including NAA, Cr, Cho, Ins, Glu, Gln, GABA, Lac, etc.) are simulated using GAMMA tool embedded in the Vespa package [114].

The spectral parameters, $T_{2,n}$, f_n, and h are not as deterministic as the physical basis functions, they vary in different experiments, subjects, and in different voxels. But it is assumed that under the normal physiological conditions and similar environmental conditions, the variations of $T_{2,n}$ and f_n are small and their distributions are similar between different experiments. Furthermore, it has been shown that the distributions of parameters $T_{2,n}$ and f_n reside on a non-linear low-dimensional manifold in high-dimensional vector space, and this manifold can be approximated by using a linear subspace [91]. Therefore, the distributions of these spectral parameters can be learned from training data by estimating linear subspaces. The modulating function $h(t)$ varies more from experiment to experiment mainly due to practical factors like B_0 field inhomogeneity and eddy current. It is very challenging to approximate a consistent and useful distribution from prior scans. However, for water and lipid signals, these effects can be mitigated and corrected when spatial resolution is high; for metabolite signals whose resolution is usually very low, the effects are assumed to be global, which means the effects on metabolites signals are the same on water signals if there are any. Since the proposed sequence does not suppress water signals, the modulating function can be estimated from the companion unsuppressed water signals.

The procedure to learn subspace for a specific molecule from training data is summarized as follows. Assuming the physical basis function of this molecule ($\varphi_n(t)$) has been generated by quantum simulation and the set of training data contains many points of spectra, the modulating function $h(t)$ is first estimated. More specifically, for water and lipid signals, which are of enough SNR, $h(t)$ can be estimated by directly fitting the spectral signals to Equation (5.2); for metabolite

signals, which do not have sufficient SNR, the $h(t)$ estimated from the companion water signals are used. With $h(t)$ determined, the spectral parameters $T_{2,n}$ and f_n can be estimated by fitting to Equation (5.2). The fitting method used is based on a time-domain fitting method [115]. Then, the spectral parameters from many samples are obtained, which are assumed to follow the underlying distribution. To capture the distribution using a subspace, a collection of spectral signals is re-generated using Equation (5.2) with the estimated parameter, and these spectra are arranged into a Casorati matrix as follows:

$$\begin{bmatrix} s_n(t_1;\theta_n^1) & s_n(t_2;\theta_n^1) & \dots & s_n(t_{N_t};\theta_n^1) \\ s_n(t_1;\theta_n^2) & s_n(t_2;\theta_n^2) & \dots & s_n(t_{N_t};\theta_n^2) \\ \vdots & \vdots & \ddots & \vdots \\ s_n(t_1;\theta_n^N) & s_n(t_2;\theta_n^N) & \dots & s_n(t_{N_t};\theta_n^N) \end{bmatrix} \tag{5.4}$$

where θ_n is the spectral parameter set learned from a specific voxel and $s_n(t)$ is the generated spectral signal using the fitting spectral parameters. Then the set of basis functions $\{v_{n,l}(t)\}$ is estimated using SVD on the Casorati matrix and are selected as the right-singular vectors. These basis functions simply capture the distributions of signal variations in the training data. As discussed, different basis functions are estimated for different molecules and then they are used in different aspects of the data processing.

Different sets of training data were acquired for the subspace learning. For the water and lipid signals, the training data was acquired using the SPICE sequence as described in section 3.4 and section 4.3. But for these sequences, only basic spatial under-sampling was employed for acceleration, not any spatiotemporal under-sampling (like using the CAIPI trajectories). This purely spatial under-sampling was easily overcome using basic parallel imaging methods without imposing subspace constraints, so the spectral properties of water/lipid signals were well preserved. For the metabolite signals, two SPICE sequences were performed sequentially, one with water suppression/lipid suppression and the other one without suppression. Then the spectra for training were obtained from the water/lipid suppressed data after nuisance removal and various correction utilizing the water/lipid unsuppressed data. Since for each 3D data there are tens of thousands of spatially resolved spectra which can be used for training, only data from a few subjects were acquired for the subspace training. It should be noted that separated subspaces were generated for different scanners and different cohorts of subjects (like healthy controls and patients

with specific diseases). The processing of this data followed the learning procedure as described above.

5.3 Reconstruction of Sparse Water/Lipid Signals

Given the data acquisition scheme, one of the key processing issues is to overcome the sparse sampling. As described in section 3.2 and section 4.2, the (k, t)-space is sparsely sampled in variable density. For both sequences at 3T and 7T, the central k-spaces are fully sampled, and outer k-spaces are spatiotemporally sparsely sampled using CAIPIRINHA trajectories. But the sequence at 7T has a middle k-space region where there is only spatial under-sampling. In this section, the reconstruction for the middle k-space at 7T (with only spatial under-sampling) is first discussed, then the reconstruction for regions with both spatial and temporal under-sampling follows.

In middle k-space of the 7T sequence, the acceleration factors are only 2 in both kx and ky directions, which can be addressed using basic parallel imaging methods. The data in central and middle k-space are used not only for reconstruction of water and lipid signals with relatively low resolutions, but also for reconstruction of the metabolite signals. So, the reconstruction in these regions needs to preserve temporal signal patterns and avoid filtering out low-intensity metabolite signals. We use an echo-by-echo GRAPPA+SENSE strategy to recover the under-sampled k-space for each time point, which may minimize the perturbation of reconstruction on the temporal signal pattern [23], [24]. First, the GRAPPA k-space convolution kernel is estimated from the fully sampled central k-space of early a few echoes, then the GRAPPA kernel is used to interpolate the missing data in these echoes. These processing steps follow the original GRAPPA method (as shown in Equation (2.15)) but involve more data from multiple echoes for estimating the kernel [24]. With reconstructed alias-free images of these echoes, a set of coil sensitivity maps at the same resolution can be estimated under simple assumption that the sum-of-square of the coil sensitivity maps is uniform:

$$E_c(\boldsymbol{x}) = \frac{\rho_c(\boldsymbol{x})}{\sqrt{\sum_{c=1}^{N_c} |\rho_c(\boldsymbol{x})|^2}} \tag{5.5}$$

where N_c is the total number of coil channels, $E_c(\boldsymbol{x})$ and $\rho_c(\boldsymbol{x})$ are the sensitivity function and image of the c_{th} channel, respectively. Then, these coil sensitivity maps are used for SENSE reconstruction on the data (including both central and middle k-space) of all the echoes. The echo-by-echo SENSE

reconstruction is implemented as solving the inverse problem in Equation (2.14) through linear least-square solver. Since the SENSE reconstruction is a linear process, this reconstruction strategy can minimize the effects on the temporal patten, thus preserving the metabolite signals in these k-space regions.

In the outer k-space of both 3T and 7T sequences, the measurements are highly sparsely sampled, so it requires very strong prior information to recover the missing (k, t)-space data. Since data in these regions is only used for reconstruction of high-resolution water and lipid signals, temporal constraints such as subspace structures of water and lipids are safe to use. More specifically, this reconstruction issue is solved using a constrained reconstruction method, which incorporates sensitivity encodings, pre-learned subspace structure, spatial supports of different signals, and spatial smoothness constrains [92]. This reconstruction was formulated as solving the following optimization problem:

$$\widehat{U}_w, \widehat{U}_f = \arg\min_{U_w, U_f} \sum_{c=1}^{N_c} \left\| d_c - \Omega\{\mathcal{F} S_c B(M_w U_w V_w + M_f U_f V_f)\} \right\|_2^2 + \lambda_w \|D U_w\|_2^2 + \lambda_f \left\| D U_f \right\|_2^2 \qquad (5.6)$$

where d_c is vector form of the measured (k, t)-space data of the c^{th} coil channel. V_w, V_f are matrix form of the pre-learned water and lipid basis functions from training data, and U_w, U_f are the corresponding spatial coefficients to be determined. M_w and M_f are masks for the spatial support of brain tissue and subcutaneous lipids. Ω, $\mathcal{F}$, S_c, B, and D are operators representing (k, t)-space sampling, Fourier transform, sensitivity encoding, field inhomogeneity, and edge-preserved total variation, respectively. In current implementation, the coil sensitivity map and B_0 field map are estimated from the images of low-resolution k-space regions (central region in the 3T sequence; central and middle regions in the 7T sequence) by sum-of-square method shown in Equation (5.5) and a linear HSVD (Hankel Singular Value Decomposition) fitting [116], respectively; the edge map is derived from the high-resolution anatomical image of MPRAGE using image local gradients. The regularization parameters λ_w and λ_f are chosen based on the discrepancy principle. After solving this optimization problem, the spatiospectral functions of water and lipids can be synthesized using the estimated spatial coefficients $\widehat{U}_w$ and $\widehat{U}_f$, as $\rho_w = \widehat{U}_w V_w$ and $\rho_f = \widehat{U}_f V_f$.

5.4 Reconstruction of Noisy Metabolite Signals

After reconstruction of the sparse data as described in the last section, the remaining key processing issues include (1) separation of water/lipid signals with metabolite signals (also known as nuisance removal issue) and (2) reconstruction of metabolite signals from the noisy measurements (similar as a typical denoising issue).

The nuisance removal task mainly includes the removal of water and lipid signals. The signal intensity of the water and lipid signals is more than three orders of magnitude higher than that of metabolite signals. In normal physiological conditions, lipids only exist in the subcutaneous layer of the brain, which do not overlap with the metabolite signals. However, given the limited spatial encodings of MRSI methods, the ringing of lipid signals would leak into the brain and overwhelm the metabolite signals in traditional Fourier reconstruction. Water signals have different frequency distributions (around 4.7 ppm) with the metabolite signals (mainly within 1.0 - 4.0 ppm), but given the large intensity of water signals, the tail of its spectra can overlap with the metabolite signals. To address these issues, processing methods incorporating the reconstructed high-resolution water and lipid signals (as described in the last section) are used, which are based on the previously reported nuisance removal methods [117]–[119]. A very brief discussion is included below.

For lipid removal, one of the typical methods uses a Papoulis-Gerchberg (PG) based algorithm to compute the ringing signals from the subcutaneous layer given the boundary condition, which has achieved many encouraging results. However, given the limited spatial encodings of MRSI data and not sufficiently accurate boundary condition, PG-based methods usually only achieve very limited performance in terms of k-space extrapolation of lipid signals. The proposed method can have high-resolution lipid signals as shown in the last section, which already has significantly reduced lipid ringing. Using PG-based methods on the high-resolution lipid signals for further k-space extrapolation can reduce the requirement on PG-extrapolation and tremendously improve the lipid removal performance.

For water removal, the subspace-based method shown in [117] has very good performance in brain tissues with relatively small field inhomogeneity and susceptibility effects. However, in brain regions such as frontal lobe near the sinuses where large susceptibility exists, the water signals are strongly distorted, thus they are very difficult to be removed. The distortion of water signals is mainly due to the combination of field inhomogeneity and convolution effects of limited spatial encodings. In the regions of large field inhomogeneity, the adjacent spatial locations have largely

varied frequencies. If the resolution is large enough, the water signals will have good spectral shape without distortion. But when the resolution is limited, the water signals from adjacent locations with different frequency are summed together, leading to signal cancellation and distortion. Therefore, the high-resolution water signals provided in the proposed method can help resolve the distortion of water signals, thus it can result in better removal of water signals, especially in the regions with large field inhomogeneity.

After the nuisance removal, the remaining metabolite signals were buried in the measurement noise given their low-concentrations and high-resolution. This reconstruction task was addressed using subspace modeling and anatomical constraints as the basic SPICE method while integrating pre-trained basis functions obtained as described in section 5.2. This reconstruction is formulated as solving the following optimization problem:

$$\widehat{U}_m = \arg\min_{U_m} \left\| d_r - \mathcal{F}\left(\sum_{m=1}^{M} U_m V_m\right)\right\|_2^2 + \sum_{m=1}^{M} \lambda_m \|D U_m\|_2^2 \tag{5.7}$$

where d_r is vector form of the noisy (k, t)-space data after nuisance removal as described above. V_m represent the pre-learned basis functions of the m^{th} molecule and U_m the corresponding spatial coefficients. It should be noted that data d_r are coil-combined and field-corrected after nuisance removal. After reconstruction, the spatiospectral functions of different molecules can be generated as $\rho_m = \widehat{U}_m V_m$.

5.5 Correction of System Imperfections

MRSI methods are relatively sensitive to system imperfections like B_0 inhomogeneity, B_1 inhomogeneity, field drift, and head motion [37], [38]. Significant artifacts will appear if they are not properly corrected. As described in session 3.4, the unsuppressed water signals and embedded navigator signals in the proposed method can provide very unique opportunities for solving these issues.

B_0 field inhomogeneity can cause frequency shift, broadened spectral linewidth, and signal distortion in MRSI. Traditional MRSI methods require an additional GRE or water unsuppressed MRSI scan to obtain B_0 field map for correction. The proposed method does not need additional scans, high-resolution B_0 field map can be derived from the companion water spectroscopic signals

through fitting methods like HSVD. This high-resolution field map can be used to correct the B_0 inhomogeneity effects effectively.

B_1 inhomogeneity usually causes significant spatial shading effects, especially at ultrahigh field while using coils with large channel numbers (e.g., 64-channel coils). Without correction, the B_1 inhomogeneity would impose additional spatial variation to the metabolite distributions. In conventional experiments, a couple of additional scans are needed to map the B_1 field. The unsuppressed water in the proposed method can provide a good reference to derive B_1 map. Specifically, under the assumption that the B_1 field should be spatially smooth, and they have the same shading effects on both water and metabolite signals, the B_1 field can be estimated from the water image through a spatial polynomial fitting. Then, this B_1 field map (weighting map) can be used to correct the shading effects in metabolite signals.

The correction of field drift and head motion depends on the navigator acquisitions as described in Chapter 3. The short FID signals for estimating field drifts (frequency drifts) are acquired every 60 TRs. Under the assumption that the field drift is a smooth process along time, the frequency shifts estimated every 60 TRs are interpolated to each single TR using a polynomial fitting. Then these estimated frequency shifts can be used to correct the data in each TR.

The head motion is detected using the linear navigators at the end of each TR. The spatial shifts of head in three axes can be estimated using the linear navigators by computing the shifts of their projection profiles. Instead of using the estimated spatial shifts to correct the k-space data, the proposed method uses an interpolation-based strategy. More specifically, data in the TRs with large estimated spatial shifts are identified as motion-corrupted data. The data in these TRs are discarded from the measurements, and then the discarded (k, t)-space data is interpolated using the remaining (k, t)-space data (denoted as motion-free data) through parallel imaging with additional spatial constraints. This interpolation is done by solving the following optimization problem:

$$\hat{\rho} = \arg\min_{\rho} \sum_{c=1}^{N_c} \left\| d_c - \Omega_{mf} \mathcal{F}(S_c \rho) \right\|_2^2 + \lambda \| W \nabla \rho \|_2^2 \tag{5.8}$$

where d_c denotes the motion-free data of c^{th} coil, Ω_{mf} the k-space sampling operator for motion-free data, $\mathcal{F}$ the Fourier transform operator, S_c the spatial sensitivity map, N_c the channel number of coil, ∇ the total variation operator and W a spatial weighting derived from anatomical images.

After reconstruction, the motion-corrected data $\hat{d}_c$ is synthesized using the reconstructed (interpolated) data and the measured data:

$$\hat{d}_c = \Omega_{\mathrm{mc}}\mathcal{F}(S_c \odot \hat{\rho}) + \Omega_{\mathrm{mf}}d_c \tag{5.9}$$

where Ω_{mc} is the k-space sampling for the motion-corrupted data. Overall, the motion correction process can be regarded as a SENSE-based k-space interpolation.

5.6 Summary

In summary, the union-of-subspaces model has enabled separation and reconstruction of the spatiospectral functions of different molecules from the sparse and noisy measurements. Based on this subspace model, incorporating a subspace learning strategy, special processing approaches are used to address the challenging processing tasks. Moreover, the high-resolution water/lipid signals are also utilized to improve the removal of nuisance signals and correct system imperfections, including B_0 inhomogeneity, B_1 inhomogeneity, field drift, and head motion.

CHAPTER 6 – ^{1}H-MRSI EXPERIMENTAL RESULTS

To demonstrate the feasibility and to evaluate the performance of the proposed ^{1}H-MRSI methods at both 3T and 7T, both phantom experiments and in vivo experiments have been carried out. The sequence at 3T has also been performed on tumor patients to show its potential clinical values. This chapter presents all the results obtained from both 3T and 7T.

6.1 Phantom Experiments at 3T

The 3T phantom experiments were performed on a uniform sphere phantom (SPECTRE phantom, Gold Standard Phantoms LTD) on a Siemens Prisma scanner (Siemens Healthcare, Erlangen, Germany). The phantom is of 150 mm diameter and is filled with water-based liquid and a set of brain metabolites/neurotransmitters (including NAA, Cr, Cho, Ins, Glu, Lac and GABA) at physiological concentrations (NAA: 12.5 mM, Cr: 10.0 mM, Cho: 3.0 mM, Ins: 7.5 mM, Glu: 12.5 mM, Lac: 5.0 mM, GABA: 2.0 mM). The sequence protocols are the same as described in section 3.4. The SPICE sequence was scanned twice for analyzing test-retest reproducibility (FOV = 240×240×72 mm^3, resolution of metabolites = 2.0×3.0×3.0 mm^3 (matrix size = 124×78×24), TR = 160 ms, TE = 1.6 ms, echo-space = 1.76 ms, echo number = 74×2, readout bandwidth = 167 kHz, flip angle = 27˚, scan time = 8 minutes).

A series of results are displayed in Figure 6.1-6.4, showing performance of the proposed method in noise reduction, accuracy, and reproducibility. Figure 6.1 shows a comparison of results using Fourier reconstruction and using SPICE reconstruction. From both spatial distributions (metabolite maps) and spectral distributions (localized spectra), it is obvious that SPICE reconstruction significantly improves SNR and produces high-quality MRSI results. From the reconstructed spectra, we can see clear peaks of NAA, Cr, Cho, Lac, Ins, and overlapped Glu and GABA after SPICE reconstruction, while they are buried under noise in the Fourier reconstruction. To verify the denoising results, a low-resolution but high SNR data was generated from the measured data. Specifically, the resolution of raw data was reduced by a factor of eight (two in each spatial dimension) via k-space truncation, and Hamming windows were added in all three spatial dimensions. So the “effective” resolution was approximately around 60 times lower than the original raw data, but this reduced-resolution improved SNR in the voxel. The comparison between this low-resolution data and SPICE reconstruction is shown in Figure 6.2. The localized

spectrum of SPICE reconstruction shows good consistency and similar noise level with that of low-resolution data, while the SPICE reconstruction keeps a much higher spatial resolution.

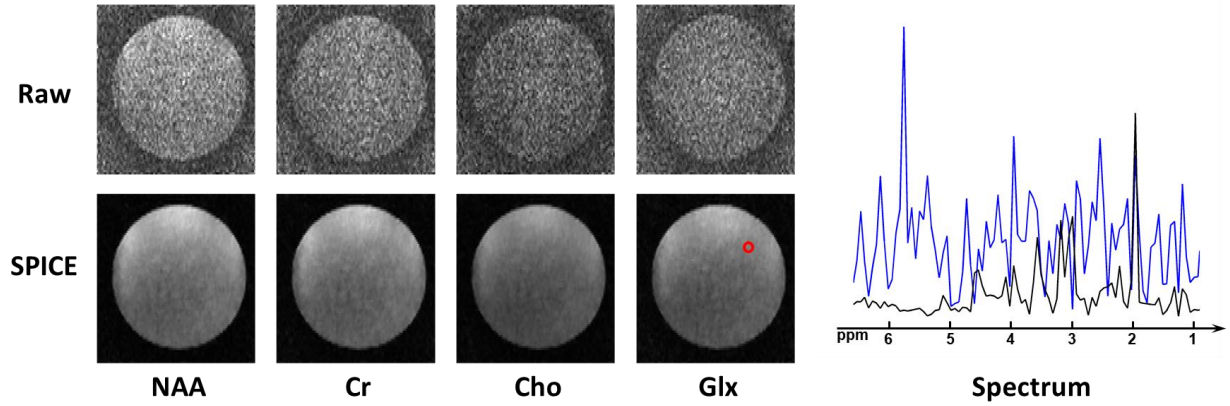

Figure 6.1: Comparison of raw data and SPICE reconstruction results, including metabolite maps and localized spectra (Raw data in blue spectrum, SPICE results in black spectrum). The displayed SPICE spectrum was scaled by a factor of 2.

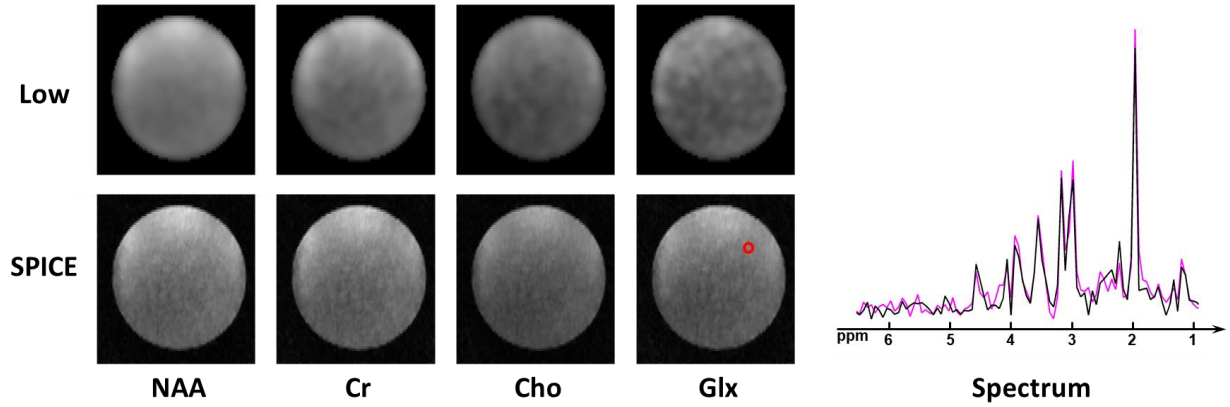

Figure 6.2: Comparison of low-resolution data and SPICE reconstruction results, including metabolite maps and localized spectra (low-resolution data in pink spectrum, SPICE results in black spectrum).

Figure 6.3 shows the resulting metabolite maps and localized spectra from two repeated SPICE scans on this phantom. Good agreements were found in both spatial maps and spectra. A more quantitative analysis was done, with R^2-plots and Pearson's correlation coefficients shown in Figure 6.4. Good reproducibility was successfully achieved on this phantom data (Pearson's correlation coefficients for NAA: $\gamma = 0.9593$; for Cr: $\gamma = 0.9563$; for Cho: $\gamma = 0.9561$; for Glx (denoted for Glu+GABA here): $\gamma = 0.9403$), which is a result of the significantly improved SNR.

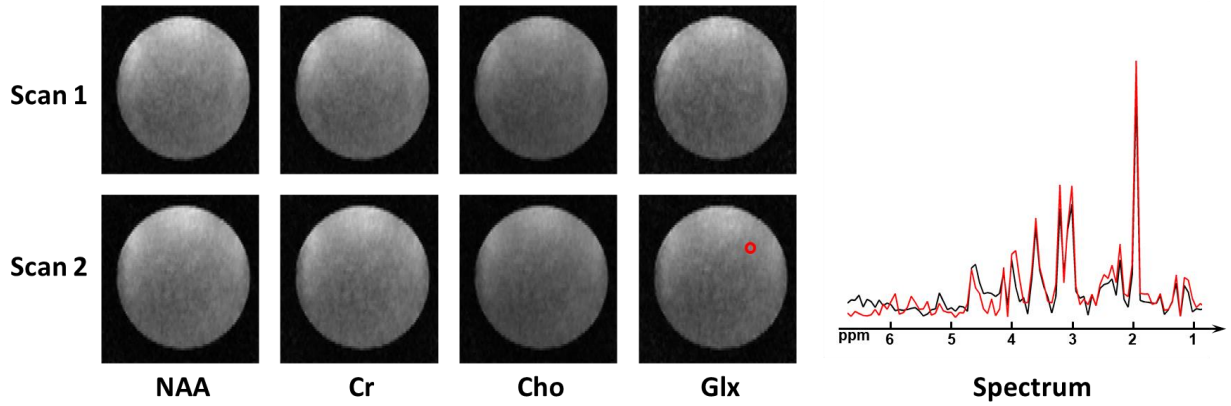

Figure 6.3: Comparison of SPICE results in two repeated scans, including metabolite maps and localized spectra from the same spatial location.

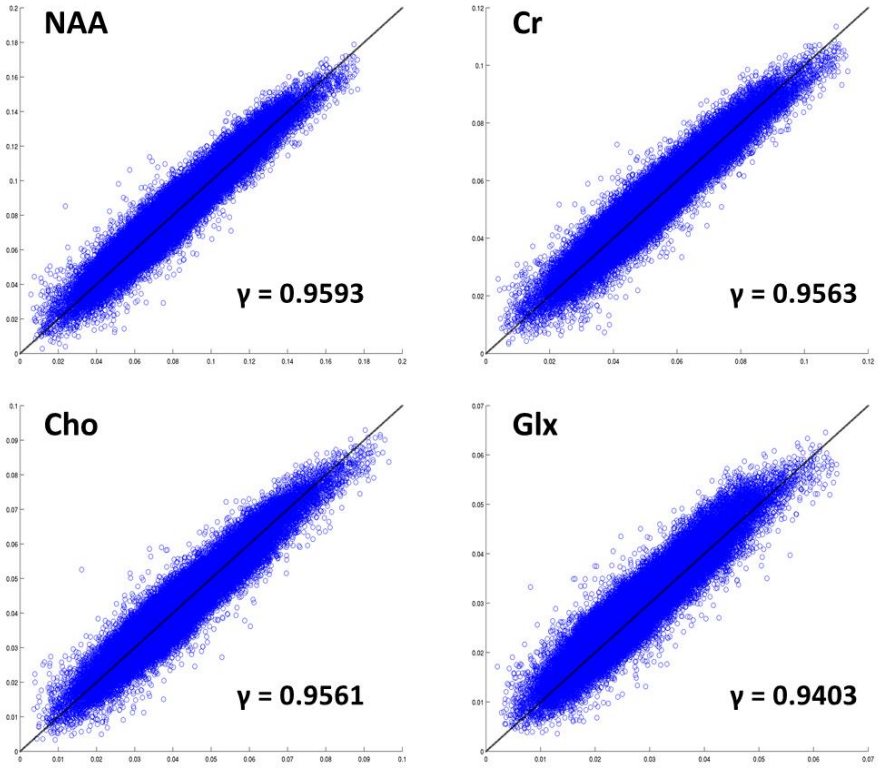

Figure 6.4: R^2-plots of four metabolites including NAA, Cr, Cho and Glx (Glu+GABA) in two sequential repeated SPICE scans. Identical line is shown in black. Pearson correlation coefficients are also computed and displayed.

This set of phantom results show that the SPICE method at 3T is able to achieve high-SNR and well reproducible MRSI results from an 8-minute scan in an in vitro environment using a standard metabolite phantom. The special data acquisition sequence, combining with a subspace

model, provides significant improvement on SNR, that enables higher spatial resolution and more robust and reproducible results.

6.2 In vivo Experiments at 3T

The 3T *in vivo* experiments on healthy volunteers were also carried on the Siemens Prisma scanner (Siemens Healthcare, Erlangen, Germany). The scans were approved by the Institutional Review Board of University of Illinois, and written informed consent was obtained before the scan. The scan protocol of SPICE sequence is the same as described in section 3.4. The reconstruction of metabolite signals and water signals is described in Chapter 5.

Figure 6.5 displays a set of representative results, including high-resolution metabolite maps (including NAA, Cr, Cho, and Ins at 2.0×3.0×3.0 mm^3 nominal resolution, four different slices of the brain are shown) and high-quality spatially resolved spectra. From the metabolite maps, we can see good contrast of metabolites given the high-resolution capability. For example, higher creatine in gray matter than white matter, and low metabolite signals in brain ventricles are clear in the results, which match the observations in literature. The localized spectra also show decent SNR and reasonably separated spectral peaks from main detectable metabolites.

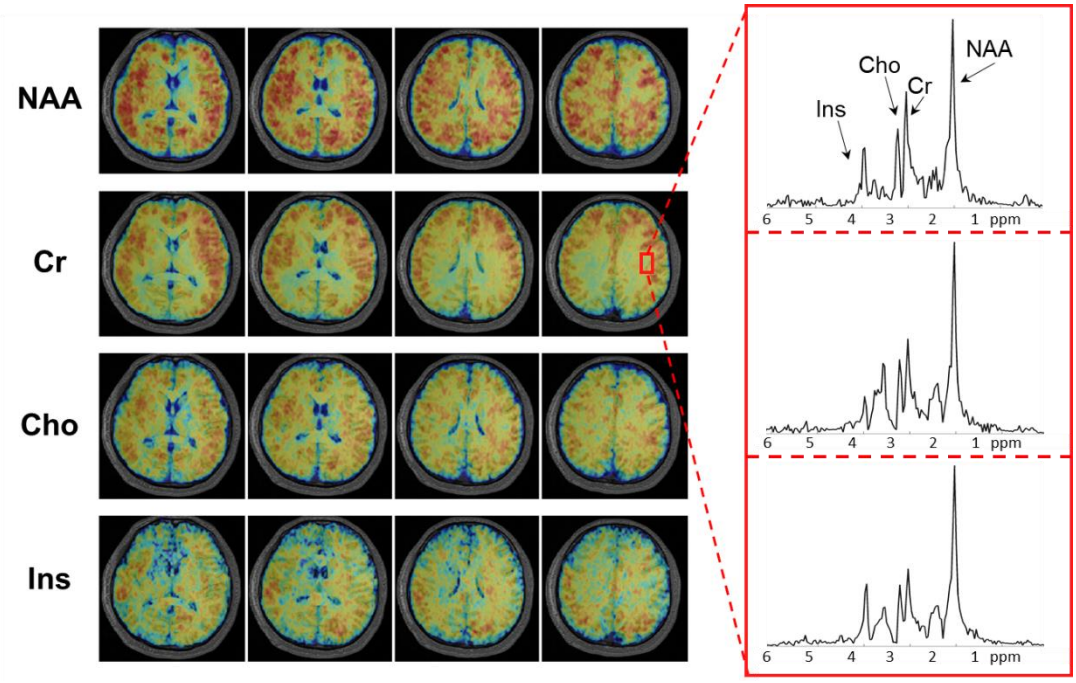

Figure 6.5: High-resolution metabolite maps (including NAA, Cr, Cho, and Ins) and localized spectra obtained from a healthy subject.

Besides high-resolution metabolite signals, the proposed method also generates higher-resolution water signals (at 2.0×1.0×1.0 mm^3 nominal resolution), which can be used to provide structural information. Susceptibility mapping (QSM) is one of the imaging modalities that can be extracted from the water spectroscopic signals. QSM can quantitatively map tissue susceptibility and it has been widely used for study of brain fine-structures like veins. Spatial resolution is critical to QSM, but MRSI sequences usually have low spatial encoding efficiency since they need to sample the temporal signals. The proposed method addresses this issue by using sparse sampling with spatiotemporal trajectories in outer (k, t)-space (as discussed in section 4.2). This sparse sampling helps to achieve high-resolution of water signals while keeping fast imaging speed; it takes around one minute to cover outer (k, t)-space but increases the resolution by a factor of nine. The resulting QSM map compared with that obtained using only central k-space (corresponding to a resolution of 2.0×3.0×3.0 mm^3) is shown in Figure 6.6. Through the comparison, especially in the zoom-in regions, we can see some vein structures are lost in the low-resolution QSM maps due to partial volume effects, while these structures are nicely revealed in the high-resolution QSM maps produced by the proposed method.

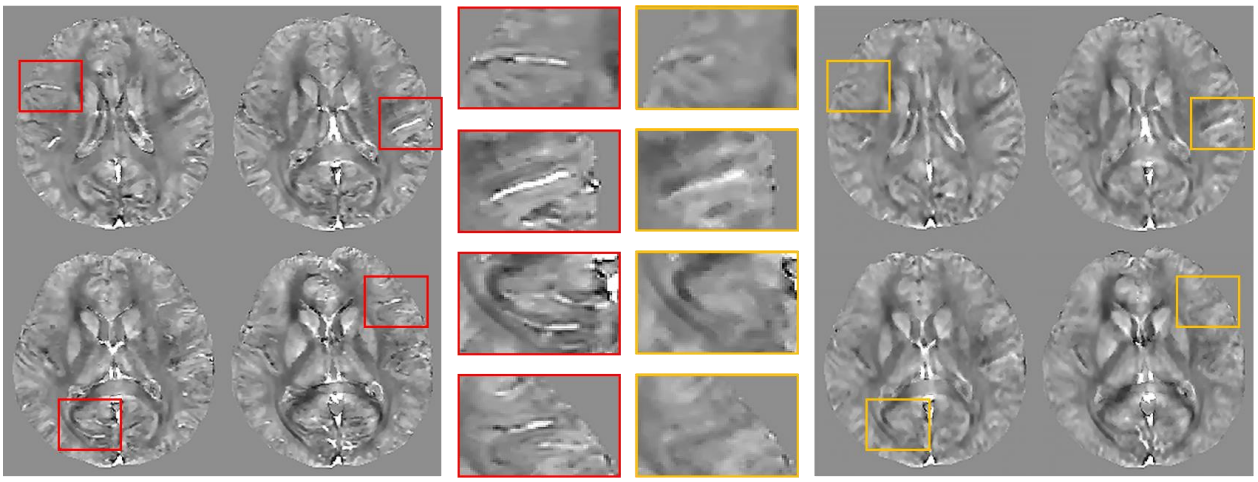

Figure 6.6: Comparison of QSM maps obtained from a healthy subject using (a) high-resolution SPICE (with the entire (k, t)-space, 2.0×1.0×1.0 mm^3); and (B) low-resolution SPICE (with only central (k, t)-space, 2.0×3.0×3.0 mm^3).

The high-resolution capability can not only provide nice structural imaging, but also improve the separation between metabolite signals and water/lipid signals. On the one hand, the lipid signals leaking from the subcutaneous layers into the brain would significantly reduce with higher

resolution. On the other hand, the signal distortion and cancellation due to field inhomogeneity and partial volume effects could also largely reduce. Figure 6.7 shows an illustration of these benefits of high resolution. In the water images at TE of 70 ms, we can see the signal dephasing near the frontal region is much severer in low-resolution than high-resolution SPICE data, and the signal distortion in the water spectra is also obviously reduced with high-resolution. Moreover, after removal of water signals, the high-resolution SPICE data has much less lipid contamination (orange spectra) and much less residual water signals (blue spectra). Higher resolution also benefits the correction of field effects for metabolite signals. With low-resolution SPICE data, only a low-resolution field map can be estimated and used for correction, while higher-resolution field correction becomes possible with high-resolution SPICE data. As shown in Figure 6.8, after field correction with high resolution, the cancellation and distortion of metabolite signals in the frontal region is significantly reduced, which greatly improves the quality of MRSI results.

Figure 6.9 shows a more complete set of results obtained by the proposed method, including water image, QSM map, T_2* map, myelin water imaging, NAA map, Cr map, Cho map, and Ins map. All these imaging modalities are acquired from a single 8-minute scan, with water signals at 2.0×1.0×1.0 mm^3 resolution and metabolite signals at 2.0×1.0×1.0 mm^3 resolution.

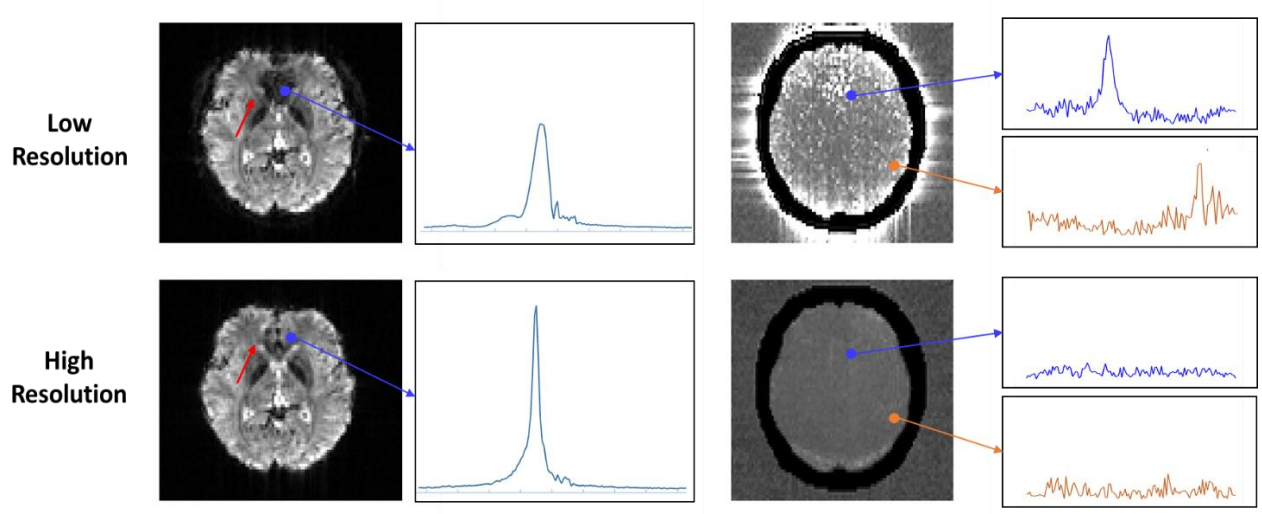

Figure 6.7: Comparison of the effects of different resolutions on MRSI data regarding to signal cancellation, lipid contamination and water removal. Both low resolution (2.0×3.0×3.0 mm^3) SPICE data and high resolution (2.0×1.0×1.0 mm^3) SPICE data, including water images at TE of 70 ms, water removed image, and their localized spectra are displayed.

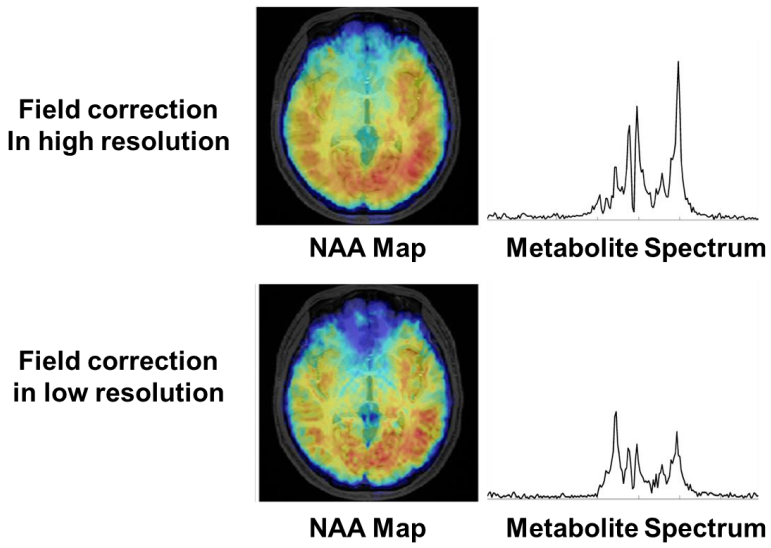

Figure 6.8: Comparison of NAA maps and metabolite spectra after correcting field effects using estimated field maps of different resolutions (low resolution is 2.0×3.0×3.0 mm^3 and high resolution is 2.0×1.0×1.0 mm^3).

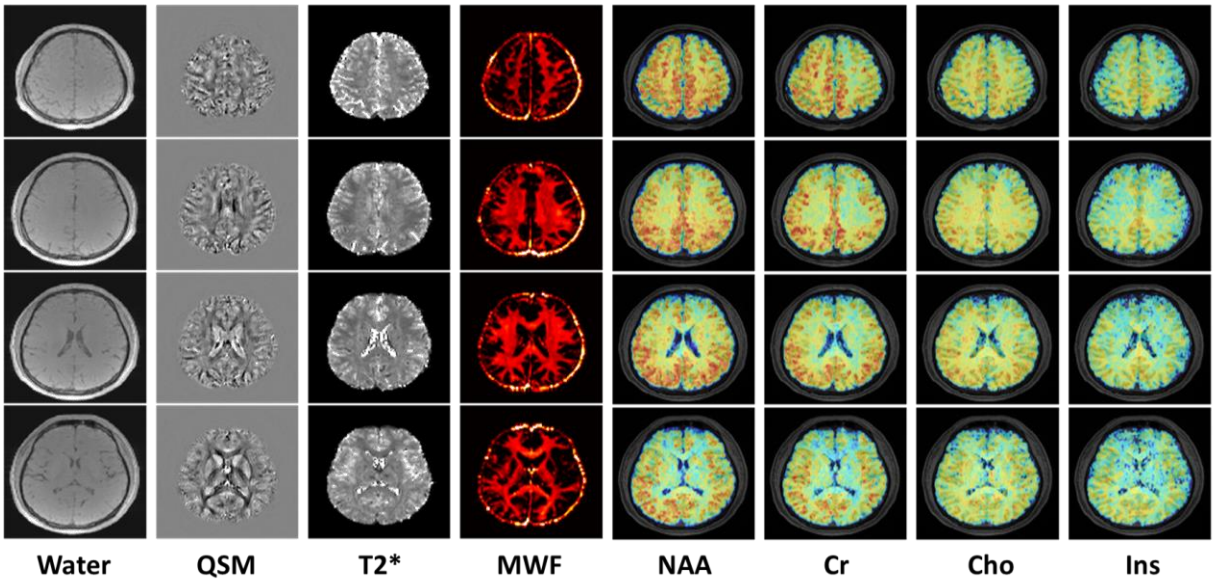

Figure 6.9: A representative set of results obtained from a healthy subject using the proposed method at 3T within an 8-minute scan time. The results include water image, QSM map, T2* map, myelin water faction at 2.0×1.0×1.0 mm^3, and NAA, Cr, Cho, and Ins maps at 2.0×1.0×1.0 mm^3.

A test-retest reproducibility study similar to the phantom experiments was carried out. The healthy volunteer was scanned twice within the same session, and the results from the two scans were compared. Figure 6.10 shows Bland-Altman plots of the resulting metabolite maps including NAA, Cr, Cho, and Ins. From the plots and the rates of outside points beyond two standard

deviations (4.9%, 5.5%, 5.3%, 5.7% for NAA, Cr, Cho, and Ins, respectively), we can see reproducibility of the proposed method in *in vivo* environment is still very reasonable.

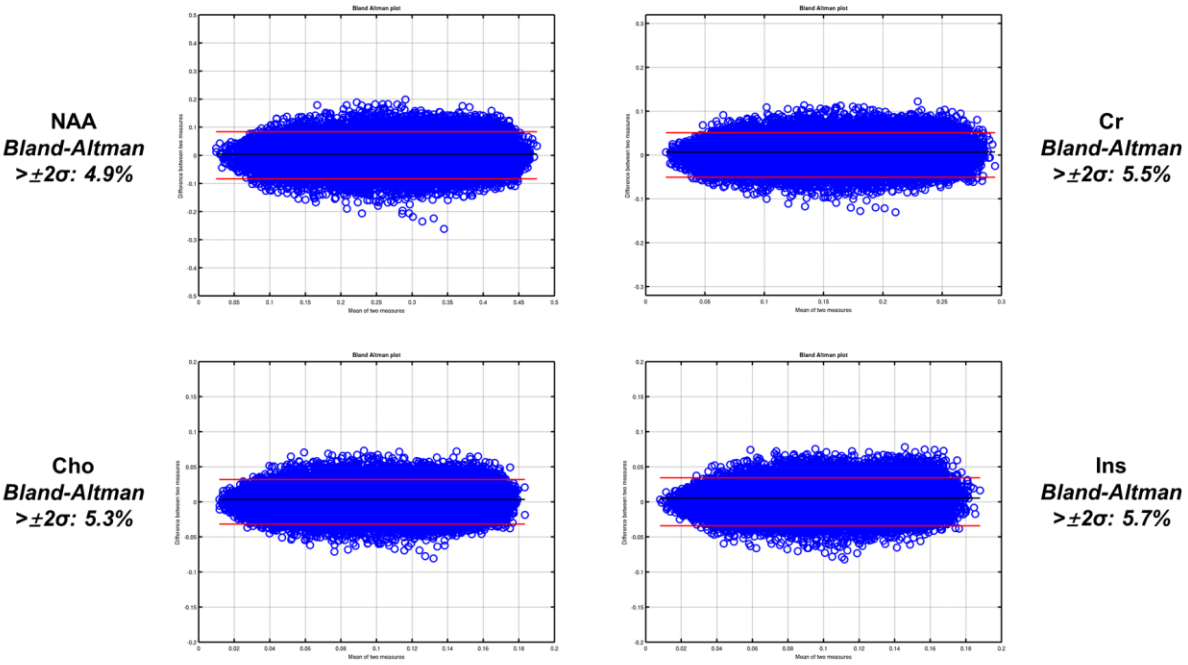

Figure 6.10: Bland-Altman plots of metabolites including NAA, Cr, Cho, and Ins, from a test-retest study scan.

6.3 Applications on Brain Tumor at 3T

Currently, the most widely used brain tumor imaging tool in clinical practice is MRI, which can provide high-resolution structural information. The structural information has very high sensitivity for neoplastic diseases, but does not have good specificity to distinguish tumors with other focal lesions or differentiate tumors of different grades and mutant phenotypes [68], [120]. The potential of noninvasive metabolic imaging for brain tumors has long been recognized by both imaging scientists and clinicians. Imaging metabolism of brain tumors is essential for its diagnosis, treatment planning, and therapy assessment, and in the past several decades, there have been numerous studies showing the unique values of brain metabolites including NAA, Cr, Cho, and Lac as biomarkers with good specificity for brain tumors [68], [94], [120]–[123]. However, the conventional MRSI methods are not able to provide sufficient spatial resolution, brain coverage,

imaging speed, and robustness, thus their clinical applications are rather limited. MRSI methods are still not widely accepted as a routine clinical tool for tumor imaging.

The imaging capability of the proposed method may overcome these technical obstacles and provide a unique opportunity for the applications of MRSI in brain tumor imaging. The three mm resolution of the proposed method may help in many aspects such as capturing small-size tumors and revealing intra-tumor metabolic heterogeneities. To demonstrate the potential of this method in brain tumor imaging, scans have been performed on patients with diagnosed tumors. All the scans were carried out on a 3T Siemens Skyra scanner (Siemens Healthineers, Erlangen, Germany), under approval of the Institutional Review Board of Shanghai Fifth People's Hospital, China. Written informed consents were obtained from all participants before the scans. The imaging protocol is the same as described in Section 3.4, but the MPRAGE scans were carried out after contrast agent (gadolinium diethylenetriaminepentaacetic acid) was intravenously administered for contrast enhancement.

Figure 6.11 compares the proposed high-resolution MRSI ($2.0\times3.0\times3.0$ mm^3) with a low-resolution MRSI of a practically used spatial resolution ($12\times12\times12$ mm^3). This low-resolution MRSI data was generated from the high-resolution data by k-space truncation. The patient was diagnosed with a small-size tumor, as indicated in the anatomical image (by a blue arrow). Using the proposed method, this small-size tumor can be observed on the Cho map very clearly, but it is not differentiable from surrounding tissues in the low-resolution MRSI due to strong partial volume effects. The spatially localized spectra also show the advantages of high-resolution MRSI. From the previous studies using single voxel spectroscopy or low-resolution CSI methods, it has been shown that the brain tumor typically shows reduced NAA and elevated Cho [68], [120]. In the spectra of high-resolution MRSI data, the NAA reduction and Cho increase in tumors are clearly revealed compared with the normal tissues. But in the low-resolution data, these spectral features are not as distinguishable from the normal issues as in the high-resolution data. This set of results show that the enhancement of resolution using the proposed method can enable improved detection of metabolic alterations in such small tumors.

High resolution MRSI also benefits imaging of large-size brain tumors, especially for high-grade tumors. High-grade brain tumors like glioblastomas usually have strong intra-tumoral heterogeneities; different regions of the lesion such as edema, enhancing ring and necrotic core are expected to have different pathological conditions thus different metabolic fingerprints. Figure

6.11 shows a set of results obtained from a tumor patient diagnosed with grade IV glioblastoma. Four representative localized spectra from enhancing ring, surrounding edema, necrotic core, and normal tissue are displayed, showing distinct metabolic features. Edema, enhancing ring and necrotic core all show reduction of NAA due to the loss of neurons; enhancing ring where has the highest possibility of proliferation show the highest Cho; necrotic core has destroyed cell environment, thus it shows reduction of all metabolites. From the metabolite maps, we can also observe these metabolic heterogeneities with different metabolites showing different spatial distributions. This set of results shows that the high resolution of the proposed method can reveal intra-tumoral metabolic heterogeneities, which would be very valuable in determining biopsy sites, tumoral boundaries, and tumor characteristics.

The proposed method is also applied to study the metabolic differences between tumors of different grades. A small cohort of patients with low-grade (WHO grade I, 4 patients) and high-grade tumors (WHO grade IV, 4 patients) were recruited in the study. A comparison of MRSI results is displayed in Figure 6.12, including representative anatomical imaging and Cho/NAA ratio maps, and quantitative Cho/NAA values in the tumor regions of these two groups. The tumor regions were determined by segmentation on the anatomical images including edema, and the normal tissues were selected as the contralateral tissues of lesions. From the Cho/NAA ratio maps, we can see that Cho/NAA ratios in the tumor lesions are higher than those in the normal tissues, and the ratios in high-grade tumors are higher than those in the low-grade tumors, which is consistent with previous studies in literature. In the statistical analysis of Cho/NAA values, we can see the significant differences of Cho/NAA values between high-grade tumors and low-grade tumors ($p<0.0001$) and between tumors and normal tissues ($p<0.0001$). This set of results shows the potential of the proposed method for noninvasive tumor grading, using the brain metabolites as biomarkers with good specificity. Further study may include more metabolites and imaging modalities from the companion water signals like QSM and T_2* in the analysis.

This imaging method has also been applied to monitor the longitudinal metabolic changes after treatment. Figure 6.14 shows the results obtained from a patient diagnosed with metastasis from lung cancer. Three scans using the proposed method were performed on this patient in two weeks, three months, and six months after the gamma knife therapy, respectively. From the Cho/NAA maps and quantitative values in the lesion area, we can clearly see the reduction of Cho/NAA along the time, which is considered being related to the regional remission and reduction of tumor

volume. This can be confirmed on the anatomical images and clinical scores. The positive responses of the patient to treatment were well-captured by the metabolic changes detected using the presented method.

These preliminary clinical results were obtained from a small cohort of patients, as a feasibility study. But these results have demonstrated the potential of our proposed method in capturing small brain tumors, imaging tumor heterogeneities, tumor characterization, and monitoring treatment responses. This could lay a foundation for further metabolic studies on brain tumors, providing more clinical insights. The results of this section have been published on IEEE-EMBS (Engineering in Medicine and Biology Society) conference in 2021 [94].

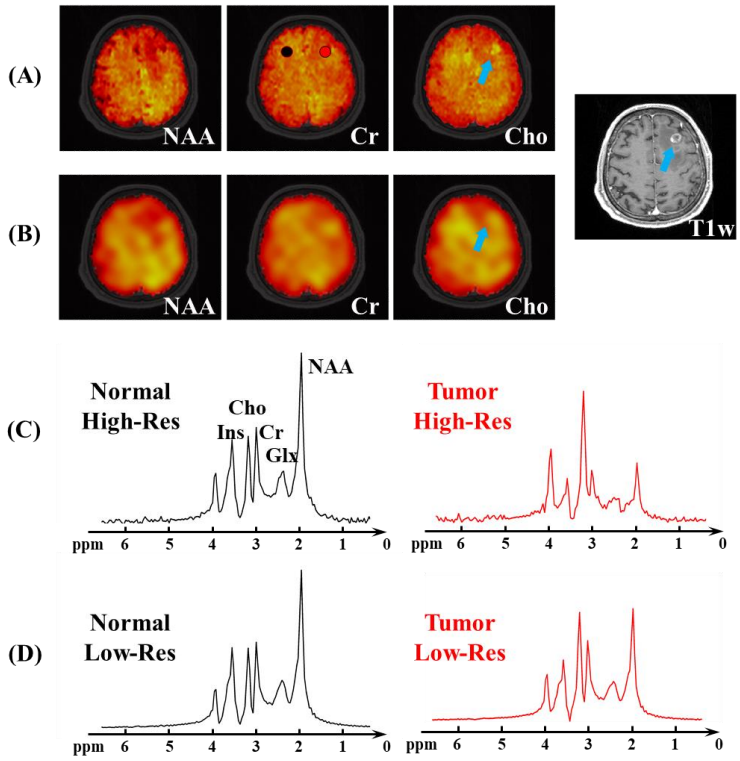

Figure 6.11: Results obtained from a brain tumor patient to show the high-resolution capability in capturing small tumors. (A) Metabolite maps from high-resolution data (2.0×3.0×3.0 mm^3). (B) Low-resolution metabolite maps (12×12×12 mm^3). (C) Spectra from normal tissue and tumor in the high-resolution data. (D) Spectra from the same points as in (C) but in low-resolution data.

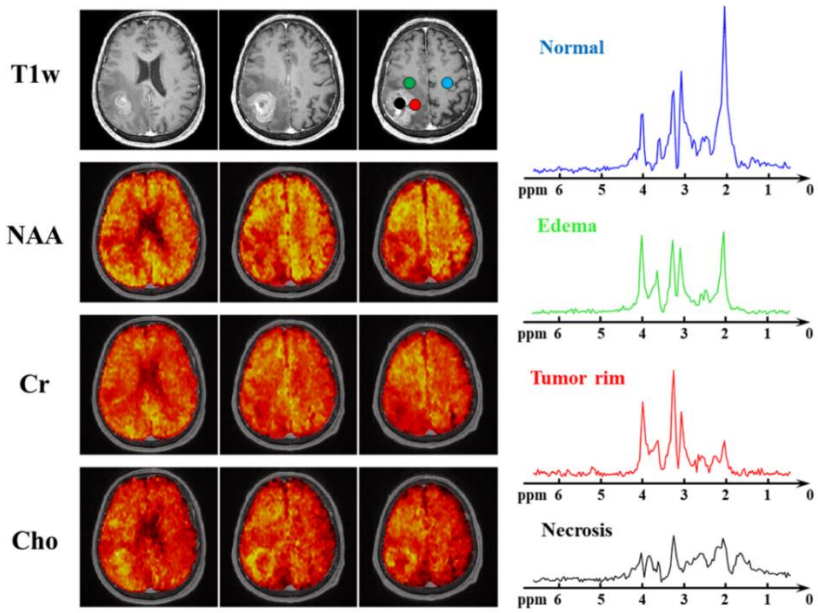

Figure 6.12: Representative results from a high-grade glioma patient to show high-resolution capability in revealing intra-tumoral heterogeneity. Metabolite maps including NAA, Cr, and Cho, and localized spectra from the normal tissue, edema, enhancing ring, and necrosis core are showed.

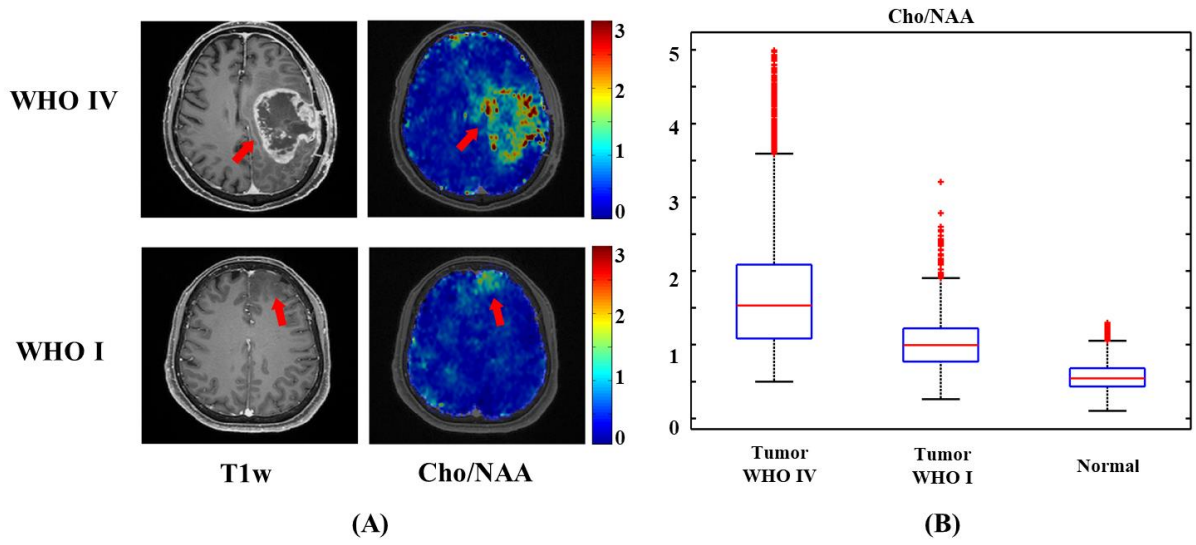

Figure 6.13: Comparison of Cho/NAA spatial maps and values between high-grade tumors (WHO IV, 4 patients) and low-grade tumors (WHO I, 4 patients). (A) Representative Cho/NAA maps. (B) Box plots of Cho/NAA values in the tumor lesions and the contralateral normal tissues. The central red mark is the median, the edges of the box are the 25th and 75th percentiles.

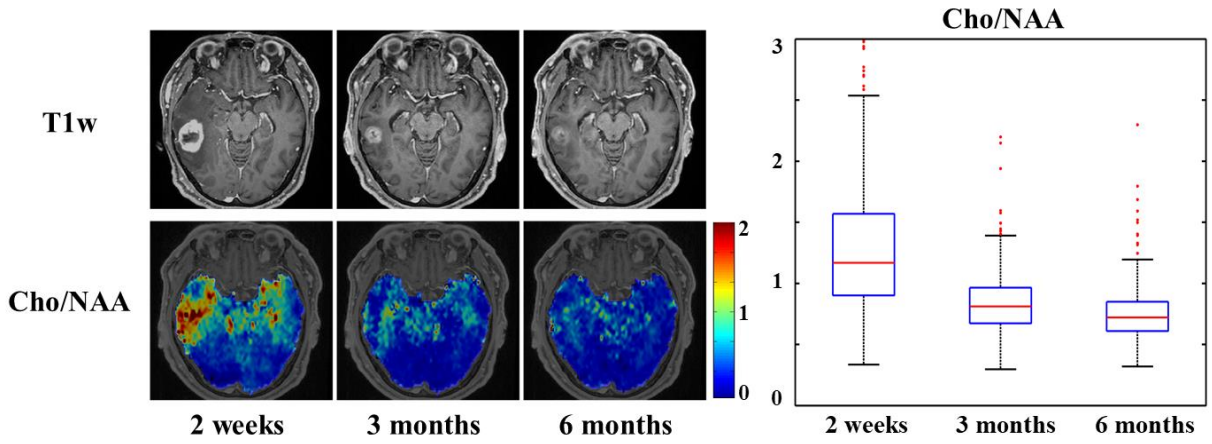

Figure 6.14: Longitudinal metabolic changes of a tumor patient diagnosed with metastasis from lung cancer. Three scans were performed in two weeks, three months, and six months after the gamma knife therapy. Cho/NAA ratio maps and the box plots of Cho/NAA values in tumor lesions are displayed. Recoveries of NAA and Cho along time have been observed along with the positive responses to treatment.

6.4 Phantom Experiments at 7T

The 7T phantom experiments were performed on a 7T Terra scanner (Siemens Healthcare, Erlangen, Germany) equipped with a 32-channel receiver coil. The same uniform sphere metabolite phantom as described in section 6.1 was used. The scan protocol for whole brain MRSI was described in section 4.3 (FOV = 240×240×150 mm^3, resolution of metabolites = 3.0×3.0×3.2 mm^3 (matrix size = 80×80×58), TR = 150 ms, TE = 1.6 ms, echo-space = 0.9 ms, echo number = 140×2, readout bandwidth = 167 kHz, flip angle = 26˚, scan time = 8 minutes).

Besides validating the proposed method and its performance, the phantom experiments at 7T were also used to demonstrate the correction of B_0/B_1 inhomogeneity and reconstruction of sparse data. Therefore, one set of data with fully sampled (k, t)-space was acquired using the proposed sequence at 7T. Scan parameters were the same as above, but no sparse sampling was applied, so total scan time was 17 min. Then retrospective under-sampling was performed to simulate the sparse data. For the sparse data, parallel imaging reconstruction was performed to interpolate the missing measurements. Then the remaining processing steps of both full data and sparse data were the same, including removal of water signals, reconstruction of metabolite signals, and correction of B_0/B_1 field inhomogeneity, as presented in Chapter 5.

Compared with the sequence at 3T, one critical point of the 7T sequence is utilization of sparse sampling even for metabolite signals to accelerate imaging speed. Therefore, good recovery of the sparse metabolite signals is important for the proposed method at 7T. As mentioned before, parallel imaging echo-by-echo without any additional constraints (such as subspace) was used to recover this part of under-sampling for metabolite signals, minimizing perturbation to temporal patterns. Figure 6.15 compares the phantom metabolite maps (including NAA, Cr, Cho and Glx) reconstructed from the fully sampled data and sparse data. The results from both data show good-quality and homogeneous spatial distribution in all four metabolite maps, without noticeable spatial aliasing artifacts. From the difference maps calculated as L_2-error between two maps, the differences between these two sets of results are less than 1%, which are acceptable in most of the practical applications.

Figure 6.16 shows a comparison of NAA maps from the metabolite phantom before and after B_0/B_1 field correction. We can see that, with a 150 mm spatial coverage in the slice direction, the proposed method was able to cover the whole phantom (150 mm diameter). Before correction of B_0/B_1 field inhomogeneity (in Figure 6.16(A)), there were obvious shading effects in the NAA map due to the strong B_1 inhomogeneity at 7T. In the localized spectra from two different locations, there were inconsistencies due to both B_0 and B_1 inhomogeneity, regarding to overall frequency shifts and signal magnitude differences. After B_0/B_1 field correction (in Figure 6.16(B)), the spatial distribution became much more homogeneous, and the localized spectra showed better agreement. It is known that the spectroscopy phantom has homogeneous concentration of metabolites, so the results show very good effectiveness of field correction, which is desired in MRSI data, especially at ultrahigh field.

This set of phantom results demonstrate the feasibility of the proposed method at 7T in *in vitro* experiments. In the acquisition aspect, whole brain coverage and fast imaging speed have been achieved, and in the processing aspect, success in field correction and recovery of sparse sampling in metabolite signals have also been shown.

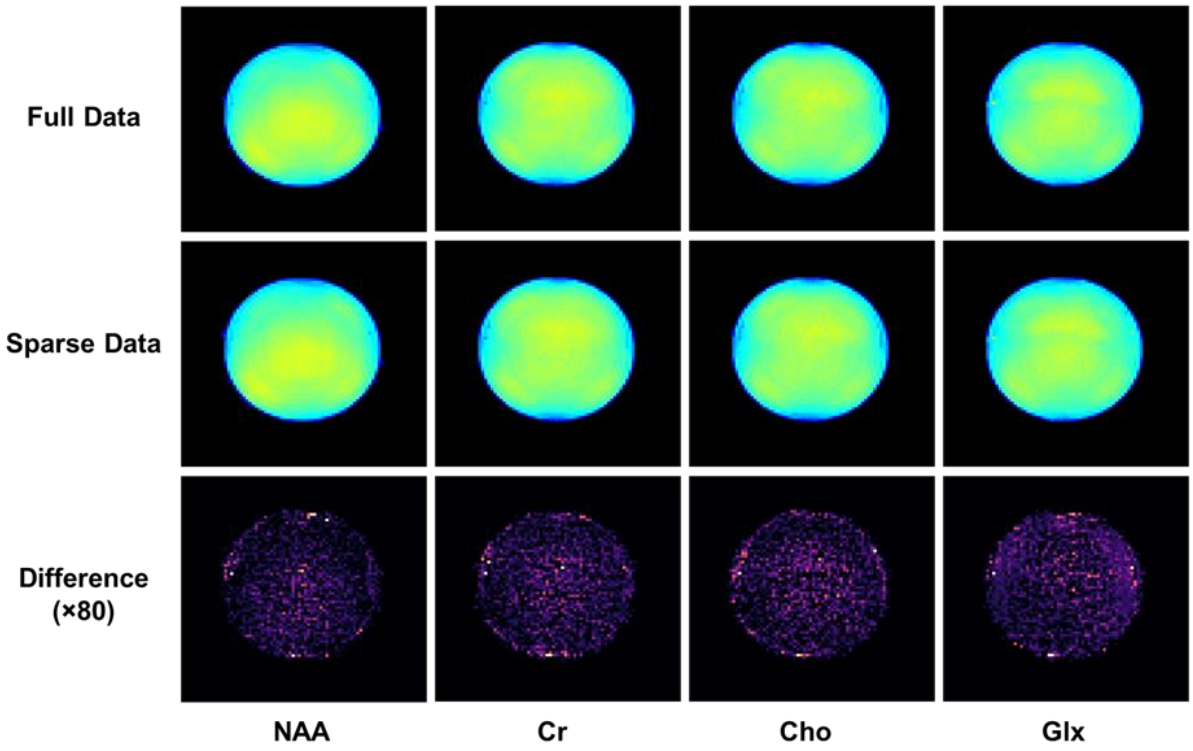

Figure 6.15: Comparison of phantom metabolite maps (including NAA, Cr, Cho, and Glx) obtained from fully sampled data and sparse data as the proposed method. Differences between the full data and sparse data are also displayed, within 1% of the metabolite maps.

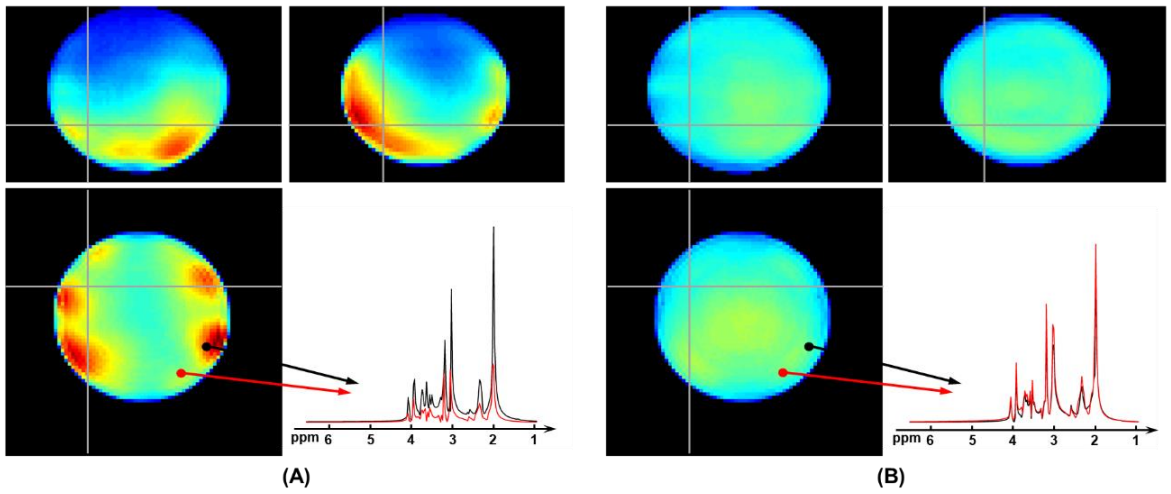

Figure 6.16: Comparison of phantom NAA maps before and after B_0/B_1 correction using the unsuppressed water signals. Spectra from two different locations are also displayed. After field correction, the spatial map shows improved homogeneity, and the localized spectra have better agreement.

6.5 In vivo Experiments at 7T

In vivo experiments at 7T were performed on healthy subjects on the same 7T Terra scanner (Siemens Healthcare, Erlangen, Germany) as 7T phantom scans. These scans were approved by the local Institutional Review Board. Written consent from the participants was collected from the participants before the scan. The scan protocol is described in section 4.3, including a Localizer scan, an MPRAGE scan, and a SPICE scan.

To compare performance of the sequences at 3T and 7T, one healthy volunteer was scanned at both 3T and 7T, using corresponding sequences with the same scan time around eight minutes. Figure 6.17 shows a comparison of spectra at 3T and 7T. Both data have been processed until the step before reconstruction of metabolite signals, including field correction, nuisance removal, coil combination, etc. Both sets of data were resized to resolutions of 1 cm for SNR consideration and spectra from one spatial voxel of each data were displayed for comparison. As observed, the spectrum of 7T data shows much improved SNR and separation between metabolite peaks, which matches expectation given the benefits of ultrahigh field. After metabolite reconstruction, the resulting metabolite maps of both 3T and 7T are shown in Figure 6.18, including NAA, Cr, Cho, and Glx. Both reconstruction of 3T and 7T data use similarly weak spatial regularization to illustrate comparison of data quality. We can see that the 7T metabolite maps have much reduced noise-induced fluctuations than 3T metabolite maps. The 7T metabolite maps also show noticeably better contrast between gray matter and white matter, especially for Cr map. This set of results has demonstrated the benefits of signal and contrast enhancement brought by ultrahigh field.

Figure 6.19 displays a representative set of results obtained from another healthy volunteer, including tri-planar views of whole-brain metabolite maps (NAA, Cr and Cho) and localized spectra from a region-of-interest. High-quality spatiospectral distributions of metabolites in the whole brain range were successfully obtained using the proposed method. We can see the whole brain metabolite maps match the anatomical structures reasonably well.

Since the proposed MRSI method does not suppress water signals, water imaging with various contrast can also be obtained. First, the anatomical images can be provided by the unsuppressed water signals. From the magnitude decay of water spectroscopic signals, T_2* map can be derived through direct exponential fitting. From the phase evolution of water spectroscopic signals, QSM can be generated through a standard QSM pipeline. These images from water signals (including anatomical image, QSM, and T_2*, at $2.0\times2.0\times3.2$ mm^3 resolution) and metabolite maps (including

NAA, Cr, and Cho maps at 3.0×3.0×3.2 mm^3 resolution) are simultaneously obtained from the single scan and displayed in Figure 6.20. This multi-model imaging capability of the proposed method may provide a valuable tool in practical applications.

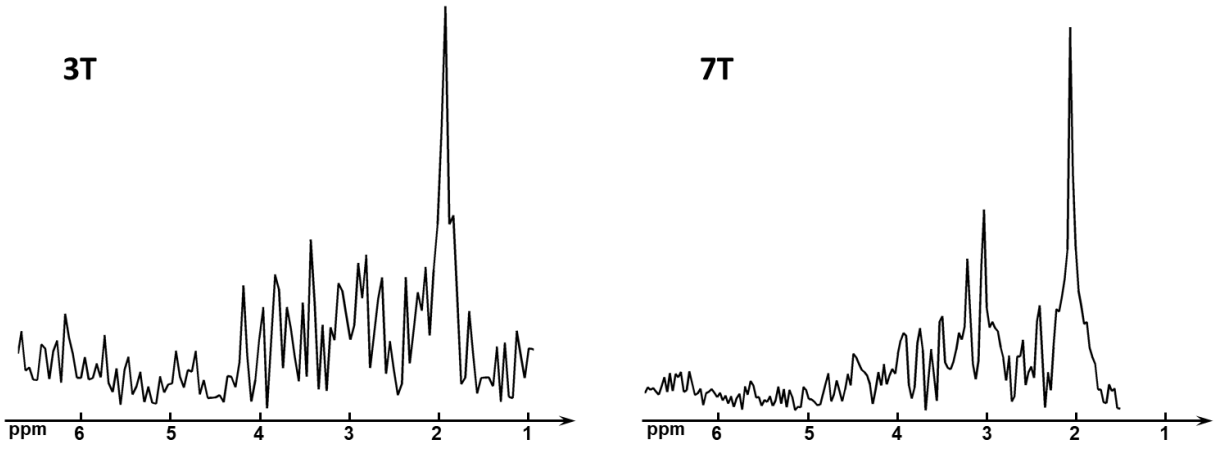

Figure 6.17: Comparison of localized spectra using the proposed sequences at 3T and 7T. Both displayed data are truncated to around 1 cm resolution and have not been reconstructed using subspace.

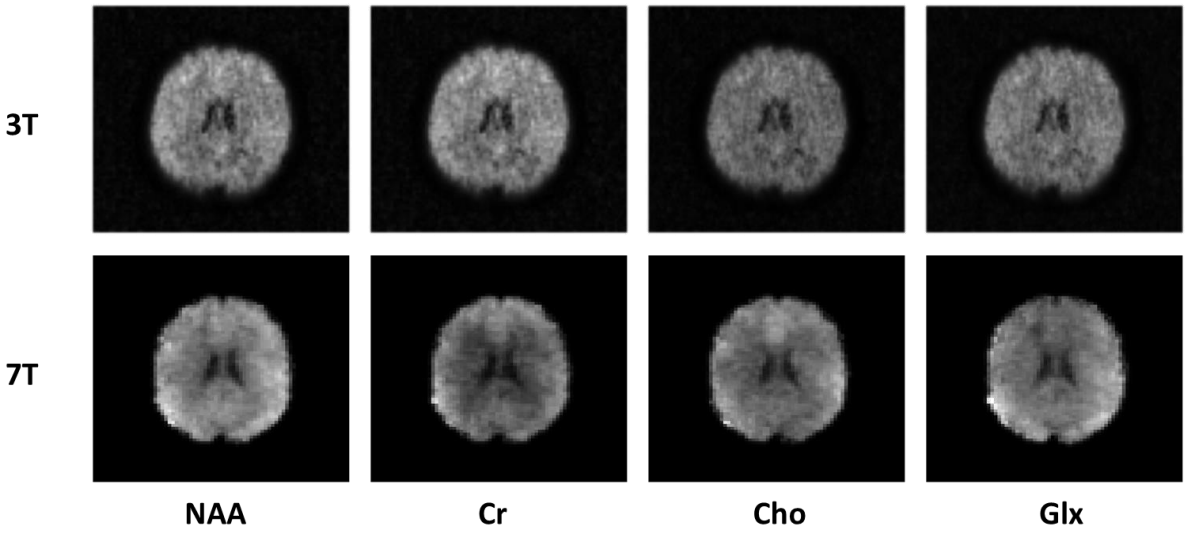

Figure 6.18: Comparison of reconstructed metabolite maps from 3T and 7T. Both data were acquired on the same subject within similar scan times around eight minutes.

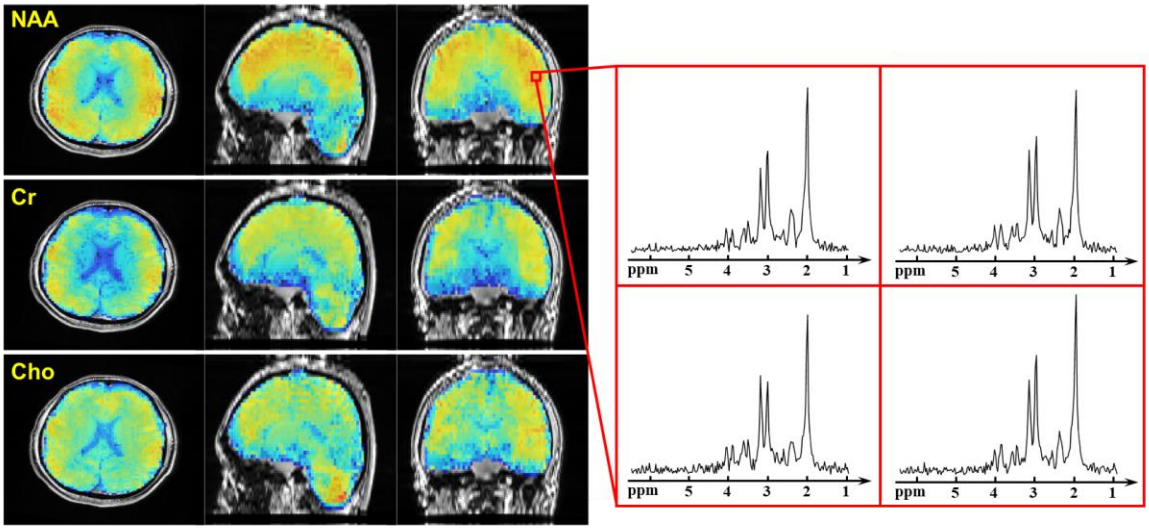

Figure 6.19: Tri-planar views of the whole brain metabolite maps (NAA, Cr, and Cho) and localized spectra. High quality spatiospectral distribution at high resolution (3.0×3.0×3.2 mm^3 resolution) was obtained in an 8-minute scan.

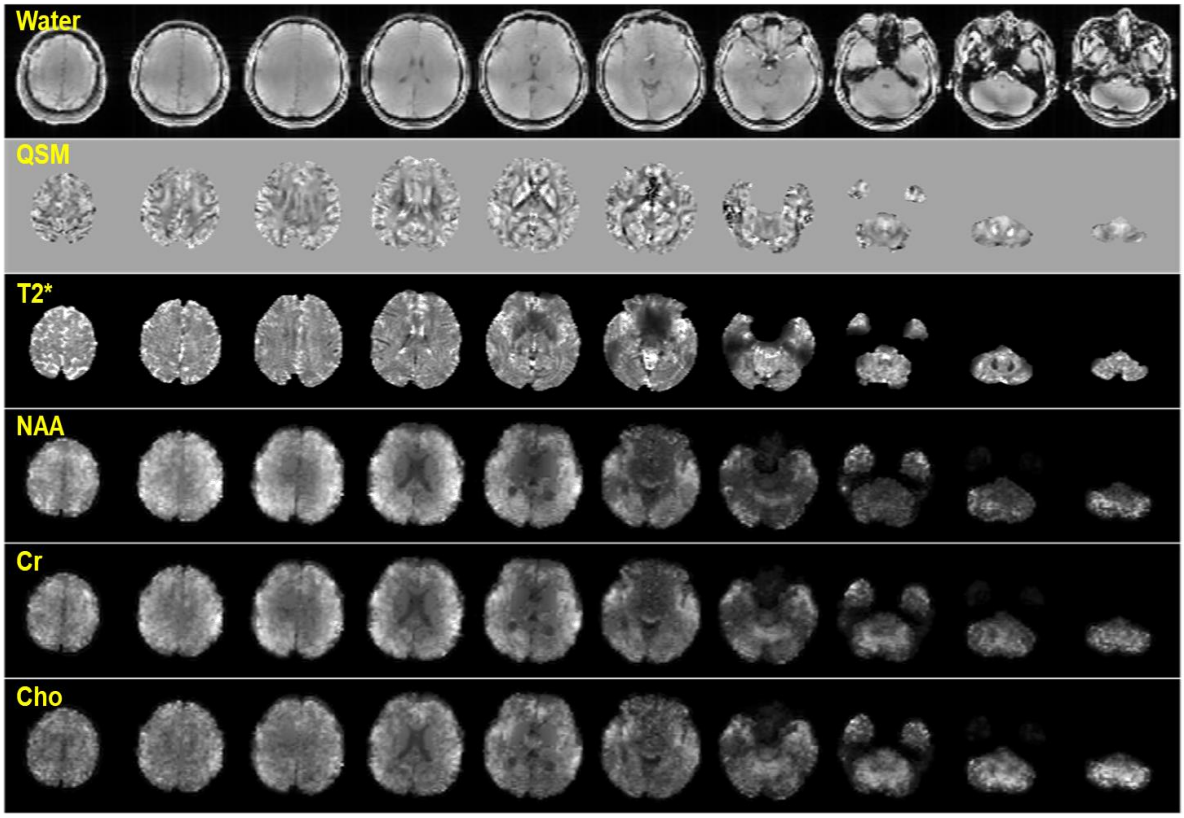

Figure 6.20: Simultaneously obtained whole brain water imaging (water image, QSM, and T_2*) at 2.0×2.0×3.2 mm^3 resolution and metabolic imaging (NAA, Cr, and Cho maps) at 3.0×3.0×3.2 mm^3 resolution in a single 8-minute scan.

The reproducibility of the SPICE sequence at 7T was also evaluated. A set of test-retest scans were performed on the healthy subjects. There were four scans for each subject, two sequential scans were performed within the same session while the other two scans were performed in one session of the other day. Figure 6.21 shows some representative test-retest metabolite maps from the four scans on the same subject. There metabolite maps were registered together for display and quantitative analysis. We can see reasonably reproducible metabolite maps were successfully obtained among different scans and different sessions. The corresponding R^2-plots and correlations were displayed in Figure 6.22. For inner session scans, the Pearson's correlation coefficients for NAA, Cr, and Cho are 0.8535, 0.8162, and 0.7031, respectively; for inter session scans, these Pearson's correlation coefficients of metabolites are 0.8388, 0.8063, and 0.6993, which are very close to, but slightly lower than, those of inner-session scans.

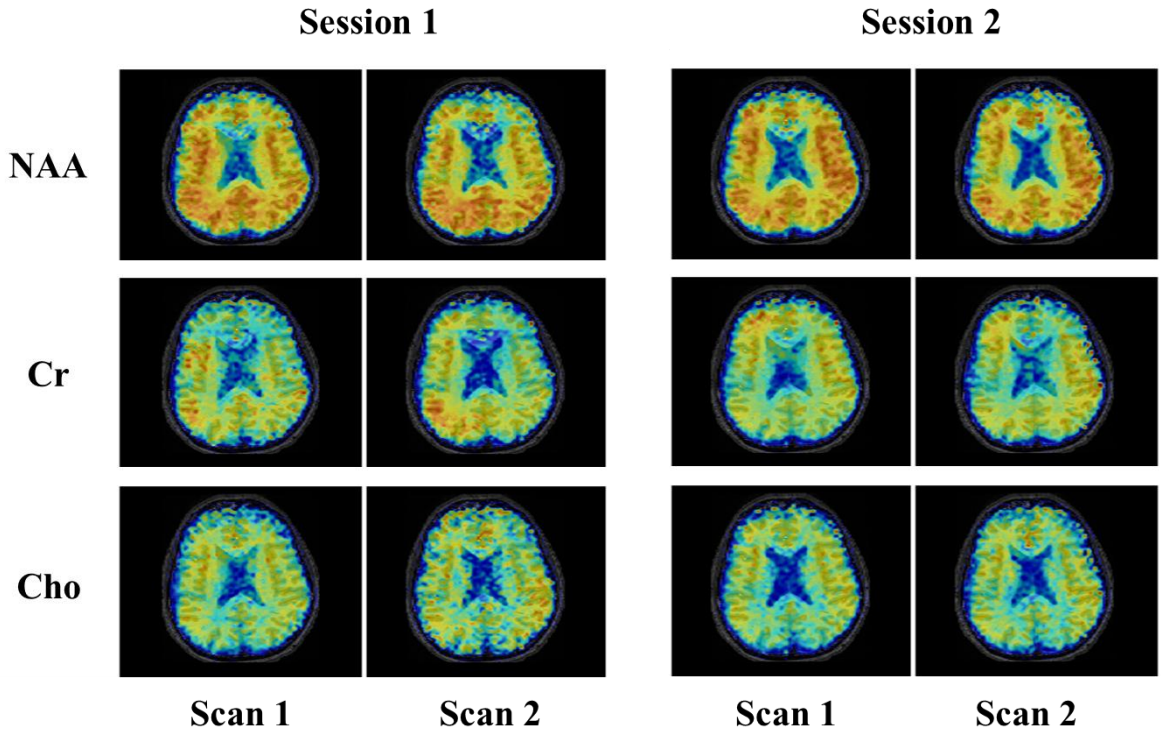

Figure 6.21: *In vivo* metabolite maps (including NAA, Cr, and Cho) from test-retest scans at 7T. four scans were performed on the same subject. Two sequential scans were performed within the same session while the other two scans were performed in one session of the other day.

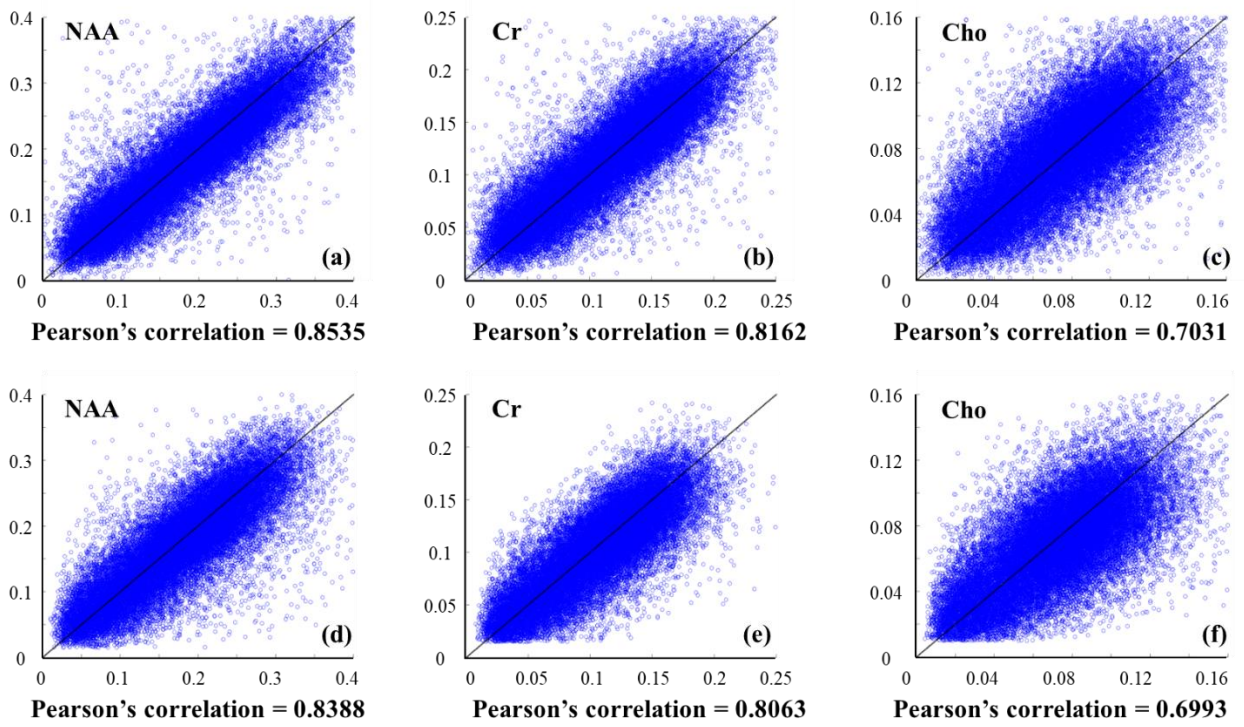

Figure 6.22: R^2-plots of in vivo metabolite maps in test-retest SPICE scans, as shown in Figure 6.21. (a-c) are plots of metabolite maps of scans within the same session; (d-f) are plots of metabolite maps of scans from different sessions. Identical lines are shown in black. Pearson correlation coefficients are also computed and displayed.

6.6 Summary

Both phantom and in vivo studies have been carried out to demonstrate the feasibility and to evaluate the performance of the proposed method. The preliminary results show that the proposed method can provide high-quality, high-resolution metabolite maps as well as high-resolution water imaging at both 3T and 7T. The applications in tumor imaging shows great potential values of the proposed method in clinical environments. The 7T results demonstrate the benefits of ultrahigh field, and its signal enhancement enables whole brain coverage and higher SNR.

CHAPTER 7 – HIGH-RESOLUTION ^{31}P-MRSI AT 7T

Besides ^{1}H-MRSI, ^{31}P-MRSI is also a promising metabolic imaging technique for the brain, whose great potential in probing energy metabolism has long been recognized. However, traditional ^{31}P-MRSI techniques for the brain are largely limited in resolution and imaging speed given the extremely low concentrations of phosphorus metabolites. This section introduces the work integrating both ultrahigh field and subspace modeling for 3D high-resolution ^{31}P-MRSI.

7.1 Challenges of ^{31}P-MRSI

As introduced in section 2.1, brain ^{31}P-MRS/MRSI techniques are able to detect a bunch of resonances of high-energy metabolites and membrane phospholipids, such as PCr, ATP, Pi, NAD, PC, PE, GPC, GPE, etc. These metabolites are unique probes in evaluation of many aspects of biology processes, including ATP synthesis and consumption, oxidative phosphorylation, composition of cell membranes, and tissue pH distribution and changes. Since many diseases and disorders are related to imbalance of energy metabolism, ^{31}P-MRSI methods have been employed in investigation of a range of diseases, like cancer, stroke, multiple sclerosis, and epilepsy [72]–[74]. However, ^{31}P-MRSI methods are rarely used in a clinical setting, caused by several technical impediments imposed by the low sensitivity and low concentration of phosphate metabolites. Given the natural signal intensity of phosphate metabolites, ^{31}P-MRSI methods are limited to low resolution, small brain coverage, and prohibitory long scan time, which are even more challenging than ^{1}H-MRSI.

First, the gyromagnetic ratio of ^{31}P is 17.2 MHz/T, which is about one third of ^{1}H (42.6 MHz/T). This low gyromagnetic ratio causes very low bulk magnetization of ^{31}P, about 1/10 of ^{1}H, according to Equation (2.3). This difference in gyromagnetic ratio also leads a different resonance frequency as ^{1}H, so a separate, specially designed RF coil is needed for excitation and acquisition. This additional request on hardware also limits its practical utility in some level. Second, the concentrations of ^{31}P metabolites are very low in the brain. The concentrations of most ^{31}P metabolites are on the order of mM, metabolites like NAD have even lower concentrations (as shown in Table 7.1). These low concentrations lead to very limited sensitivity for these metabolites. Third, the frequencies of ^{31}P metabolites are widely spread, covering a range of more than 20 ppm. On the one hand, the spectral peaks of metabolites are well separated, so the

quantification of metabolites is much easier compared with the crowded ^{1}H MR spectrum. But on the other hand, RF pulses with adequate excitation bandwidth is needed, and a large sampling bandwidth is also required to avoid spectral aliasing, based on the Nyquist sampling theorem. In addition, large sampling bandwidth imposes challenges to the use of fast spatiotemporal trajectories as introduced in section 2.3.

Metabolite	Chemical shift (ppm)	Concentration (mM)
PCr	0	4.37 ± 0.39
γ-ATP	-2.52	[3.0]
α-ATP	-7.56	3.09 ± 0.23
β-ATP	-16.15	2.82 ± 0.25
NAD	-8.21	0.28 ± 0.13
UDPG	-9.72	0.08 ± 0.04
PE	6.76	2.27 ± 0.16
PC	6.24	0.30 ± 0.12
Pi (ex)	5.24	0.30 ± 0.09
Pi (in)	4.82	0.85 ± 0.11
GPE	3.50	0.80 ± 0.18
GPC	2.95	1.32 ± 0.18

Table 7.1: Concentrations of typically detectable ^{31}P metabolites in the brain. The values are obtained from [124].

Given the low SNR nature of ^{31}P MR signals, many studies use single voxel ^{31}P-MRS, or single slice ^{31}P-MRSI with very low resolution, which suffer from strong partial volume effects and lack the capability to resolve metabolic heterogeneity of the tissue. To achieve large brain coverage or high spatial resolution, the scan time will become unacceptably long. For example, a 3D ^{31}P-MRSI study with a spatial resolution around one cm could easily take more than one hour, which is far from clinically feasible.

7.2 Data Acquisition and Image Reconstruction

As discussed in the last section, to achieve 3D high-resolution ^{31}P-MRSI within a reasonable scan time, the fundamental challenge is the SNR issue. To address this challenge, we propose a ^{31}P-MRSI method synergistically integrating ultrahigh field, SNR-efficient acquisition sequence, and subspace modeling for 3D high-resolution ^{31}P-MRSI (at 7T).

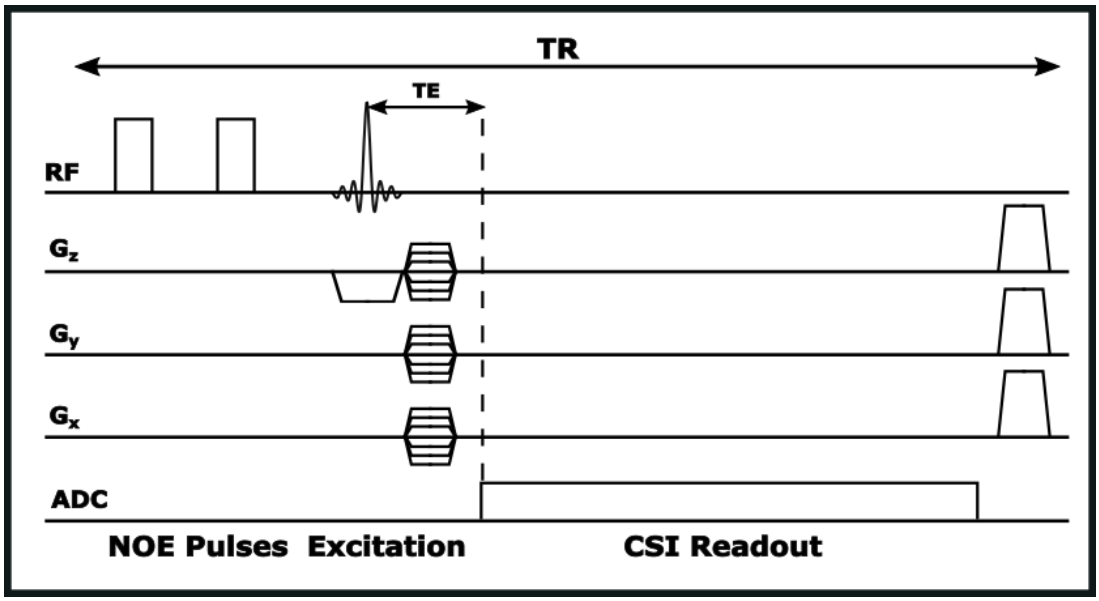

Figure 7.1: Pulse sequence diagram of the data acquisition sequence for 31P-MRSI at 7T. The sequence is based on FID-CSI sequence, integrated with NOE pulses to enhance SNR and optimized parameters such as short TR (200 ms), ultrashort TE (1.0 ms), and width bandwidth of excitation pulses.

In data acquisition, a basic FID-based CSI sequence is used, as shown in Figure 7.1. The selection of this FID-CSI sequence is based on several considerations. First, the SNR of ^{31}P metabolite signals is still very low even on the 7T scanners. The use of fast trajectories like EPSI or spiral trajectories for acceleration or higher resolution would further sacrifice SNR, which is not desirable in this SNR-limited scenario. Second, given the large bandwidth of ^{31}P spectrum, spatiotemporal trajectories would face the trade-off between sampling bandwidth and spatial resolution, but CSI sequence can guarantee enough acquisition bandwidth as wanted. Third, some important ^{31}P metabolites have very short T_2 values, especially ATPs and NAD have T_2 values around 15 ms. So, an FID acquisition with short TE is preferred for preserving SNR of these metabolites.

The CSI sequence at 7T is optimized with several specifics. First, the RF excitation pulse is a SINC-based pulse with a wide bandwidth (around 10 kHz) to reduce chemical shift displacement error. Furthermore, the used SINC pulse is weighted by a hamming window to improve slice profile (reduce Gibbs ringing). Second, a minimum TE as 1.0 ms is used to maximize SNR and preserve short T_2 metabolites. Third, TR value is selected as 200 ms, which is the minimum TR to cover enough temporal encodings. Similar to the discussion in section 3.1.2, the SNR efficiency

does not very much in the short TR range. Fourth, a weighted k-space sampling scheme is used. This means that the k-space locations closer to the k-space center have a greater number of averages. This provides good SNR efficiency and spatial response functions. Fifth, an NOE (Nuclear Overhauser Effects) module is added in the sequence to enhance SNR of ^{31}P metabolites [125]. The NOE module saturates the proton spins near ^{31}P nuclei using low-power RF pulses (4 sequential rectangular pulses in each TR in our implementation) at water frequency before acquisition of ^{31}P signals. Through dipolar interactions between ^{31}P and ^{1}H, the saturated water protons can enhance the magnetization of ^{31}P metabolites.

Compared with ^{1}H-MRSI described in previous chapters, the processing of ^{31}P-MRSI data is relatively more straightforward since it does not have sparse sampling and nuisance signals. Therefore, the major processing task is on signal denoising, which can be addressed using the learned subspace model as used for ^{1}H-MRSI reconstruction. So the reconstruction procedure includes subspace learning and constrained reconstruction.

In the subspace learning, a simplified spectral formulation is used, discarding the term of compensation function in Eq (5.2):

$$s_n(t) = \varphi_n(t) e^{-t/T_{2,n} + i2\pi f_n t} \tag{7.1}$$

where $\varphi_n(t)$ represents the resonance frequency structure of a specific ^{31}P metabolite; $T_{2,n}$ the T_2 relaxation time and f_n the frequency shift. The physical basis function $\varphi_n(t)$ can be generated from quantum mechanical simulation as ^{1}H-MRSI. For in vivo experiments, where the broadened linewidth would cover J-splitting and result in single spectral peak for each metabolite, $\varphi_n(t)$ can also be generated as a single Lorentzian function with known frequency shift. Discarding of the compensation function may cause model error, so a preliminary field correction step is performed as a pre-processing step before reconstruction or spectral fitting. More specifically, given the low SNR of ^{31}P-MRSI data, a Hamming window is applied in k-space to gain SNR, then the frequency shifts of PCr peak (as referred to 0 ppm) are estimated as the field map for correction. This field correction only corrects the inter-voxel field inhomogeneity but not intra-voxel field inhomogeneity. Then the estimation of spectral parameters $T_{2,n}$ and f_n can be done by fitting to Equation (7.1), using the time-domain fitting method as in ^{1}H-MRSI [115]. Then the remaining steps follow the subspace learning for ^{1}H-MRSI, including re-generation of spectral signals using

Equation (7.1), arrangement of spectral signals into a Casorati matrix, and generation of basis function using SVD.

Training data was collected using the CSI sequence as described above. Normally the training data has smaller resolution while higher SNR than the typical imaging data; given the long scan time of ^{31}P-MRSI experiments, we directly use the imaging data for subspace learning without acquiring additional training data.

With the pre-determined spectral basis functions (the matrix form is denoted as V_p), the reconstruction or denoising task can be done by subspace modeling incorporating anatomical constraints as the ^{1}H-SPICE method. The formulation is similar to Equation (5.7) as solving the optimization problem:

$$\widehat{\mathrm{U}}_p = \arg\min_{\mathrm{U}_p} \left\| s_p - \mathrm{U}_p \mathrm{V}_p \right\|_2^2 + \lambda_p \left\| D\mathrm{U}_p \right\|_2^2 \tag{7.2}$$

where s_p is vector form of the noisy ^{31}P-MRSI data in spatiotemporal domain, after Fourier reconstruction from (k, t)-space data. U_m represents matrix form of spatial coefficients, D the edge-weighted total variation operator and λ_p the regularization parameter. The edge weighting for regularization is estimated from a ^{1}H anatomical images acquired with the ^{31}P-MRSI scan. After getting $\widehat{\mathrm{U}}_p$, the reconstructed spatiotemporal function can be generated as $\rho_p = \widehat{\mathrm{U}}_p \mathrm{V}_p$.

After reconstruction, spectral quantification of metabolites is performed using a subspace-based fitting method [32]. For absolute quantification, γ-ATP is used as internal reference since it is widely regarded as three mM concentration in a normal human brain. Then the concentration of other metabolites is calculated based on the following formula:

$$C_p = \frac{1}{P_p} C_{\gamma ATP} \frac{E_{\gamma ATP}}{E_p} \frac{S_p}{S_{\gamma ATP}} \tag{7.3}$$

where C_p, E_p, S_p, and P_p are concentration, T_1 factor, signal intensity (area under the spectrum), and contained number of ^{31}P of a specific metabolite, respectively. The T_1 factor is computed as follows:

$$E = \frac{\left(1 - e^{-TR/T_1}\right) \sin\alpha}{1 - \cos\alpha \, e^{-TR/T_1}} \tag{7.4}$$

where α and TR are flip angle and TR of the sequence, respectively. T_1 values of metabolites are obtained from literature reported values [126].

7.3 Experimental Results

The ^{31}P-MRSI experiments were performed on a 7T MR scanner (Siemens Healthcare, Erlangen, Germany) equipped with a single channel, dual-channel ^{31}P-^{1}H quadrature TEM head volume coil. Experiments were performed on both phantom and healthy subjects. The phantom is a home-made bottle phantom filled with water-based liquid and ATP of 10 mM concentration. The *in vivo* experiments were performed under the approval of the Institutional Review Board of University of Minnesota, and written informed consent was obtained before the scans. The sequence protocols slightly vary between scans. One typical set of CSI parameters for *in vivo* scan are as follows: FOV = 220×220×100 mm^3, matrix size = 24×24×8; resolution = 9.1×9.1×12 mm^3, TR = 200 ms, TE = 1.2 ms, bandwidth = 5000 Hz, vector size = 1024, average (k-space weighted) = 12, flip angle = 30˚, scan time = 15 minutes. The slight modifications based on this protocol will be specially discussed below.

In phantom experiments, the only difference in scan protocol compared with the protocol mentioned above was fewer number of averages. Only six averages were acquired for phantom experiments, resulting in a scan time of 9:45 minutes. Figure 7.2 shows a set of such phantom results to illustrate the denoising performance of the proposed method. The spatial distributions of three ATPs (including γ-ATP, α-ATP, and β-ATP) and spectra from a selected spatial location are displayed. Both metabolite maps and spectra show that the ^{31}P-SPICE method could largely reduce the measurement noise and produce high-quality results.

Figure 7.3 shows a set of representative *in vivo* results (using the same 15-minute scan protocol as mentioned above). From the spectra from a selected spatial point within the brain, we could see that the original ^{31}P-MRSI are very noisy, with only the peak of PCr (which has the highest concentration) visible. Signals of other metabolites like ATPs were buried under the large measurement noise. After SPICE reconstruction, signals of these metabolites became much more visible. The improvement is also obvious in the resulting metabolite maps (including PCr, γ-ATP, and α-ATP). This shows that the proposed method is able to obtain reasonable 3D ^{31}P metabolite maps at a nominal resolution of 9.1×9.1×12 mm^3 in a 15-minute scan.

One important question ^{31}P-MRSI is used to study is the metabolite contrast between gray matter and white matter. The contrast of ^{31}P metabolites is difficult to be directly investigated using single voxel ^{31}P-MRS and typical low-resolution ^{31}P-MRSI methods. In this work, the metabolite contrast is evaluated using the ^{31}P-SPICE method. To gain enough SNR for the analysis, the proposed sequence was repeated twice in data acquisition, taking a total 30-minute scan time. Figure 7.4 shows the metabolite maps including PCr, γ-ATP, α-ATP, GPC, and PE obtained in the scan. A T_1-weighted images acquired in the same scan and the derived masks of tissues (including gray matter, white matter, and CSF) are also displayed as reference. High-quality spatial maps of these metabolites were successfully obtained. Comparing with the proton images, we could qualitatively see some level of contrast in these metabolite maps. Figure 7.5 shows the quantitative comparison of metabolite concentrations between gray matter and white matter. Based on the box plots, the concentrations of γ-ATP and α-ATP were quite uniform between gray matter and white matter, the concentration of PCr in gray matter was higher than that of white matter, while white matter has a higher concentration of GPC than gray matter. These observations match the previous studies in literature [127]. This indicates that the resolution of the proposed method might have the capacity to address partial volume effect and resolve the metabolite difference between gray matter and white matter.

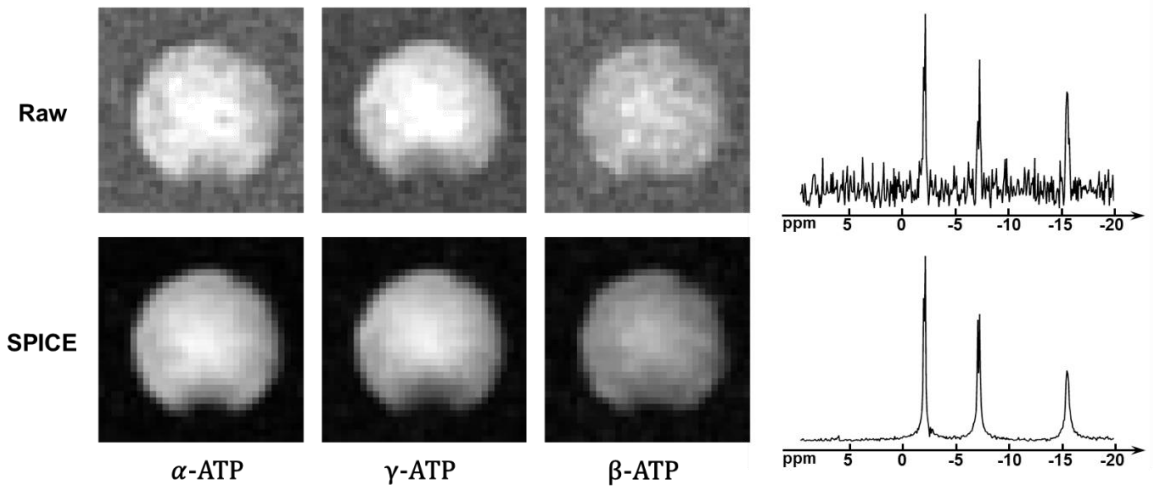

Figure 7.2: Representative ^{31}P-MRSI results obtained from an ATP phantom before and after denoising using SPICE.

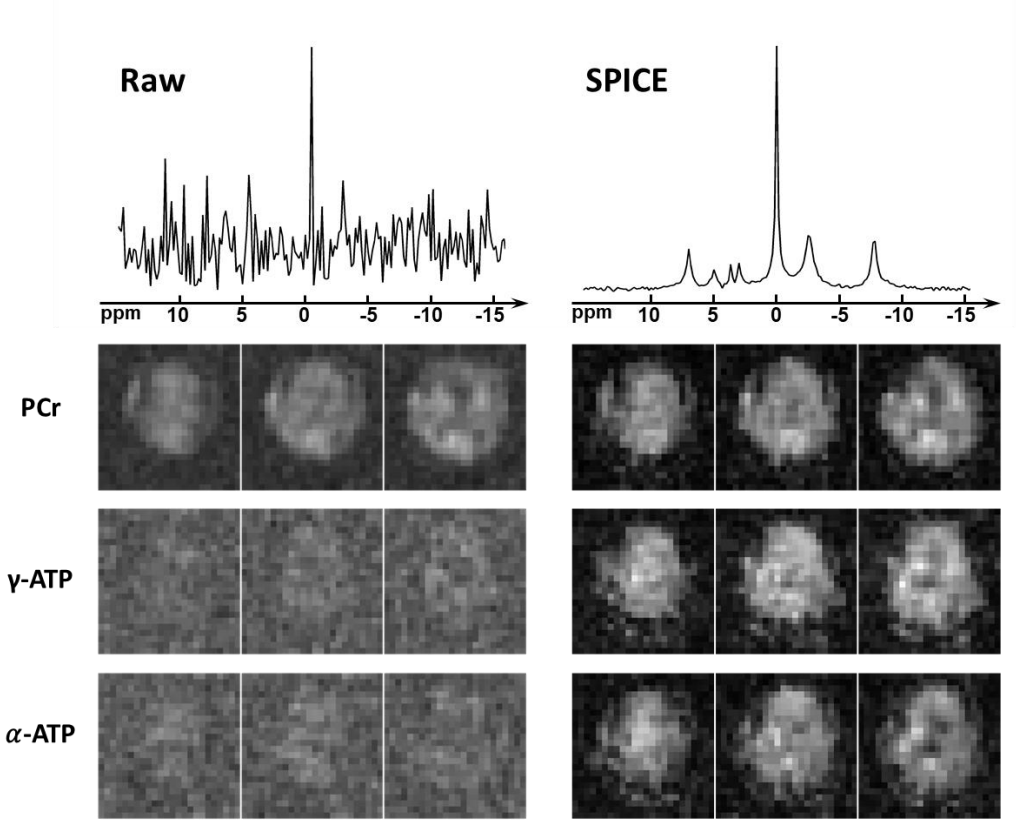

Figure 7.3: Representative ^{31}P-MRSI results obtained from a healthy subject before and after SPICE reconstruction, including localized spectra and metabolite maps.

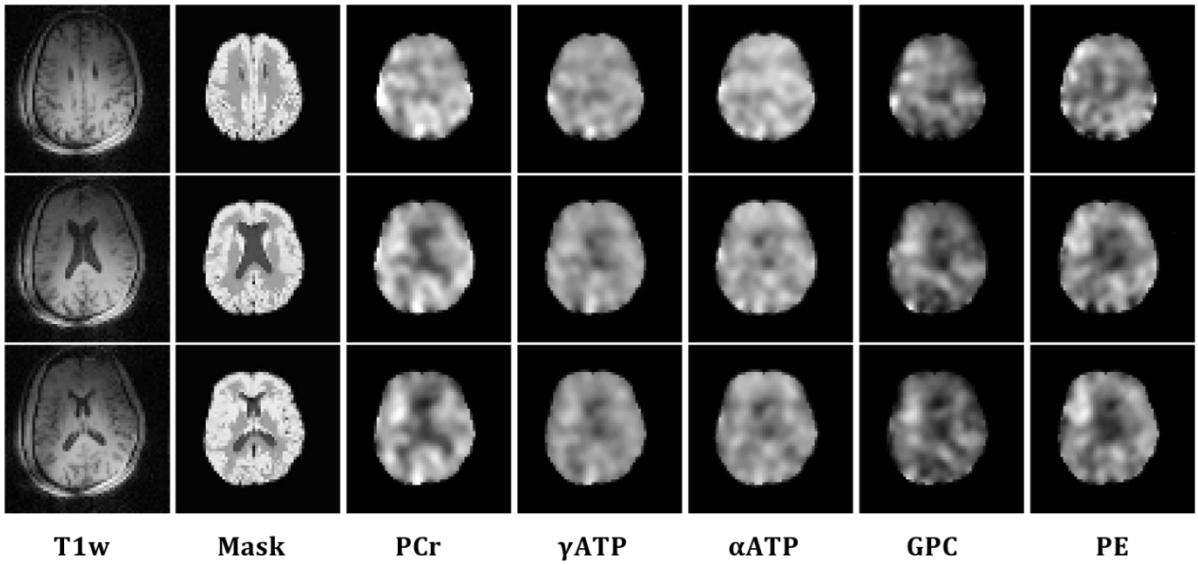

Figure 7.4: Metabolite maps obtained from a healthy subject in a 30-minute scan for metabolite contrast analysis. T_1-weighted images, masks of tissues, and metabolite maps are shown.

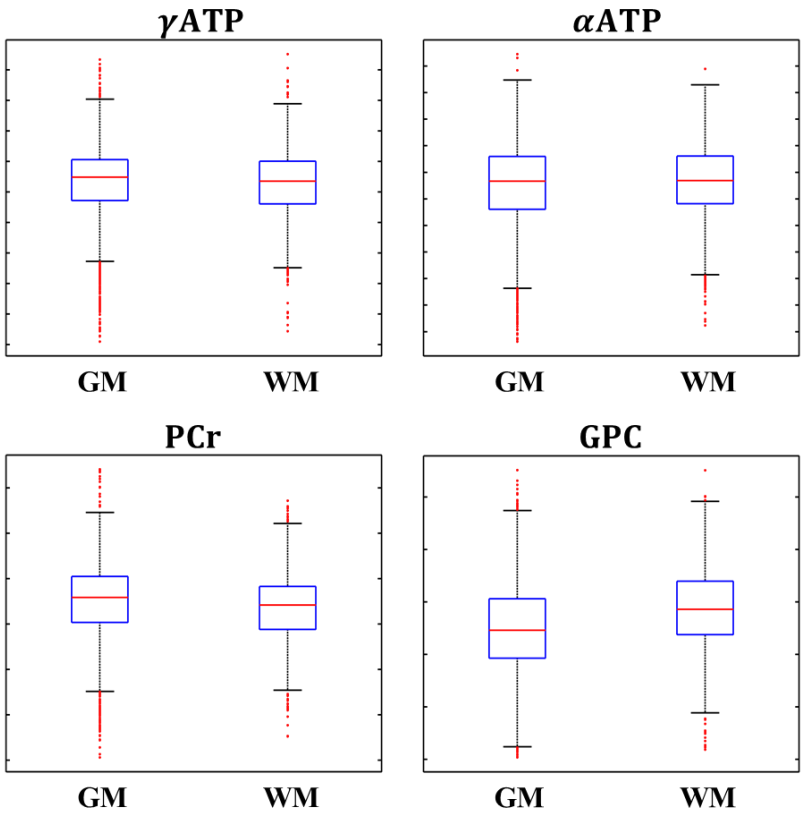

Figure 7.5: Box plots of metabolite concentrations between gray matter and white matter, including PCr, γ-ATP, α-ATP, and GPC.

NAD is one biologically important metabolite detectable by ^{31}P-MRSI. However, due to the low concentration of NAD in human brain (around 0.4 mM), it is very challenging to map NAD distributions using traditional ^{31}P-MRSI methods. To achieve enough SNR for NAD mapping, we used a long ^{31}P-MRSI scan with lower resolution. More specifically, the acquired matrix size was reduced to 15×15×13, and the scan time was along 50 minutes. Under this long scan time and low resolution, the resulting SNR would become possible to achieve good estimation of low concentration metabolites like NAD. Figure 7.6 shows the high-quality spectrum obtained from the scan. The spectral peaks of ^{31}P-metabolites (including PCr, γ-ATP, α-ATP, β-ATP, NAD, Pi, GPC, GPE, PC, and PE) can be clearly observed and well separated with each other. Since the signal of NAD is overlapped with γ-ATP in spectrum, a spectral fitting was performed to resolve these metabolites. The fitting results are also included in Figure 7.6, which show that the spectral fitting method can successfully resolve the metabolites and the resulting residual is near noise level. Figure 7.7 shows spatial maps of the full spectrum of ^{31}P metabolites obtained from this scan, including NAD. Based on the quantification, mean concentration of NAD within the brain is

0.417 ± 0.091 mM, which is close to previously reported value [128]. This shows that the proposed method may provide a potentially powerful imaging tool for NAD mapping.

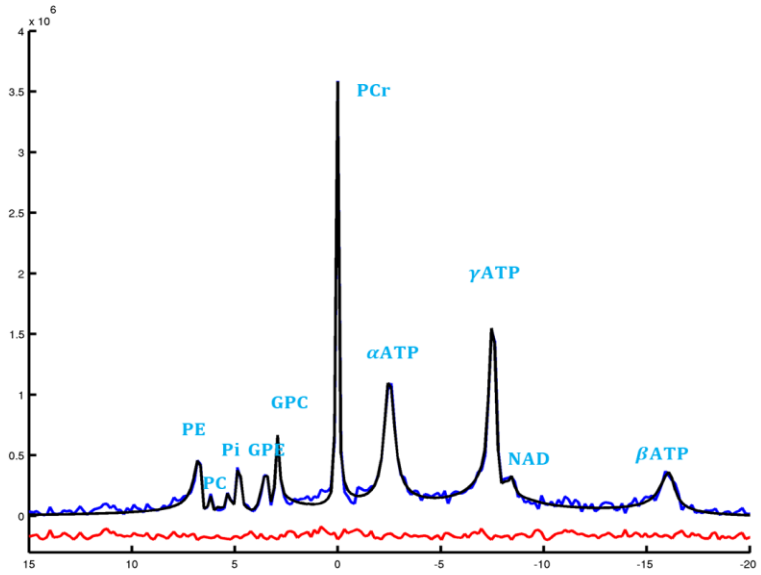

Figure 7.6: A localized spectrum (in blue) obtained from the 50-minute scan, the fitted spectrum by spectral quantification (in black) and difference (in red) are also shown.

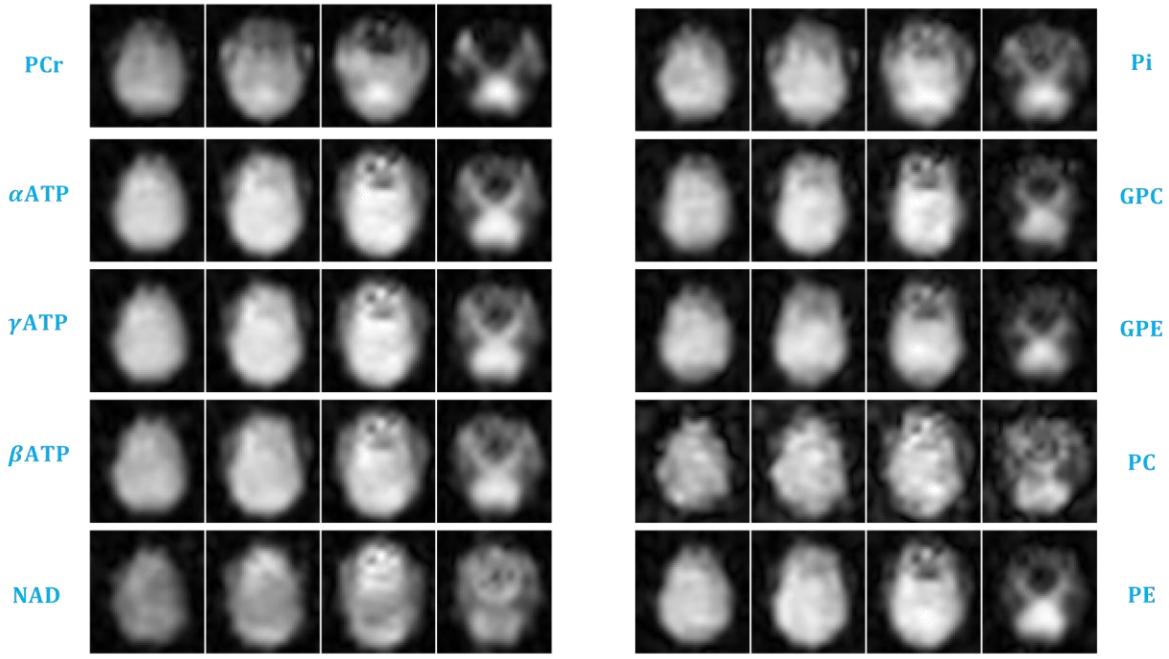

Figure 7.7: Spatial maps of a full spectrum of ^{31}P metabolites obtained from a 50-minute scan, including PCr, γ-ATP, α-ATP, β-ATP, NAD, Pi, GPC, GPE, PC, and PE.

7.4 Summary

In this chapter, ultrahigh field, fast acquisition sequence, and subspace modelling are integrated to achieve high-resolution ^{31}P-MRSI. Both phantom and in vivo experiments have been performed. Experimental results show that the proposed method can significantly reduce the measurement noise and produce high-quality, high-resolution ^{31}P-metabolite maps at 7T. Potential of the method in imaging brain metabolic heterogeneity and mapping low-concentration metabolites like NAD are also successfully demonstrated.

CHAPTER 8 – CONCLUSIONS AND FUTURE DIRECTIONS

8.1 Summary and Conclusions

This thesis research has presented a novel imaging method based on SPICE framework for fast high-resolution MRSI. The presented method synergistically integrates fast acquisition sequence, subspace modelling, and machine learning to make the imaging capability of achieving three-dimensional high-resolution MRSI within a practically acceptable scan time possible. This approach has been used for high-resolution ^{1}H-MRSI at both 3T and 7T, and applied to high-resolution ^{31}P-MRSI at 7T.

For ^{1}H-MRSI at 3T, the proposed acquisition sequence is characterized by several unique features including FID-based acquisition with ultrashort TE, short TR which maximizes SNR and acquisition efficiency, elimination of water/lipid suppression, EPSI trajectories with a large echo-space, motion navigators, and sparse sampling of (k, t)-space in variable density to extend spatial resolution. Combining these features provides remarkable efficiency and robustness for data acquisition, making the SPICE technique feasible for practical and clinical applications. In data processing, a union-of-subspace model is used to represent the overall signals containing water, lipid, and metabolite signals. This subspace modelling significantly reduces the degrees-of-freedom in representing the high-dimensional spatiospectral signals in high-resolution, and it also enables incorporation of spatial and spectral priors in processing. Moreover, the subspace structures of different molecules are pre-learned using both physical priors from quantum mechanics simulation and distribution priors from training data. These processing features make the reconstruction and separation of signals from the noisy and sparse measurements possible. As a result, high-quality metabolite maps at 2.0×3.0×3.0 mm^3 nominal resolution with unsuppressed water signals at 2.0×1.0×1.0 mm^3 resolution can be obtained in an 8-minute scan.

Both phantom and in vivo experiments were carried out to validate and evaluate the performance of the proposed method. The accuracy and reproducibility of the proposed method have been preliminarily validated. Compared with the low-resolution version of SPICE, the proposed method not only provided much higher resolution of metabolite signals, but also showed improved capabilities of water imaging in capturing brain fine-structural features, reducing lipid contamination, and recovering signal drop and distortion in large susceptibility regions. The

proposed method was also applied to a small cohort of tumor patients to demonstrate its values in clinical environments. The preliminary results have shown impressive potential of the proposed method in capturing metabolite alteration of small-size brain tumors, imaging intra-tumoral metabolic heterogeneities, providing biomarkers for noninvasive tumor grading, and evaluating therapeutic efficiency by detecting metabolic responses. This imaging tool should also be of interest for many other clinical applications, like stroke, brain injury, and neurodegenerative diseases.

Ultrahigh field is especially beneficial for MRSI given the enhanced MR signal and more separate spectral resonances. The proposed method was also implemented on 7T to take advantage of the benefits provided by increased field strength. In current implementation, the enhanced SNR was utilized to pursue whole brain coverage without increasing scan time, which is desired by many neuroscience studies. By changing the EPSI readout to slice direction and sub-sampling the metabolite signals, the proposed method could achieve whole brain metabolite mapping at $3.0\times3.0\times3.2$ mm^3 nominal resolution in the same 8-minute scan time. Moreover, the unsuppressed water signals also provided valuable data and information for correction of the increased system imperfections at ultrahigh field. The effectiveness of the method in correcting effects caused by B_0 and B_1 inhomogeneity at 7T and in recovering the sparse sampling of (k, t)-space measurements were well demonstrated in phantom experiments. *In vivo* experiments were also carried out at 7T, and the preliminary results have shown the SNR and contrast improvement brought by ultrahigh field.

With the power of ultrahigh field, the proposed method was also applied for high-resolution ^{31}P-MRSI to map high-energy brain metabolites at 7T. The challenges of ^{31}P-MRSI are relatively more straightforward than ^{1}H-MRSI, mainly on poor SNR. The subspace modelling method of SPICE was integrated with an optimized CSI sequence at 7T to address this challenge. The experimental results from both phantom and healthy subjects have demonstrated the effectiveness of the proposed method in noise reduction and production of high-quality, high-resolution metabolite maps within an acceptable scan time. Its potential in imaging brain metabolic heterogeneity and mapping low-concentration ^{31}P-metabolites like NAD were also successfully demonstrated. With more development in receiving coil and acquisition sequence, the imaging capability should be further improved.

In summary, this thesis research has shown the encouraging progress of SPICE for high-resolution MRSI, from proof-of-concept to a practical imaging technique. The preliminary results have demonstrated its feasibility and capability in multiple aspects, from 3T to 7T, from ^{1}H-MRSI to ^{31}P-MRSI. Its impressive imaging capabilities have been thought impossible but have been dreamed about by scientists and clinicians for many years. With further development, the SPICE method would provide a powerful metabolic imaging tool to map the metabolic fingerprints of brain function and diseases, opening many unique opportunities for neurological, psychiatric studies, and a large range of clinical applications.

8.2 Future Directions

Besides the presented imaging methods, SPICE provides a very unique platform for the development for many other imaging techniques. Given current exciting progress, there are numerous future research works and developments that can be built on this work. A few of them are discussed as follows, including machine learning, multi-contrast imaging, and neurotransmitter mapping.

8.2.1 Machine learning

Recent years have witnessed the tremendous progress on machine learning and artificial intelligence, especially the development of large scale deep neural networks. Benefited from the increased access to large datasets, significantly improved computation power, and developments of well-developed, open deep learning toolbox in near decades, machine learning, especially deep learning techniques have innovated a lot of areas such as computer vision. Machine learning methods have also been extensively applied to medical imaging regarding to many different aspects, such as image segmentation, image reconstruction, and image analysis [129]–[131], achieving very encouraging results. The capability and benefits of machine learning techniques have been greatly recognized by the MR society, and they are being to be applied to almost every aspect of the MR research.

Current spectral priors used in this work are used in the form of linear subspaces, as the union-of-subspaces model presented in section 5.1. Additionally, only a small number of training data are used currently. To further reduce the measurements needed for imaging, or enable higher quality reconstruction from the noisy data, stronger prior knowledge is necessary. This could be

potentially achieved in two ways: one is to obtain prior information from a much larger set of training data, and the other one is to obtain better priors from the training data. Given the emerging progress on deep learning, and more and more data available for training, it is expected that deep learning-based methods can provide better ways to utilize the prior information embedded in the training data. The prior information can be in many forms, such as spatial constraints, spectral constraints, specific distribution, and so on. With such large flexibility and rich information, machine learning type of methods should lead to better reconstruction and processing results for MRSI. Our group already has a few works utilizing the power of machine learning in some specific MR applications [132], [133], and we will keep moving forward in this direction.

8.2.2 Multi-contrast imaging

One beauty of MR techniques is that different contrasts can be generated with different pulse sequences and parameters. After about 40 years since its development, numerous MRI methods have been developed for generating different image contrasts for specific applications. For example, structural imaging methods with T_1-weighting, T_2-weighting, or susceptibility weighting, have been widely used for anatomical examination; functional imaging, especially BOLD (blood oxygenation level dependent)-fMRI has been the indispensable tool for neurological studies; diffusion imaging has been popular for studying white matter fiber structures and diagnosis of ischemic stroke; perfusion imaging has also been used for brain functional studies or tissue viability assessment; quantitative imaging methods such as T_1 mapping, T_2 mapping, and QSM have been recently welcome for tissue characterization; and metabolic imaging as described extensively in previous chapters. These different contrasts provide complementary biological information, and it has been shown that combining multiple imaging modalities can better characterize the tissue and can help improve diagnosis sensitivity and specificity.

However, traditional MR imaging paradigm is to acquire these contrasts one by one with separate pulse sequences, which takes very long scan times and brings challenging registration issues. In recent years, quite a few works on simultaneous multi-contrast imaging have been drawing more and more attention, such as MR fingerprinting (MRF), MR multitasking, STAGE (STrategically Acquired Gradient Echo) imaging, and EPTI (echo planar time-resolved imaging) [134]–[137]. Current multi-contrast methods are only focused on imaging of water signals, thus not including metabolic imaging capability.

As described in previous chapters, the proposed pulse sequence for ^{1}H-MRSI does not suppress water signals, so it provides tremendous flexibility for simultaneous metabolic imaging and water imaging. In one acquisition, the metabolite signals can be used for metabolite mapping, and the unsuppressed water signals can be utilized for imaging many other traditional MRI modalities. More specifically, without any modification, current sequence already provides entire FID signals including T_2^* decay and phase evolution, so structural imaging as typical GRE images and SWI images, and quantitative maps of T_2^*, QSM, and myelin water fraction (MWF) maps can be generated from current sequence [89], [92]. Current FID-based acquisition is very flexible to be integrated with other acquisition modules to generate specific contrast. For example, with interleaved echo volume imaging navigators, the sequence has been extended for simultaneous functional imaging (BOLD-fMRI) and metabolic imaging; with variable flip angle and T_2 preparation pulses, the sequence can be used for simultaneous T_1/T_2 parameter mapping and metabolic imaging; with a diffusion preparation pulses, simultaneous diffusion imaging and metabolic imaging has also been shown feasible. Based on these progresses, it can be expected that with further development, the proposed method can provide a very special imaging technique for simultaneous metabolic imaging, structural imaging, quantitative imaging, and functional imaging within a practical scan time.

8.2.3 Neurotransmitter mapping

As introduced in section 2.1, neurotransmitters glutamate and GABA play central roles in excitatory and inhibitory neurotransmission process, respectively. Mapping neurotransmitters can provide valuable insights on brain functionality and the underlying physiology of many mental disorders like schizophrenia, anxiety disorders, and depression [53]–[58]. However, there are several long-standing technical difficulties for neurotransmitter mapping using ^{1}H-MRSI. As the difficulties of typical ^{1}H-MRSI methods, it suffers from low sensitivity and huge nuisance signals, thus is limited in low-resolution and long scan time. Moreover, the resonances of glutamate are largely overlapping with glutamine, and the resonances of GABA are largely overlapped with NAA, glutamate/glutamine, creatine, and broad macromolecule resonances. These sensitivity and spectral overlapping issues make neurotransmitter mapping very challenging. Current MRSI methods exploit multi-TE J-resolve or J-editing techniques to address the spectral overlapping issue, but these techniques require additional scan time. Therefore, most current neurotransmitter

mapping methods are limited to single voxel or very low spatial resolution, which cannot fulfill the practical research and clinical needs.

Current ^{1}H-SPICE method provides high-resolution mapping of several metabolites with high concentrations and little overlapping with other metabolites, like NAA, Cr, Cho, Ins, and Glx (combination of Glu and Gln), but it has good potential to map neurotransmitters via additional extension or improvements. The acquisition features and subspace-based processing methods can be easily adapted and utilized to address the imaging problems of neurotransmitter mapping techniques. In addition, ultrahigh field as 7T can provide significantly enhanced SNR and better spectral separation, which are very beneficial for neurotransmitter mapping methods. So the experience of this thesis research at 7T will also benefit the development of neurotransmitter mapping techniques. Our group has already done some preliminary works using SPICE for J-resolved MRSI at 3T [138], showing very encouraging results. Based on the progress, SPICE should be able to provide a more powerful imaging tool to neurotransmitter mapping in the near future.

REFERENCES

[1] R. J. Gropler, "Recent advances in metabolic imaging," *Journal of Nuclear Cardiology*, vol. 20, no. 6. pp. 1147–1172, 2013, doi: 10.1007/s12350-013-9786-z.

[2] P. J. Magistretti and I. Allaman, "A Cellular Perspective on Brain Energy Metabolism and Functional Imaging," *Neuron*, vol. 86, no. 4. pp. 883–901, 2015, doi: 10.1016/j.neuron.2015.03.035.

[3] S. Camandola and M. P. Mattson, "Brain metabolism in health, aging, and neurodegeneration," *EMBO J.*, vol. 36, no. 11, pp. 1474–1492, 2017, doi: 10.15252/embj.201695810.

[4] S. M. Ametamey, M. Honer, and P. A. Schubiger, "Molecular imaging with PET," *Chemical Reviews*, vol. 108, no. 5. pp. 1501–1516, 2008, doi: 10.1021/cr0782426.

[5] W. Chen, "Clinical applications of PET in brain tumors," *Journal of Nuclear Medicine*, vol. 48, no. 9. pp. 1468–1481, 2007, doi: 10.2967/jnumed.106.037689.

[6] S. Posse, R. Otazo, S. R. Dager, and J. Alger, "MR spectroscopic imaging: Principles and recent advances," *Journal of Magnetic Resonance Imaging*, vol. 37, no. 6. pp. 1301–1325, 2013, doi: 10.1002/jmri.23945.

[7] A. J. Walsh *et al.*, "Optical metabolic imaging identifies glycolytic levels, subtypes, and early-treatment response in breast cancer," *Cancer Res.*, vol. 73, no. 20, pp. 6164–6174, 2013, doi: 10.1158/0008-5472.CAN-13-0527.

[8] E. M. Rohren, T. G. Turkington, and R. E. Coleman, "Clinical Applications of PET in Oncology," *Radiology*, vol. 231, no. 2. pp. 305–332, 2004, doi: 10.1148/radiol.2312021185.

[9] K. Herholz, "Use of FDG PET as an imaging biomarker in clinical trials of Alzheimers disease," *Biomarkers in Medicine*, vol. 6, no. 4. pp. 431–439, 2012, doi: 10.2217/bmm.12.51.

[10] G. Öz *et al.*, "Clinical proton MR spectroscopy in central nervous system disorders," *Radiology*, vol. 270, no. 3. pp. 658–679, 2014, doi: 10.1148/radiol.13130531.

[11] P. C. Lauterbur, D. M. Kramer, W. V. House, and C. N. Chen, "Zeugmatographic High Resolution Nuclear Magnetic Resonance Spectroscopy. Images of Chemical Inhomogeneity within Macroscopic Objects," *Journal of the American Chemical Society*, vol. 97, no. 23. pp. 6866–6868, 1975, doi: 10.1021/ja00856a046.

[12] T. R. Brown, B. M. Kincaid, and K. Ugurbil, "NMR chemical shift imaging in three dimensions," *Proc. Natl. Acad. Sci. U. S. A.*, vol. 79, no. 11 I, pp. 3523–3526, 1982, doi: 10.1073/pnas.79.11.3523.

[13] P. Mansfield, "Spatial mapping of the chemical shift in NMR," *Magn. Reson. Med.*, vol. 1, no. 3, pp. 370–386, 1984, doi: 10.1002/mrm.1910010308.

[14] C. T. W. Moonen *et al.*, "Comparison of single-shot localization methods (steam and press) for In vivo proton NMR spectroscopy," *NMR Biomed.*, vol. 2, no. 5–6, pp. 201–208, 1989, doi: 10.1002/nbm.1940020506.

[15] A. Haase, J. Frahm, W. Hanicke, and D. Matthaei, "1H NMR chemical shift selective (CHESS) imaging," *Phys. Med. Biol.*, vol. 30, no. 4, pp. 341–344, 1985, doi: 10.1088/0031-9155/30/4/008.

[16] T. W. J. Scheenen, D. W. J. Klomp, J. P. Wijnen, and A. Heerschap, “Short echo time 1H-MRSI of the human brain at 3T with minimal chemical shift displacement errors using adiabatic refocusing pulses,” *Magn. Reson. Med.*, vol. 59, no. 1, pp. 1–6, 2008, doi: 10.1002/mrm.21302.

[17] R. J. Ogg, P. B. Kingsley, and J. S. Taylor, “WET, a T1- and B1-Insensitive Water-Suppression Method for in Vivo Localized 1H NMR Spectroscopy,” *J. Magn. Reson. Ser. B*, 1994, doi: 10.1006/jmrb.1994.1048.

[18] A. Ebel, V. Govindaraju, and A. A. Maudsley, “Comparison of inversion recovery preparation schemes for lipid suppression in 1H MRSI of human brain,” *Magn. Reson. Med.*, vol. 49, no. 5, pp. 903–908, 2003, doi: 10.1002/mrm.10444.

[19] D. D. Doddrell *et al.*, “The utilization of two frequency-shifted sinc pulses for performing volume-selected in vivo NMR spectroscopy,” *Magn. Reson. Med.*, vol. 3, no. 6, pp. 970–975, 1986, doi: 10.1002/mrm.1910030620.

[20] S. Posse, G. Tedeschi, R. Risinger, R. Ogg, and D. Le Bihan, “High Speed 1H Spectroscopic Imaging in Human Brain by Echo Planar Spatial-Spectral Encoding,” *Magn. Reson. Med.*, vol. 33, no. 1, pp. 34–40, 1995, doi: 10.1002/mrm.1910330106.

[21] E. Adalsteinsson, P. Irarrazabal, S. Topp, C. Meyer, A. Macovski, and D. M. Spielman, “Volumetric spectroscopic imaging with spiral-based k-space trajectories,” *Magn. Reson. Med.*, vol. 39, no. 6, pp. 889–898, 1998, doi: 10.1002/mrm.1910390606.

[22] M. Chiew *et al.*, “Density-weighted concentric rings k-space trajectory for 1H magnetic resonance spectroscopic imaging at 7 T,” *NMR Biomed.*, vol. 31, no. 1, 2018, doi: 10.1002/nbm.3838.

[23] K. P. Pruessmann, M. Weiger, M. B. Scheidegger, and P. Boesiger, “SENSE: Sensitivity encoding for fast MRI,” *Magn. Reson. Med.*, vol. 42, no. 5, pp. 952–962, 1999, doi: 10.1002/(SICI)1522-2594(199911)42:5<952::AID-MRM16>3.0.CO;2-S.

[24] M. A. Griswold *et al.*, “Generalized Autocalibrating Partially Parallel Acquisitions (GRAPPA),” *Magn. Reson. Med.*, vol. 47, no. 6, pp. 1202–1210, 2002, doi: 10.1002/mrm.10171.

[25] M. Lustig, D. Donoho, and J. M. Pauly, “Sparse MRI: The application of compressed sensing for rapid MR imaging,” *Magn. Reson. Med.*, vol. 58, no. 6, pp. 1182–1195, 2007, doi: 10.1002/mrm.21391.

[26] H. M. Nguyen, X. Peng, M. N. Do, and Z. P. Liang, “Denoising MR spectroscopic imaging data with low-rank approximations,” *IEEE Trans. Biomed. Eng.*, vol. 60, no. 1, pp. 78–89, 2013, doi: 10.1109/TBME.2012.2223466.

[27] Y. Liu, C. Ma, B. A. Clifford, F. Lam, C. L. Johnson, and Z. P. Liang, “Improved low-rank filtering of magnetic resonance spectroscopic imaging data corrupted by noise and B0 field inhomogeneity,” *IEEE Trans. Biomed. Eng.*, vol. 63, no. 4, pp. 841–849, 2016, doi: 10.1109/TBME.2015.2476499.

[28] L. Vanhamme, A. Van Den Boogaart, and S. Van Huffel, “Improved Method for Accurate and Efficient Quantification of MRS Data with Use of Prior Knowledge,” *J. Magn. Reson.*, vol. 129, no. 1, pp. 35–43, 1997, doi: 10.1006/jmre.1997.1244.

[29] R. Eslami and M. Jacob, “A sparse reconstruction algorithm for parallel spiral MR spectroscopic imaging,” in *Proceedings - International Symposium on Biomedical Imaging*, 2011, pp. 93–96,

doi: 10.1109/ISBI.2011.5872362.

[30] F. H. Lin *et al.*, “Sensitivity-encoded (SENSE) proton echo-planar spectroscopic imaging (PEPSI) in the human brain,” *Magn. Reson. Med.*, vol. 57, no. 2, pp. 249–257, 2007, doi: 10.1002/mrm.21119.

[31] Q. Ning, C. Ma, F. Lam, and Z. P. Liang, “Spectral Quantification for High-Resolution MR Spectroscopic Imaging with Spatiospectral Constraints,” *IEEE Trans. Biomed. Eng.*, vol. 64, no. 5, pp. 1178–1186, 2017, doi: 10.1109/TBME.2016.2594583.

[32] Y. Li, F. Lam, B. Clifford, and Z. P. Liang, “A subspace approach to spectral quantification for MR spectroscopic imaging,” *IEEE Trans. Biomed. Eng.*, vol. 64, no. 10, pp. 2486–2489, 2017, doi: 10.1109/TBME.2017.2741922.

[33] Z. P. Liang, “Spatiotemporal imaging with partially separable functions,” in *2007 4th IEEE International Symposium on Biomedical Imaging: From Nano to Macro - Proceedings*, 2007, pp. 988–991, doi: 10.1109/ISBI.2007.357020.

[34] F. Lam and Z. P. Liang, “A subspace approach to high-resolution spectroscopic imaging,” *Magn. Reson. Med.*, vol. 71, no. 4, pp. 1349–1357, 2014, doi: 10.1002/mrm.25168.

[35] F. Lam, C. Ma, B. Clifford, C. L. Johnson, and Z. P. Liang, “High-resolution 1H-MRSI of the brain using SPICE: Data acquisition and image reconstruction,” *Magn. Reson. Med.*, vol. 76, no. 4, pp. 1059–1070, 2016, doi: 10.1002/mrm.26019.

[36] C. Ma, F. Lam, Q. Ning, C. L. Johnson, and Z. P. Liang, “High-resolution 1H-MRSI of the brain using short-TE SPICE,” *Magn. Reson. Med.*, vol. 77, no. 2, pp. 467–479, 2017, doi: 10.1002/mrm.26130.

[37] M. I. Karamat, S. Darvish-Molla, and A. Santos-Diaz, “Opportunities and challenges of 7 tesla magnetic resonance imaging: A review,” *Critical Reviews in Biomedical Engineering*, vol. 44, no. 1–2. pp. 73–89, 2016, doi: 10.1615/CritRevBiomedEng.2016016365.

[38] E. Moser, F. Stahlberg, M. E. Ladd, and S. Trattnig, “7-T MR-from research to clinical applications?,” *NMR in Biomedicine*, vol. 25, no. 5. pp. 695–716, 2012, doi: 10.1002/nbm.1794.

[39] G. Barisano *et al.*, “Clinical 7 t MRi: Are we there yet? A review about magnetic resonance imaging at ultra-high field,” *British Journal of Radiology*, vol. 92, no. 1094. 2019, doi: 10.1259/bjr.20180492.

[40] A. G. Van Der Kolk, J. Hendrikse, J. J. M. Zwanenburg, F. Visser, and P. R. Luijten, “Clinical applications of 7 T MRI in the brain,” *European Journal of Radiology*, vol. 82, no. 5. pp. 708–718, 2013, doi: 10.1016/j.ejrad.2011.07.007.

[41] R. Sladky *et al.*, “High-resolution functional MRI of the human amygdala at 7 T,” *Eur. J. Radiol.*, vol. 82, no. 5, pp. 728–733, 2013, doi: 10.1016/j.ejrad.2011.09.025.

[42] N. Harel, “Ultra high resolution fMRI at ultra-high field,” *NeuroImage*, vol. 62, no. 2. pp. 1024–1028, 2012, doi: 10.1016/j.neuroimage.2012.01.018.

[43] T. Tourdias, M. Saranathan, I. R. Levesque, J. Su, and B. K. Rutt, “Visualization of intra-thalamic nuclei with optimized white-matter-nulled MPRAGE at 7T,” *Neuroimage*, vol. 84, pp. 534–545, 2014, doi: 10.1016/j.neuroimage.2013.08.069.

[44] F. Pittau *et al.*, “MP2RAGE and Susceptibility-Weighted Imaging in Lesional Epilepsy at 7T,” *J. Neuroimaging*, vol. 28, no. 4, pp. 365–369, 2018, doi: 10.1111/jon.12523.

[45] J. M. Lupo *et al.*, “7-Tesla Susceptibility-Weighted Imaging To Assess the Effects of Radiotherapy on Normal-Appearing Brain in Patients With Glioma,” *Int. J. Radiat. Oncol. Biol. Phys.*, vol. 82, no. 3, 2012, doi: 10.1016/j.ijrobp.2011.05.046.

[46] G. Hangel *et al.*, “Ultra-high resolution brain metabolite mapping at 7 T by short-TR Hadamard-encoded FID-MRSI,” *Neuroimage*, vol. 168, pp. 199–210, 2018, doi: 10.1016/j.neuroimage.2016.10.043.

[47] L. Hingerl *et al.*, “Clinical High-Resolution 3D-MR Spectroscopic Imaging of the Human Brain at 7 T,” *Invest. Radiol.*, vol. 55, no. 4, pp. 239–248, 2020, doi: 10.1097/RLI.0000000000000626.

[48] S. Nassirpour, P. Chang, and A. Henning, “High and ultra-high resolution metabolite mapping of the human brain using 1H FID MRSI at 9.4T,” *Neuroimage*, vol. 168, pp. 211–221, 2018, doi: 10.1016/j.neuroimage.2016.12.065.

[49] E. Coello *et al.*, “High-resolution echo-planar spectroscopic imaging at ultra-high field,” *NMR Biomed.*, vol. 31, no. 11, 2018, doi: 10.1002/nbm.3950.

[50] A. Klauser, B. Strasser, B. Thapa, F. Lazeyras, and O. Andronesi, “Achieving high-resolution 1H-MRSI of the human brain with compressed-sensing and low-rank reconstruction at 7 Tesla,” *J. Magn. Reson.*, vol. 331, 2021, doi: 10.1016/j.jmr.2021.107048.

[51] F. Hyder and D. L. Rothman, “Advances in Imaging Brain Metabolism,” *Annu. Rev. Biomed. Eng.*, vol. 19, pp. 485–515, 2017, doi: 10.1146/annurev-bioeng-071516-044450.

[52] J. Albrecht, M. Sidoryk-Węgrzynowicz, M. Zielińska, and M. Aschner, “Roles of glutamine in neurotransmission,” *Neuron Glia Biol.*, vol. 6, no. 4, pp. 263–276, 2010, doi: 10.1017/S1740925X11000093.

[53] L. M. Rowland *et al.*, “In vivo measurements of glutamate, GABA, and NAAG in schizophrenia,” *Schizophr. Bull.*, vol. 39, no. 5, pp. 1096–1104, 2013, doi: 10.1093/schbul/sbs092.

[54] V. Kumar, S. Manchegowda, A. Jacob, and N. P. Rao, “Glutamate metabolites in treatment resistant schizophrenia: A meta-analysis and systematic review of 1H-MRS studies,” *Psychiatry Res. - Neuroimaging*, vol. 300, 2020, doi: 10.1016/j.pscychresns.2020.111080.

[55] J. W. Liao, S. S. Wang, H. H. Yang, P. Ma, C. R. Li, and J. Y. Pan, “Comparative analysis of serum glutamate and gamma-aminobutyric acid levels in patients with bipolar depressive disorder and major depression disorder,” *Zhonghua Yi Xue Za Zhi*, vol. 100, no. 23, pp. 1800–1804, 2020, doi: 10.3760/cma.j.cn112137-20191025-02319.

[56] A. A. Rey, M. Purrio, M. P. Viveros, and B. Lutz, “Biphasic effects of cannabinoids in anxiety responses: CB1 and GABA B receptors in the balance of gabaergic and glutamatergic neurotransmission,” *Neuropsychopharmacology*, vol. 37, no. 12, pp. 2624–2634, 2012, doi: 10.1038/npp.2012.123.

[57] J. Persson *et al.*, “Inhibitory and excitatory neurotransmitter systems in depressed and healthy: A positron emission tomography and magnetic resonance spectroscopy study,” *Psychiatry Res. - Neuroimaging*, vol. 315, 2021, doi: 10.1016/j.pscychresns.2021.111327.

[58] D. P. Auer, B. Pütz, E. Kraft, B. Lipinski, J. Schill, and F. Holsboer, “Reduced glutamate in the

anterior cingulate cortex in depression: An in vivo proton magnetic resonance spectroscopy study," *Biol. Psychiatry*, vol. 47, no. 4, pp. 305–313, 2000, doi: 10.1016/S0006-3223(99)00159-6.

[59] J. R. Moffett, B. Ross, P. Arun, C. N. Madhavarao, and A. M. A. Namboodiri, "N-Acetylaspartate in the CNS: From neurodiagnostics to neurobiology," *Progress in Neurobiology*, vol. 81, no. 2. pp. 89–131, 2007, doi: 10.1016/j.pneurobio.2006.12.003.

[60] K. Glunde, Z. M. Bhujwalla, and S. M. Ronen, "Choline metabolism in malignant transformation," *Nature Reviews Cancer*, vol. 11, no. 12. pp. 835–848, 2011, doi: 10.1038/nrc3162.

[61] K. R. Byrnes *et al.*, "FDG-PET imaging in mild traumatic brain injury: A critical review," *Front. Neuroenergetics*, vol. 6, no. JAN, 2014, doi: 10.3389/fnene.2013.00013.

[62] F. Biver *et al.*, "Frontal and parietal metabolic disturbances in unipolar depression," *Biol. Psychiatry*, vol. 36, no. 6, pp. 381–388, 1994, doi: 10.1016/0006-3223(94)91213-0.

[63] D. Zhang, Y. Wang, L. Zhou, H. Yuan, and D. Shen, "Multimodal classification of Alzheimer's disease and mild cognitive impairment," *Neuroimage*, vol. 55, no. 3, pp. 856–867, 2011, doi: 10.1016/j.neuroimage.2011.01.008.

[64] L. Mosconi, "Brain glucose metabolism in the early and specific diagnosis of Alzheimer's disease: FDG-PET studies in MCI and AD," *European Journal of Nuclear Medicine and Molecular Imaging*, vol. 32, no. 4. pp. 486–510, 2005, doi: 10.1007/s00259-005-1762-7.

[65] S. K. Meles, L. K. Teune, B. M. De Jong, R. A. Dierckx, and K. L. Leenders, "Metabolic imaging in parkinson disease," *Journal of Nuclear Medicine*, vol. 58, no. 1. pp. 23–28, 2017, doi: 10.2967/jnumed.116.183152.

[66] P. T. Meyer, L. Frings, G. Rücker, and S. Hellwig, "18F-FDG PET in Parkinsonism: Differential diagnosis and evaluation of cognitive impairment," *J. Nucl. Med.*, vol. 58, no. 12, pp. 1888–1898, 2017, doi: 10.2967/jnumed.116.186403.

[67] T. Belhocine *et al.*, "18FDG PET in oncology: The best and the worst (review)," *International Journal of Oncology*, vol. 28, no. 5. pp. 1249–1261, 2006, doi: 10.3892/ijo.28.5.1249.

[68] A. Horská and P. B. Barker, "Imaging of brain tumors: MR spectroscopy and metabolic imaging," *Neuroimaging Clinics of North America*, vol. 20, no. 3. pp. 293–310, 2010, doi: 10.1016/j.nic.2010.04.003.

[69] P. B. Barker *et al.*, "Acute stroke: Evaluation with serial proton MR spectroscopic imaging," *Radiology*, vol. 192, no. 3, pp. 723–732, 1994, doi: 10.1148/radiology.192.3.8058940.

[70] L. A. Jelen, S. King, P. G. Mullins, and J. M. Stone, "Beyond static measures: A review of functional magnetic resonance spectroscopy and its potential to investigate dynamic glutamatergic abnormalities in schizophrenia," *Journal of Psychopharmacology*, vol. 32, no. 5. pp. 497–508, 2018, doi: 10.1177/0269881117747579.

[71] X. H. Zhu, M. Lu, and W. Chen, "Quantitative imaging of brain energy metabolisms and neuroenergetics using in vivo X-nuclear 2H, 17O and 31P MRS at ultra-high field," *J. Magn. Reson.*, vol. 292, pp. 155–170, 2018, doi: 10.1016/j.jmr.2018.05.005.

[72] R. M. Blumberg, E. B. Cady, J. S. Wigglesworth, J. E. McKenzie, and A. D. Edwards, "Relation between delayed impairment of cerebral energy metabolism and infarction following transient

focal hypoxia-ischaemia in the developing brain," *Exp. Brain Res.*, vol. 113, no. 1, pp. 130–137, 1997, doi: 10.1007/BF02454148.

[73] R. G. Gonzalez, A. R. Guimaraes, G. J. Moore, A. Crawley, L. A. Cupples, and J. H. Growdon, "Quantitative in vivo 31P magnetic resonance spectroscopy of Alzheimer disease," *Alzheimer Dis. Assoc. Disord.*, vol. 10, no. 1, pp. 46–52, 1996, doi: 10.1097/00002093-199601010-00008.

[74] J. W. Hugg, G. B. Matson, D. B. Twieg, A. A. Maudsley, D. Sappey-Marinier, and M. W. Weiner, "Phosphorus-31 MR spectroscopic imaging (MRSI) of normal and pathological human brains," *Magn. Reson. Imaging*, vol. 10, no. 2, pp. 227–243, 1992, doi: 10.1016/0730-725X(92)90483-G.

[75] P. N. Jayakumar, B. N. Gangadhar, D. K. Subbakrishna, N. Janakiramaiah, J. S. Srinivas, and M. S. Keshavan, "Membrane phospholipid abnormalities of basal ganglia in never-treated schizophrenia: A 31P magnetic resonance spectroscopy study," *Biol. Psychiatry*, vol. 54, no. 4, pp. 491–494, 2003, doi: 10.1016/S0006-3223(02)01829-2.

[76] W. Bogner, R. Otazo, and A. Henning, "Accelerated MR spectroscopic imaging—a review of current and emerging techniques," *NMR in Biomedicine*, vol. 34, no. 5. 2021, doi: 10.1002/nbm.4314.

[77] J. K. Furuyama, N. E. Wilson, and M. A. Thomas, "Spectroscopic imaging using concentrically circular echo-planar trajectories in vivo," *Magnetic Resonance in Medicine*, vol. 67, no. 6. pp. 1515–1522, 2012, doi: 10.1002/mrm.23184.

[78] D. C. Noll, "Multishot rosette trajectories for spectrally selective mr imaging," *IEEE Trans. Med. Imaging*, vol. 16, no. 4, pp. 372–377, 1997, doi: 10.1109/42.611345.

[79] M. S. Ramirez *et al.*, "Radial spectroscopic MRI of hyperpolarized [1-13C] pyruvate at 7 tesla," *Magn. Reson. Med.*, vol. 72, no. 4, pp. 986–995, 2014, doi: 10.1002/mrm.25004.

[80] A. Papoulis, "Generalized Sampling Expansion," *IEEE Trans. Circuits Syst.*, vol. 24, no. 11, pp. 652–654, 1977, doi: 10.1109/TCS.1977.1084284.

[81] J. P. Haldar, D. Hernando, S. K. Song, and Z. P. Liang, "Anatomically constrained reconstruction from noisy data," *Magn. Reson. Med.*, vol. 59, no. 4, pp. 810–818, 2008, doi: 10.1002/mrm.21536.

[82] M. Resonance *et al.*, "Constrained reconstruction methods in MR imaging," *Rev Magn Reson Med*, vol. 4, no. 217, pp. 67–185, 1992, [Online]. Available: http://scholar.google.com/scholar?hl=en&btnG=Search&q=intitle:Constrained+Reconstruction+Methods+in+MR+Imaging#0.

[83] K. K. Kwong *et al.*, "Dynamic magnetic resonance imaging of human brain activity during primary sensory stimulation.," *Proc. Natl. Acad. Sci. U. S. A.*, vol. 89, no. 12, pp. 5675–5679, 1992, doi: 10.1073/pnas.89.12.5675.

[84] Z. P. Liang, H. Jiang, C. P. Hess, and P. C. Lauterbur, "Dynamic imaging by model estimation," *Int. J. Imaging Syst. Technol.*, vol. 8, no. 6, 1997, doi: 10.1002/(SICI)1098-1098(1997)8:6<551::AID-IMA7>3.0.CO;2-9.

[85] Z. P. Liang and P. C. Lauterbur, "A Generalized Series Approach to MR Spectroscopic Imaging," *IEEE Trans. Med. Imaging*, vol. 10, no. 2, pp. 132–137, 1991, doi: 10.1109/42.79470.

[86] J. He, Q. Liu, A. G. Christodoulou, C. Ma, F. Lam, and Z. P. Liang, "Accelerated High-Dimensional MR Imaging with Sparse Sampling Using Low-Rank Tensors," *IEEE Trans. Med.*

Imaging, vol. 35, no. 9, pp. 2119–2129, 2016, doi: 10.1109/TMI.2016.2550204.

[87] X. Hu, D. N. Levin, P. C. Lauterbur, and T. Spraggins, "SLIM: Spectral localization by imaging," *Magn. Reson. Med.*, vol. 8, no. 3, pp. 314–322, 1988, doi: 10.1002/mrm.1910080308.

[88] D. Hernando, Z. P. Liang, and P. Kellman, "Chemical shift-based water/fat separation: A comparison of signal models," *Magn. Reson. Med.*, vol. 64, no. 3, pp. 811–822, 2010, doi: 10.1002/mrm.22455.

[89] X. Peng, F. Lam, Y. Li, B. Clifford, and Z. P. Liang, "Simultaneous QSM and metabolic imaging of the brain using SPICE," *Magn. Reson. Med.*, vol. 79, no. 1, pp. 13–21, 2018, doi: 10.1002/mrm.26972.

[90] R. Guo, Y. Zhao, Y. Li, Y. Li, and Z. P. Liang, "Simultaneous metabolic and functional imaging of the brain using SPICE," *Magn. Reson. Med.*, vol. 82, no. 6, pp. 1993–2002, 2019, doi: 10.1002/mrm.27865.

[91] F. Lam, Y. Li, R. Guo, B. Clifford, and Z. P. Liang, "Ultrafast magnetic resonance spectroscopic imaging using SPICE with learned subspaces," *Magn. Reson. Med.*, vol. 83, no. 2, pp. 377–390, 2020, doi: 10.1002/mrm.27980.

[92] R. Guo *et al.*, "Simultaneous QSM and metabolic imaging of the brain using SPICE: Further improvements in data acquisition and processing," *Magn. Reson. Med.*, vol. 85, no. 2, pp. 970–977, 2021, doi: 10.1002/mrm.28459.

[93] Y. Li *et al.*, "Fast high-resolution metabolic imaging of acute stroke with 3D magnetic resonance spectroscopy," *Brain*, vol. 143, no. 11, pp. 3225–3233, 2021, doi: 10.1093/BRAIN/AWAA264.

[94] R. Guo *et al.*, "High-Resolution Label-Free Molecular Imaging of Brain Tumor," *Proc. Annu. Int. Conf. IEEE Eng. Med. Biol. Soc. EMBS*, pp. 3049–3052, 2021, doi: 10.1109/EMBC46164.2021.9630623.

[95] B. Guérin *et al.*, "The ultimate signal-to-noise ratio in realistic body models," *Magn. Reson. Med.*, vol. 78, no. 5, pp. 1969–1980, 2017, doi: 10.1002/mrm.26564.

[96] L. Wald and E. Adalsteinsson, "Parallel transmit technology for high field MRI," *MAGNETOM Flash*, pp. 124–135, 2009, [Online]. Available: http://www.medical.siemens.com/siemens/it_IT/rg_marcom_FBAs/files/brochures/magnetom_2009_05/MAGNETOM_Flash_May_2009_High_Field_MRI.pdf.

[97] M. De Greef, O. Ipek, A. J. E. Raaijmakers, J. Crezee, and C. A. T. Van Den Berg, "Specific absorption rate intersubject variability in 7T parallel transmit MRI of the head," *Magn. Reson. Med.*, vol. 69, no. 5, pp. 1476–1485, 2013, doi: 10.1002/mrm.24378.

[98] F. Godenschweger *et al.*, "Motion correction in MRI of the brain," *Physics in Medicine and Biology*, vol. 61, no. 5. pp. R32–R56, 2016, doi: 10.1088/0031-9155/61/5/R32.

[99] T. Lange, J. MacLaren, M. Buechert, and M. Zaitsev, "Spectroscopic imaging with prospective motion correction and retrospective phase correction," *Magnetic Resonance in Medicine*, vol. 67, no. 6. pp. 1506–1514, 2012, doi: 10.1002/mrm.23136.

[100] A. J. W. Van Der Kouwe, T. Benner, and A. M. Dale, "Real-time rigid body motion correction and shimming using cloverleaf navigators," *Magn. Reson. Med.*, vol. 56, no. 5, pp. 1019–1032, 2006, doi: 10.1002/mrm.21038.

[101] W. Bogner *et al.*, "3D GABA imaging with real-time motion correction, shim update and reacquisition of adiabatic spiral MRSI," *Neuroimage*, vol. 103, pp. 290–302, 2014, doi: 10.1016/j.neuroimage.2014.09.032.

[102] B. C. Andrews-Shigaki, B. S. R. Armstrong, M. Zaitsev, and T. Ernst, "Prospective motion correction for magnetic resonance spectroscopy using single camera retro-grate reflector optical tracking," *J. Magn. Reson. Imaging*, vol. 33, no. 2, pp. 498–504, 2011, doi: 10.1002/jmri.22467.

[103] A. T. Hess, O. C. Andronesi, M. Dylan Tisdall, A. Gregory Sorensen, A. J. W. van der Kouwe, and E. M. Meintjes, "Real-time motion and B 0 correction for localized adiabatic selective refocusing (LASER) MRSI using echo planar imaging volumetric navigators," *NMR Biomed.*, vol. 25, no. 2, pp. 347–358, 2012, doi: 10.1002/nbm.1756.

[104] F. A. Breuer *et al.*, "Controlled aliasing in volumetric parallel imaging (2D CAIPIRINHA)," *Magn. Reson. Med.*, vol. 55, no. 3, pp. 549–556, 2006, doi: 10.1002/mrm.20787.

[105] F. A. Breuer, M. Blaimer, R. M. Heidemann, M. F. Mueller, M. A. Griswold, and P. M. Jakob, "Controlled aliasing in parallel imaging results in higher acceleration (CAIPIRINHA) for multi-slice imaging," *Magn. Reson. Med.*, vol. 53, no. 3, pp. 684–691, 2005, doi: 10.1002/mrm.20401.

[106] Z. P. Liang and P. C. Lauterbur, "An Efficient Method for Dynamic Magnetic Resonance Imaging," *IEEE Trans. Med. Imaging*, vol. 13, no. 4, pp. 677–686, 1994, doi: 10.1109/42.363100.

[107] S. A. Smith, T. O. Levante, B. H. Meier, and R. R. Ernst, "Computer Simulations in Magnetic Resonance. An Object-Oriented Programming Approach," *J. Magn. Reson. Ser. A*, vol. 106, no. 1, pp. 75–105, 1994, doi: 10.1006/jmra.1994.1008.

[108] B. J. Soher, K. Young, A. Bernstein, Z. Aygula, and A. A. Maudsley, "GAVA: Spectral simulation for in vivo MRS applications," *J. Magn. Reson.*, vol. 185, no. 2, pp. 291–299, 2007, doi: 10.1016/j.jmr.2007.01.005.

[109] B. J. Soher, P. Semanchuk, D. Todd, J. Steinberg, and K. Young, "VeSPA: Integrated applications for RF pulse design, spectral simulation and MRS data analysis," in *Proceedings of the 19th Meeting of ISMRM, Montreal 2011*, 2011, vol. 19, p. 1410.

[110] D. Graveron-Demilly, A. Diop, A. Briguet, and B. Fenet, "Product-operator algebra for strongly coupled spin systems," *J. Magn. Reson. - Ser. A*, vol. 101, no. 3, pp. 233–239, 1993, doi: 10.1006/jmra.1993.1038.

[111] H. J. Hogben, M. Krzystyniak, G. T. P. Charnock, P. J. Hore, and I. Kuprov, "Spinach - A software library for simulation of spin dynamics in large spin systems," *J. Magn. Reson.*, vol. 208, no. 2, pp. 179–194, 2011, doi: 10.1016/j.jmr.2010.11.008.

[112] D. Stefan *et al.*, "Quantitation of magnetic resonance spectroscopy signals: The jMRUI software package," *Meas. Sci. Technol.*, vol. 20, no. 10, 2009, doi: 10.1088/0957-0233/20/10/104035.

[113] S. Mangia *et al.*, "Sensitivity of single-voxel 1H-MRS in investigating the metabolism of the activated human visual cortex at 7 T," *Magn. Reson. Imaging*, vol. 24, no. 4, pp. 343–348, 2006, doi: 10.1016/j.mri.2005.12.023.

[114] B. J. Soher, P. Semanchuk, D. Todd, J. Steinberg, and K. Young, "VeSPA: Integrated applications for RF pulse design, spectral simulation and MRS data analysis," in *J. Magn. Reson, Ser. A*, 2011, vol. 12, no. 2, pp. 75–105, [Online]. Available:

http://scion.duhs.duke.edu/vespa/http://www.swig.org.TheauthorsacknowledgeNIHfunding-1R01EB008387-01A1.

[115] H. Ratiney, M. Sdika, Y. Coenradie, S. Cavassila, D. van Ormondt, and D. Graveron-Demilly, "Time-domain semi-parametric estimation based on a metabolite basis set," *NMR Biomed.*, vol. 18, no. 1, pp. 1–13, 2005, doi: 10.1002/nbm.895.

[116] H. Barkhuijsen, R. de Beer, and D. van Ormondt, "Improved algorithm for noniterative time-domain model fitting to exponentially damped magnetic resonance signals," *J. Magn. Reson.*, vol. 73, no. 3, pp. 553–557, 1987, doi: 10.1016/0022-2364(87)90023-0.

[117] C. Ma, F. Lam, C. L. Johnson, and Z. P. Liang, "Removal of nuisance signals from limited and sparse 1H MRSI data using a union-of-subspaces model," *Magn. Reson. Med.*, vol. 75, no. 2, pp. 488–497, 2016, doi: 10.1002/mrm.25635.

[118] Y. Li, F. Lam, R. Guo, B. Clifford, X. Peng, and Z. Liang, "Removal of water sidebands from 1H-MRSI data acquired without water suppression," in *Proc. Intl. Soc. Magn. Reson. Med.*, 2018, p. 288.

[119] C. I. Haupt, N. Schuff, M. W. Weiner, and A. A. Maudsley, "Removal of lipid artifacts in 1H spectroscopic imaging by data extrapolation," *Magn. Reson. Med.*, vol. 35, no. 5, pp. 678–687, 1996, doi: 10.1002/mrm.1910350509.

[120] V. Kumar, U. Sharma, and N. R. Jagannathan, "In vivo magnetic resonance spectroscopy of cancer," *Biomed. Spectrosc. Imaging*, vol. 1, no. 1, pp. 89–100, 2012, doi: 10.3233/BSI-2012-0008.

[121] S. Trattnig *et al.*, "Key clinical benefits of neuroimaging at 7 T," *Neuroimage*, vol. 168, pp. 477–489, 2018, doi: 10.1016/j.neuroimage.2016.11.031.

[122] K. Herholz, "Brain Tumors: An Update on Clinical PET Research in Gliomas," *Seminars in Nuclear Medicine*, vol. 47, no. 1. pp. 5–17, 2017, doi: 10.1053/j.semnuclmed.2016.09.004.

[123] M. C. Preul *et al.*, "Accurate, noninvasive diagnosis of human brain tumors by using proton magnetic resonance spectroscopy," *Nat. Med.*, vol. 2, no. 3, pp. 323–325, 1996, doi: 10.1038/nm0396-323.

[124] A. Santos-Díaz and M. D. Noseworthy, "Phosphorus magnetic resonance spectroscopy and imaging (31P-MRS/MRSI) as a window to brain and muscle metabolism: A review of the methods," *Biomedical Signal Processing and Control*, vol. 60. 2020, doi: 10.1016/j.bspc.2020.101967.

[125] P. Bachert-Baumann, F. Ermark, H. -J Zabel, R. Sauter, W. Semmler, and W. J. Lorenz, "In vivo nuclear overhauser effect in 31P- {1H} double-resonance experiments in a 1.5-T whole-body MR system," *Magn. Reson. Med.*, vol. 15, no. 1, pp. 165–172, 1990, doi: 10.1002/mrm.1910150119.

[126] J. Ren, A. D. Sherry, and C. R. Malloy, "31P-MRS of healthy human brain: ATP synthesis, metabolite concentrations, pH, and T1 relaxation times," *NMR Biomed.*, vol. 28, no. 11, pp. 1455–1462, 2015, doi: 10.1002/nbm.3384.

[127] G. F. Mason *et al.*, "Evaluation of 31P metabolite differences in human cerebral gray and white matter," *Magn. Reson. Med.*, vol. 39, no. 3, pp. 346–353, 1998, doi: 10.1002/mrm.1910390303.

[128] X. H. Zhu, M. Lu, B. Y. Lee, K. Ugurbil, and W. Chen, "In vivo NAD assay reveals the

intracellular NAD contents and redox state in healthy human brain and their age dependences," *Proc. Natl. Acad. Sci. U. S. A.*, vol. 112, no. 9, 2015, doi: 10.1073/pnas.1417921112.

[129] V. S. Parekh and M. A. Jacobs, "Deep learning and radiomics in precision medicine," *Expert Review of Precision Medicine and Drug Development*, vol. 4, no. 2. pp. 59–72, 2019, doi: 10.1080/23808993.2019.1585805.

[130] X. Zhao and X. M. Zhao, "Deep learning of brain magnetic resonance images: A brief review," *Methods*, vol. 192. pp. 131–140, 2021, doi: 10.1016/j.ymeth.2020.09.007.

[131] J. Montalt-Tordera, V. Muthurangu, A. Hauptmann, and J. A. Steeden, "Machine learning in Magnetic Resonance Imaging: Image reconstruction," *Physica Medica*, vol. 83. pp. 79–87, 2021, doi: 10.1016/j.ejmp.2021.02.020.

[132] Z. Meng *et al.*, "Accelerating T2 mapping of the brain by integrating deep learning priors with low-rank and sparse modeling," *Magn. Reson. Med.*, vol. 85, no. 3, pp. 1455–1467, 2021, doi: 10.1002/mrm.28526.

[133] Y. Li *et al.*, "Machine Learning-Enabled High-Resolution Dynamic Deuterium MR Spectroscopic Imaging," *IEEE Trans. Med. Imaging*, vol. 40, no. 12, pp. 3879–3890, 2021, doi: 10.1109/TMI.2021.3101149.

[134] D. Ma *et al.*, "Magnetic resonance fingerprinting," *Nature*, vol. 495, no. 7440, pp. 187–192, 2013, doi: 10.1038/nature11971.

[135] A. G. Christodoulou *et al.*, "Magnetic resonance multitasking for motion-resolved quantitative cardiovascular imaging," *Nat. Biomed. Eng.*, vol. 2, no. 4, pp. 215–226, 2018, doi: 10.1038/s41551-018-0217-y.

[136] Y. Wang *et al.*, "STrategically Acquired Gradient Echo (STAGE) imaging, part II: Correcting for RF inhomogeneities in estimating T1 and proton density," *Magn. Reson. Imaging*, vol. 46, pp. 140–150, 2018, doi: 10.1016/j.mri.2017.10.006.

[137] F. Wang *et al.*, "Echo planar time-resolved imaging (EPTI)," *Magn. Reson. Med.*, vol. 81, no. 6, pp. 3599–3615, 2019, doi: 10.1002/mrm.27673.

[138] L. Tang *et al.*, "Accelerated J-resolved 1H-MRSI with limited and sparse sampling of (k,t1,t2-space," *Magn. Reson. Med.*, vol. 85, no. 1, pp. 30–41, 2021, doi: 10.1002/mrm.28413.